



Hochschule für Technik
und Wirtschaft Berlin

University of Applied Sciences

HZB BAIP
Beratung für BIPV

Thermographic Investigation of Photovoltaic Modules in a Building-Integrated Application

Masterthesis

in the course of studies of

Renewable Energies

Faculty 1

submitted by

Luca Marie Raschke

Date:

Berlin, 22nd September 2025

First Supervisor: Prof. Dr. Bert Stegemann

Second Supervisor: Dr. Björn Rau

Abstract

Maintenance and in this regard monitoring of PV modules is essential to enhance reliability, maintain efficiency and ensure long-term performance stability. Defects in PV modules cannot always be detected through system performance measurements alone, as detection sensitivity depends on string configuration and the interconnection of cells. To build on this gap, this case study investigates the application of infrared thermography (IRT) as a non-destructive and non-invasive tool for building-integrated photovoltaic (BIPV) systems. In this context specific attention was directed toward CIGS-based facade modules, which are integrated into a ventilated curtain wall system on the “Living Lab” of the Helmholtz-Zentrum Berlin (HZB). These modules were subjected to on-site performance monitoring and characterization as part of the study.

While IRT is well established in the maintenance of large rack-mounted photovoltaic (PV) plants, its use on building-integrated vertical installations introduces new challenges related to geometry, structural integration and environmental influences. Results reveal that structural elements such as metallic backrails dominate thermal patterns likely masking more subtle anomalies such as cell degradation or electrical faults. The study demonstrates how IRT can visualize ventilation behavior and thermal bridges offering insights on heat transfer phenomena neglected in many thermal models. Temperature differences exceeding 10 K within module regions of interest suggest possible performance loss due to cell mismatch. Measurements on damaged modules were conducted in a separate measurement setup to examine the viability of PV module damage detection through IR imaging.

While CIGS modules present low thermal contrast and require expert interpretation, damaged units can still be distinguished from intact modules – the distinctness depending on the measurement conditions. These measurements were combined with electroluminescence (EL) measurements and electrical characterization of a damaged CIGS module for a more detailed classification of thermographic images. The study concludes that IRT, when strategically implemented and complemented by diagnostic tools such as monitoring of electrical and environmental parameters, can significantly contribute to improve the maintenance quality of BIPV systems to ensure longevity and safety of the modules.

Table of Contents

Abstract	I
Table of Contents	II
Index of Figures	V
Index of Tables	IX
Nomenclature	X
1 Introduction.....	1
2 Infrared Thermal Imaging.....	3
2.1 Fundamentals of Thermography	3
2.2 Infrared Thermal Camera.....	4
2.3 Surface and Environmental Influences on Thermography	5
2.3.1 The Role of Emissivity in Thermography	5
2.3.2 The Role of Albedo in Thermography.....	6
2.3.3 Other External Influences on Thermography	6
2.4 Image Processing for Thermal Imaging.....	7
2.5 Infrared Thermography in Photovoltaic Systems	8
2.6 Difference between Indoor and Outdoor Thermography on PV	9
3 Building-Integrated Photovoltaic.....	11
3.1 Color of Building-Integrated Photovoltaic	11
3.2 Installation Typologies for BIPV	12
3.3 CIGS Solar Cell Technology	14
3.4 Electrical Parameters in Photovoltaics.....	14
3.5 Monitoring Technologies for Photovoltaic Systems.....	15
4 Temperature Dependence of PV Modules.....	17
4.1 Heat Sources of a PV Module.....	18
4.1.1 Heat Generation of a PV Module.....	18
4.1.2 Heat Dissipation of a PV Module	20
4.1.3 Resulting Energy Fluxes around a PV Module.....	22
4.2 Temperature Profile of a PV Module.....	23

4.3	Effects of Operating and Temperature on PV Performance	24
4.4	Thermal Cycling Impact on PV Module Degradation	25
5	Experimental Setup	26
5.1	The Building - Living Lab PVcomB	26
5.1.1	The Building Setup	26
5.1.2	Surrounding Grounds and Spatial Limitations	28
5.1.3	The Modules and the Mounting System	29
5.1.4	Obtaining Infrared Data on the PV Facade	31
5.2	HZB Outdoor Performance Laboratory	32
5.3	Measuring Tools	33
5.3.1	FLIR Camera and Software “FLIR ResearchIR Max”	33
5.3.2	Built-in Sensors of the PV Facade	34
5.3.3	Miscellaneous Measuring Tools	35
5.4	Flash Testing and Electroluminescence Measurements	35
6	Measurement Procedure.....	37
6.1	How to Interpret the Data	37
6.2	Absolute Temperatures	38
6.3	Image Processing after Measurements.....	39
6.4	Limitations during Measurements	40
6.5	Mitigation Strategies during Measurements	41
7	Results and Evaluation of Measurements (Analytics)	42
7.1	Interpretation of Data.....	42
7.1.1	IR Measurement at Modul Level	42
7.1.2	IR Measurement at System Level	44
7.1.3	IR Measurement at String Level	49
7.1.4	IR Measurement on Disconnected Strings.....	52
7.1.5	Integration of a Damaged Modules.....	54
7.1.6	Localized IR Anomalies across the Facade	63
7.2	The Significance of IR Measurement Results to BIPV Facades	66
7.2.1	On Module Level	66

7.2.2	On System level	67
7.3	Measurement Uncertainties Resulting from Measurements	68
7.3.1	Evaluation of Temperature Data at Pixel Scale	68
7.3.2	Camera	70
7.3.3	Reflection	70
7.3.4	Emissivity	72
7.3.5	Sensitivity of Sensors.....	72
8	Summary and Conclusion	73
9	Outlook	75
10	References	76
11	Academic Integrity Declaration	84
12	Appendix.....	85
A1	Additional Data	85
A2	Technical Data	87
	Acancis SKALA CIGS Modules	87
	IR Camera: FLIR A6700sc	87

Index of Figures

Figure 2-1: Intensity of blackbody radiation over the wavelength λ of the emitted radiation for multiple temperatures. [33]	4
Figure 2-2: Dependence of module emissivity on viewing angle. [37]	6
Figure 2-3: Manually defined temperature range [44]	7
Figure 2-4: IR images of module in defective condition a) indoor, and b) outdoor. [51]	10
Figure 3-1: Common support types for glazing elements. [53]	13
Figure 3-2: Construction of a CIGS solar cell on a microscopic scale [59].	14
Figure 3-3: a) Equivalent circuit model of a PV module with N_s cells connected in series and N_p parallel connected cells where I_{ph} is the photogenerated current, I_L is the light generated current, and V_L the voltage across the load [61], b) Influence of series and shunt resistance to an IV curve. [62]	15
Figure 4-1: Heat fluxes between the PV facade, bifacial (left) and monofacial (right) modules, and the outdoor environment. [72]	17
Figure 4-2: a) Simulated and Experimental EQE Spectra of a CIGS solar cell [77], b) Absorption coefficient of CIGS (for a bandgap of 1.2 eV). [78]	19
Figure 4-3: Energy flux from radiation and convection at the module front and rear sides for different wind speeds at 1,000 W/m ² , 45° module inclination and 25° C ambient temperature. [75]	22
Figure 4-4: Layer temperature in different module setups. [75]	24
Figure 5-1: HZB Living Lab in Adlershof, Berlin from the southwest corner of the building during morning hours.	26
Figure 5-2: String layout of south facade with modules with two temperature sensors on the back side marked yellow (one in the center and one on the edge), with one temperature sensor on the back side marked green (in the center), and the irradiance sensors marked with red circled numbers.	27
Figure 5-3: String layout of a) north and b) west facades with two temperature sensors on the back side marked yellow (one in the center and one on the edge), with one temperature sensor on the back side marked green (in the center), and the irradiance sensors marked with red circled numbers.	28
Figure 5-4: Surrounding grounds of the Living Lab and spatial restrictions when measuring the facade. [98]	29
Figure 5-5: Avancis SKALA Module in the shade blue 7003 from a) the front, b) the side, and c) the back view including part of the mounting system. [99]	30
Figure 5-6: Measurement setup for the south facade.	31
Figure 5-7: Measurement setup at the HZB outdoor performance laboratory measuring module 0069	32

Figure 5-8: FLIR 6700sc [101]	33
Figure 5-9: Software environment to evaluate IR measurement data.....	33
Figure 5-10: Irradiance sensor ML-02/ EKO-Instruments used on the Living Lab with dimensions. [102].....	34
Figure 5-11: Digital thermo-hygrometer 30.5048 from TFA-Dostmann.[103].....	35
Figure 5-12: Construction of the module in the dark room of the flasher at HTW Berlin before closing the curtains.	36
Figure 6-1: Relevance of the vertical orientation of most facade modules for IR measurement, b) facade modules with reflection of the horizon in comparison to a) 34° -angled modules with reflection of the (ideally cloudless) zenith, where the blue arrows represent the reflected ambient radiation and the red arrows represent the actual module radiation.	37
Figure 6-2: Thermocouple setup on the inactive area of the module.	39
Figure 7-1: IR picture of module P13 along the south facade while P13 is marked with a white dashed outline and the line scan analyzed in Figure 7-2 marked light blue.	42
Figure 7-2: Temperature course from top to bottom of module P13.....	43
Figure 7-3: Top view illustration of the measurement setup with the module being recorded by the IR camera positioned on the left side and marked red, a) being the setup as in Figure 7-5, and b) being the setup as in Figure 7-6.	44
Figure 7-4: Visualization of camera angle changing according to height of module position, δ represents the angle of the camera to the plane of the module, and the index i indicating the position of a module in a column.....	45
Figure 7-5: Temperature distribution of south-facing facade recorded from the front (90°) at ground level over the course of the day, visualized from hot (red) to cool (green) – the position of temperature sensors on the backside of each module marked by a thin box for one sensor in the middle and a thick double-lined box for one sensor in the middle and one on the edge of the module, the irradiance sensors are marked by red circled numbers.	46
Figure 7-6: Temperature distribution of south-facing facade over the course of the day, visualized from hot (red) to cool (green), recorded at a 45° -angle at ground level – the position of temperature sensors on the backside of each module marked by a thin box for one sensor in the middle and a thick double-lined box for one sensor in the middle and one on the edge of the module, the irradiance sensors are marked by red circled numbers.	47
Figure 7-7: Illustration of sun reflection on modules depending on time of day and camera orientation, a) reflection for recordings in Figure 7-5 at around noon with angle of incidence and angle of departure denoted as δ_s for a south positioned sun, b) reflection for recordings in Figure 7-6 in the afternoon with angle of incidence and angle of reflection denoted δ_{sw} for a southwest positioned sun.	48

Figure 7-8: Temperature difference (ΔT) of mean temperature measured by IR camera as in Figure 7-5 and measured by temperature sensor on module backsides of selected modules at the same time, a) with the sensor placed in the center of the module, and b) with the sensor placed at the edge of the module.....	49
Figure 7-9: Temperature development of strings equipped with temperature sensors with 0.5° C measuring accuracy from negative to positive pole a) for the north facade, b) for the west facade, and c) for the south facade.	51
Figure 7-10: IR recordings of open-circuit strings marked by grey dashed border, a) showing modules D2 to D8 from the right, b) showing modules D6 to D10 from the right, c) showing modules D10 to D13 from the left, and d) showing modules D1 to D7 from the front.....	53
Figure 7-11: Temperature effects of column D being in open-circuit, a) measurement of column C and D at an irradiance of about 460 W/m ² for the top half and 306 W/m ² for the bottom half of the modules, and b) measurement of column D and E at an irradiance of about 486 W/m ² for the top half and 324 W/m ² for the bottom half of the modules.	54
Figure 7-12: Image of a) a damaged module 0688, and b) an intact module 0069 in an indoor environment with incident irradiation coming from the right.	56
Figure 7-13: a) IR recording of module 0688 on 30.07.25 at 14:04, and b) IR recording of module 0069 on 30.07.25 at 13:50.....	56
Figure 7-14: a) EL recording of a functioning module but with damaged front glass (module 0688), b) EL recording of an intact module (module 0069).	56
Figure 7-15: a) IV curves of forward measuring method of module 0688 (damaged module) at varying irradiances, b) IV curves of forward measuring method of module 0069 (intact module) at varying irradiances.....	59
Figure 7-16: IV curves of both modules at irradiances of 1,000 W/m ² and 200 W/m ²	60
Figure 7-17: Development of fill factors across irradiance for module 0069 and module 0688..	61
Figure 7-18: Development of Voc across irradiance of module 0069 and module 0688.	61
Figure 7-19: North facade with hotspot in module B12 circled green, measured on 20.06.25 a) at 16:41 and b) 16:21.	63
Figure 7-20: West facade module C10 with hotspot on top right corner measured a) on 20.05.25 at 14:01, and b) on 02.06.25 at 12:27.	64
Figure 7-21: West facade crescent shaped cool area on module D1 measured on 20.06.25 a) at 15:50, and b) at 15:29.	64
Figure 7-22: South facade with a hot and cold spot pattern along modules A7, A8 and A9, a) on 20.05.25 at 13:30, and b) 20.06.25 at 14:02.	65
Figure 7-23: Temperature distribution across the radiometric thermal image of module P13 on the south facade on 01.07.25 at 13:30, a) pixels of the IR recording sorted by 0.5 K temperature ranges, b) box plot of the temperature distribution.	69
Figure 7-24: Effects of lens damage throughout the measurements recorded on different days circled green, a) on 20.05.25, and b) on 02.06.25.....	70

Figure 7-25: Power generated by the north facade on 09.08.25 – an exemplary sunny day. [124]	71
Figure 7-26: Bad positioning of the camera in reference to the sun's position causing reflection of the lens a) on the west facade during morning hours with AGC algorithm: PE on 02.06.25, b) on the north facade during early afternoon hours with AGC algorithm: APE on 20.06.25.	71
Figure 12-1: Temperature difference (ΔT) of mean temperature measured by IR camera, as in Figure 7-6, and measured by temperature sensor on module backsides of selected modules at the same time, a) with the sensor placed in the center of the module, and b) with the sensor placed at the edge of the module.....	85
Figure 12-2: Close-up of damaged front glass in module 0688.....	86
Figure 12-3: Entire IR recordings including temperature scale, a) IR recording of module 0688, b) mirrored IR recoding of module 0069	86
Figure 12-4: Module label stickers of the modules used on the HZB Living Lab facade, a) module type as for module 0069, and b) module type as for 0688.....	87

Index of Tables

Table 1: Installation categories for BIPV. [52], [53], [58]	12
Table 2: IR and EL imaging of a damaged module 0688 in comparison to an intact module 0069.	56
Table 3: Comparison of electrical performance data of measured modules 0069 and 0688 at 1,000 W/m ²	59
Table 4: R _s and R _{sh} values calculated from IV curve slopes.	62

Nomenclature

Abbreviation	Definition
AGC	a utomatic g ain
AZO	a luminum-doped z inc o xide
APE	a dvanced p lateau e qualization
BAIP	b uilding managers, a rchitects, i nvestors and urban developers, p lanners
BIPV	b uilding-integrated p hotovoltaic(s)
CIGS	c opper i ndium g allium s elenide
CdS	c admium s ulfide
CdTe	c admium t elluride
CO ₂	c arbon d ioxide
c-Si	c rystalline s ilicon
DDE	d igital d etail e nhancement
EQE	e xternal q uantum e fficiency
ESA	e lectrical s ignature a nalysis
EVA	e thylene-vinyl a cetate
HTW	Hochschule für Technik und Wirtschaft Berlin
IRT	i nfrared t hermography
IR	i nfrared
ISE	Fraunhofer I nstitute for S olar E nergy S ystems
IV	c urrent-voltage
EL	e lectroluminescence
FLIR	f orward l ooking i nfrared
ROI	r egion o f i nterest
HZB	H elmholtz- Z entrum B erlin für M aterialien und E nergie
IR	i nfrared
mc-Si	m ulticrystalline s ilicon
PE	p lateau e qualization
PVB	p olyvinyl b utyril
PVcomB	C ompetence C enter for P hotovoltaics B erlin
PVGL	p hotovoltaic g lass l aminate
sc-Si	monocrystalline silicon (s ingle- c rystal s ilicon)
TCO	t ransparent c onductive o xide
VCu	Copper vacancy
VSe	Selenium vacancy
VIS	v isual s pectrum
ZPV	Z entrum für P hotovoltaik und E rneuerbare E nergien (en: Photovoltaic Center)

Symbol	Unit	Definition
A	$[-]$	albedo
A_{PV}	$[m^2]$	area of the PV module
FF	$[-]$	fill factor
G_{bk}	$[W/m^2]$	solar irradiance incident on the back surface of bifacial modules
G_{fr}	$[W/m^2]$	solar irradiance incident on front surface
G_{POA}	$[W/m^2]$	solar irradiance in the plane of array
h_{force}	$[W/(m^2 \cdot K)]$	forced convection heat transfer coefficient
h_{free}	$[W/(m^2 \cdot K)]$	free convection heat transfer coefficient
I_{MPP}	$[A]$	current at maximum power point
I_{sc}	$[A]$	short circuit current
J_{sc}	$[mA/cm^2]$	short circuit current density
k	$[^{\circ}C \cdot m^2/W]$	Ross coefficient
l	$[m]$	thickness of material for conductive heat flow
P_{MPP}	$[W]$	maximum power
q_{pl}	$[W/m^2]$	heat flux on the building facade
P_{PV}	$[W]$	power output of a PV module
q_{bg}/q_{ted}	$[W/m^2]$	heat flux on the back glass or backsheets of a PV module
Q_{cond}	$[W]$	conductive heat flow
Q_{conv}	$[W]$	convective heat flow
q_{fg}	$[W/m^2]$	heat flux on the front glass of a PV module
Q_r	$[W]$	radiative heat flow
$Q_{solar,abs}$	$[W]$	solar irradiation heat flow absorbed by PV module front surface
R_s	$[\Omega]$	series resistance
R_{sh}	$[\Omega]$	shunt resistance
T	$[K, ^{\circ}C]$	temperature
T_{amb}	$[K, ^{\circ}C]$	ambient temperature
T_m	$[K, ^{\circ}C]$	module temperature
V_{oc}	$[V]$	open circuit voltage
V_{MPP}	$[V]$	voltage at maximum power point
v_w	$[m/s]$	wind speed
α_{abs}	$[mA/^{\circ}C]$	absolute temperature coefficient for a PV module's I_{sc}
β_{abs}	$[mV/^{\circ}C]$	absolute temperature coefficient for a PV module's V_{oc}
γ_{rel}	$[%/^{\circ}C]$	relative decrease in power output with temperature increase
$\delta_i, 1 \leq i \leq 14$	$[^{\circ}]$	IR camera viewing angle between ground and facade plane
ε	$[-]$	emissivity
κ	$[W/(m \cdot K)]$	thermal conductivity
λ	$[\mu m, nm]$	wavelength
σ	$[W/(m^2 K^4)]$	Stefan-Boltzmann constant $\sigma = (5,67 \times 10^{-8} W/(m^2 K^4))$
Φ	$[K/W]$	thermal resistance of emitter

1 Introduction

The required decarbonization of the energy sector is no longer under discussion. Global CO₂ emissions from the energy sector reached an all-time high of 37.8 billion tons in 2024, even though the growth in emissions slowed down compared to previous years. However, a rapid and uncomplicated introduction of subaerial energy technologies could avoid up to 2.6 billion tons of CO₂ emissions every year. [1]

Decarbonizing the energy system is a major driver of land use competition on regional, national and global scales [2]. The German government has set climate targets aiming to achieve climate neutrality by 2045 by increasing the share of renewable energies from 54.4% to at least 80% by 2030 [3], [4]. Solar energy is expected to play a central role in reaching this goal [5]. Current expansion scenarios for solar energy focus primarily on two technologies: rooftop photovoltaics and ground-mounted photovoltaics (PV) on fields. Consequently, their exponentially growing presence is generating a diverse array of new and challenging land use conflicts [6], [7]. Innovative solutions have been found already, such as agrivoltaics (a combined use of land for agriculture and photovoltaics), which unite the agriculture and the energy sector [8], [9]. Therefore, particularly in urban areas, the implementation of building-integrated photovoltaics (BIPV) – embedding solar modules directly into the architecture of buildings – has yet to be widely implemented, despite offering considerable opportunities for energy generation and sustainable design. If fully utilized, from an area potential perspective BIPV alone could provide more energy than required for a 100% share of renewable electricity in Germany [10], [11], [12].

Several countries have already introduced regulations that promote or mandate the integration of solar technologies in new construction and renovation projects. These directives are most commonly applied in urban zones and can be found across Europe in countries such as Germany [13], France [14], [15], Austria [16] and Switzerland [17], [18] as well as globally in regions like California (USA) [19] or Tokyo (Japan) [20]. Thus, considering the capabilities and dynamics of the construction sector, the economically viable share of electricity generation through BIPV in Germany is estimated to reach up to 26%. Depending on the scenario, BIPV capacity could range from 80 GWp in conservative projections to 160 GWp under more optimistic assumptions [11].

BIPV extends beyond electrical performance and sustainability, embracing significant opportunities to the design and architectural level. The modules offer increasing flexibility and autonomy, whether they are explicitly showcased as design elements or subtly integrated into the building envelope to remain hidden and only discernable at second glance.

Stable electricity generation is in the best interest of all PV system operators. It is therefore essential to identify whether the system or individual modules are operating at limited capacity or may even be damaged. However, damage is not always visible at first glance – particularly for large scale systems. Especially for copper indium gallium selenide (CIGS)-modules a cracked

front glass is often only visible from close proximity. Regular monitoring and inspection are advised to ensure the optimal performance and productivity of PV systems [21], [22].

Infrared thermography (IRT) has been implemented lately as one of the most advanced techniques for inspecting and maintaining solar PV systems, owing to its non-destructive and non-contact characteristics. This allows for inspecting large-scale solar PV systems without interrupting their operation [23], [24]. This is particularly convenient for BIPV, where inspection possibilities are often limited, for example by a facade structure on the back side. However, as BIPV itself is still a relatively unconventional concept, most efforts of thermal modelling and infrared imaging focus on PV plants and not PV in buildings [25], [26], [27], [28]. Thermography is increasingly being used as a method for detecting PV defects in photovoltaic power plants and often carried out using drones equipped with thermal cameras [24], [27], [29], [30].

The objective of this research is to determine the feasibility and limitations of IR thermography as a diagnostic tool for facade-integrated CIGS PV modules. In this context, it is assessed whether IRT can meaningfully contribute to the maintenance of PV systems in building-integrated applications. This case study is based on a detailed analysis of a monitored building – the “Living Lab” at the Helmholtz-Zentrum Berlin (HZB) – equipped with facade-integrated BIPV, where IR imaging was conducted under varying environmental conditions. As the building’s facade is covered with CIGS modules, this work focuses on the application of outdoor infrared thermography (IRT) for fault detection on CIGS technology under real-world operating conditions. These measurements are complemented by obtaining electrical parameters such as electroluminescence (EL) and current-voltage (IV) curves. The goal is to determine to which extent IR thermography can reliably detect performance relevant anomalies in BIPV systems and to identify the factors that influence its diagnostic value.

The structure of the thesis is as follows: Firstly, Chapter 2 introduces the principles of IRT and its conventional applications in PV diagnostics. Chapter 3 provides an overview of BIPV technologies and the specific characteristics of CIGS modules. To sum up the theoretical outline of the work Chapter 4 elaborates on the relevance of temperature in module operation. Chapter 5 outlines the experimental setup, including the reference building in the center of this work’s discussion, while chapter 6 follows up on the acquisition methods. Chapter 7 presents the core results of IR imaging and complimentary measurements and later discusses the relevance of these results to PV system operation. The chapter further lists a range of sources for error in PV thermography visible throughout the measurements conducted in this work. Finally, Chapter 8 and 9 offer a conclusion and an outlook on possible future research directions.

This thesis addresses the gap in the implementation of infrared thermography for fault detection in facade-integrated PV systems. By combining real-world measurements with electrical characterization, this work improves the understanding of how thermal imaging performs in complex building environments and how it can contribute to improved design, maintenance, and performance of BIPV systems.

2 Infrared Thermal Imaging

Thermography, the short term for Infrared (IR) thermal imaging is a rapidly evolving field in science as well as the industry [26], [31]. To understand how thermal imaging can be applied to photovoltaic diagnostics, it is essential to first explore the physical principles that regulate thermography.

2.1 Fundamentals of Thermography

Infrared radiation is constantly present in our environment, though it remains invisible to the human eye. Any object with a temperature above absolute zero emits infrared radiation as part of its thermal energy. The primary distinction between infrared radiation and visible light lies in their respective wavelength: visible light spans the range of approx. 380 – 750 nm and carries higher energy, whereas infrared radiation occupies longer wavelengths and therefore lower energy levels. Figure 2-1 illustrates the distribution of various electromagnetic wavelength ranges.

IR radiation belongs to the electromagnetic spectrum with a wavelength range between 780 nm and 1 mm. It is commonly divided into three subcategories: IR-A (780 nm – 1,400 nm), which borders the visible spectrum, IR-B (1,400 nm – 3,000 nm), and IR-C (3,000 nm – 1 mm). The most significant natural source of infrared radiation is sunlight with over half of its total energy output falling within the infrared range. [32]

When electromagnetic radiation strikes the surface of an object it is partially absorbed and partially reflected. At thermal equilibrium, the rate of absorption equals the rate of emission, where a good absorber of radiation is also a good emitter. An idealized object that absorbs all incident electromagnetic radiation – without reflecting or transmitting any – is referred to as a blackbody. While no real material absorbs 100% of incident radiation, the blackbody serves as a theoretical model in thermodynamics. At given temperature T , a body in thermodynamic equilibrium emits radiation at the same time it absorbs it. The emission spectrum of a blackbody is visualized in the following illustration. Electromagnetic waves emitted by a blackbody are called blackbody radiation. [33]

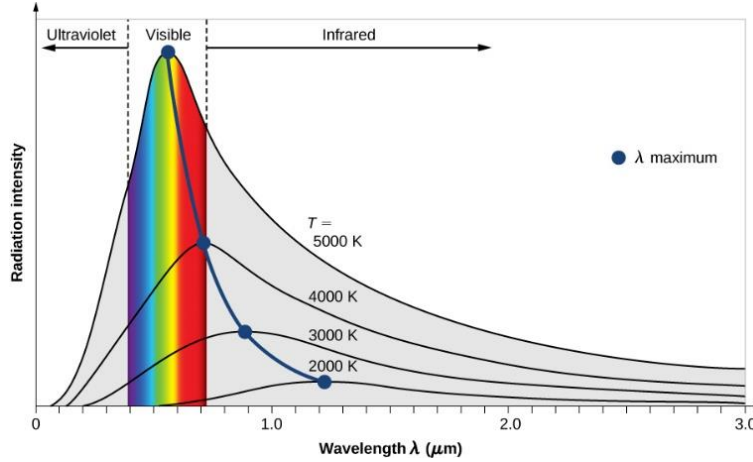


Figure 2-1: Intensity of blackbody radiation over the wavelength λ of the emitted radiation for multiple temperatures. [33]

The intensity $I(\lambda, T)$ of blackbody radiation depends on the wavelength λ of the emitted radiation and on the temperature T of the blackbody (see Figure 2-1). The function $I(\lambda, T)$ is the power intensity that is radiated per unit wavelength. Most real-world materials emit thermal radiation that only approximately follows the idealized blackbody radiation curve. The spectral density of electromagnetic radiation emitted by a blackbody in thermal equilibrium at a given temperature is described by Planck's law or Planck's blackbody radiation law. [33], [34], [35]

Planck's law leads to two important derived laws. One of them being Wien's displacement law which is visualized in Figure 2-1 as a dark blue curve connecting each temperatures' wavelength maxima, illustrating the peak wavelength of blackbody radiation shifts toward longer wavelengths as the temperature decreases. Wien's displacement law allows to estimate the temperatures of distant surfaces by measuring the wavelength of radiation they emit and reads [33]:

$$\lambda_{max} T = 2.898 \cdot 10^{-3} m \cdot K \quad (2-1)$$

Secondly, Stefan-Boltzmann's law (see Chapter 4.1.2.2) describes the total power of a blackbody radiation emitted across the entire spectrum of wavelengths at a given temperature and is represented by the area under the blackbody radiation curve for a given temperature. Real bodies emit less radiation than blackbodies defined by their emissivity. [33], [35]

2.2 Infrared Thermal Camera

Building on the theoretical framework, this section introduces the infrared thermal camera as a central instrument for capturing temperature distributions. Thermal imaging provides a noninvasive and sophisticated method for visualizing heat emissions from various objects, transforming invisible infrared into a visible display. Infrared cameras detect radiation and present imagery in the visible spectrum that allows observers to "see the heat". Depending on their design, they can either produce qualitative images or deliver quantitative temperature measurements. As

such, infrared thermography enables the assessment of the thermal condition or operational state of a target or process. [31]

Infrared thermal imaging refers to the technique of generating radiometric digital images within the thermal infrared wavelength range, typically between 0.8 - 25 μm . In addition to visualizing heat patterns, this method allows for accurate surface temperature measurement, making it a valuable tool in diagnostics and monitoring. [35] [36]

To convert infrared radiation into meaningful temperature data, IR cameras apply physical models such as Planck's radiation law and the Stefan-Boltzmann law, incorporating emissivity correction and sensor calibration. This enables the transformation of detected radiation intensity across a range of wavelengths into electrical signals, which are subsequently processed to yield quantified temperature values.

To effectively capture infrared radiation – primarily thermal emissions – the optical components of IR cameras, such as lenses and filters, must be transparent to infrared wavelengths. Unlike visible-light cameras, which use glass optics, IR cameras use semiconductors. The detectors used are not silicon-based as in visual spectrum (VIS) cameras; instead, depending on their sensitivity and the target wavelength region, they are manufactured using a wide range of materials, including cooled photoelectron detectors and uncooled thermal sensors. Since pixel signals in thermal imaging are typically not spectrally filtered, the raw output resembles monochrome imagery, which is then processed into grayscales or false-color images to enhance interpretability. [35]

2.3 Surface and Environmental Influences on Thermography

To ensure reliable reproducible thermographic measurements, several key parameters must be considered for a correct calibration of the measurement setup. Surface properties and surrounding environmental conditions are among the most critical factors influencing the accuracy of thermographic measurements.

2.3.1 The Role of Emissivity in Thermography

Real objects emit less radiation than ideal blackbodies, defined by their emissivity. Any quantitative analysis requires knowledge of the correct emissivity of the objects, which is the most important parameter affecting temperature measurement accuracy. Emissivity describes how efficiently a surface emits infrared radiation compared to a perfect blackbody. For PV glass and encapsulants, typical values range between 0.85 and 0.95. According to DIN IEC/TS 62446-3 a value between 0.85 and 0.9 is a representable value for measurement perpendicular to the module plane as seen in Figure 2-2.

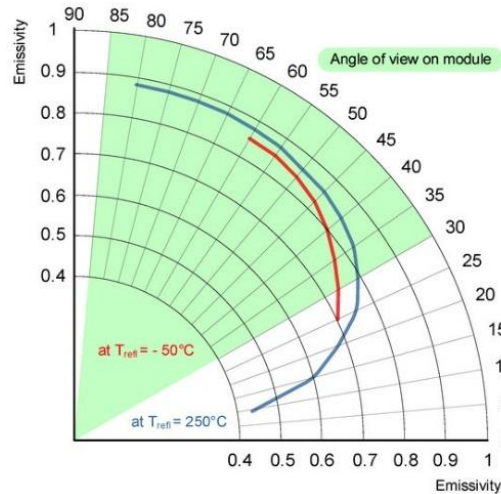


Figure 2-2: Dependence of module emissivity on viewing angle. [37]

Figure 2-2 illustrates the exponential decline in surface emissivity as the angle of view decreases, alongside its dependence on the reflected temperature. The optimal viewing angle range is highlighted in green, though it narrows as the demand for accuracy rises with the angle approaching close to 90°. Outdoor analysis is often further complicated by the fact that each image represents a combination of temperature variations and emissivity contrasts. As a result, minor deviations in emissivity within the highlighted range are considered acceptable for outdoor measurements. [35], [36], [38]

2.3.2 The Role of Albedo in Thermography

Albedo (A) describes how much solar radiation is reflected by surrounding surfaces such as rooftops or facades, which can influence both module heating and IR measurements. The albedo value is a dimensionless value between 0 and 1. While an ice surface or a snowy surface have high albedo values between 0.8 and 0.9, green areas like forests possess albedo values of about 0.2, and aquatic bodies reach albedo values below 0.1 [39]. While reflectance only describes the fraction of incident irradiation reflected at a specific angle and wavelength, albedo describes the integrated reflectance over all angles and wavelengths of incoming solar radiation. The albedo effect in PV systems can be engineered to reflect non-usable wavelengths, while also allowing usable wavelengths to be absorbed by the cells [40].

2.3.3 Other External Influences on Thermography

In addition to surface characteristics, several environmental parameters affect the accuracy and interpretability of IR measurements. Ambient temperature and humidity influence radiative exchange and sensor calibration, particularly in outdoor settings where fluctuations are common. High humidity can attenuate IR radiation, particularly in the mid- and long-wave IR region, leading to underestimation of surface temperatures and reducing image contrast, which can compromise the accuracy of thermographic diagnostics. [41], [42]

Extraneous IR signals from reflective surroundings can interfere with precise thermal imaging. The viewing angle and distance further affect measurement reliability. Oblique angles can reduce apparent emissivity and increase reflectivity, while excessive distance may degrade spatial resolution and introduce atmospheric interference. [26], [43]

To mitigate these effects, it is recommended to maintain a close to perpendicular viewing angle marked green in Figure 2-2 as well as a consistent measuring distance.

Together these factors underscore the importance of a controlled and well documented measurement setup, especially in outdoor PV applications where environmental variability is high.

2.4 Image Processing for Thermal Imaging

Once the thermal data is captured, it must be processed to exact meaningful insights. The following chapter describes the methods used to convert raw infrared signals into interpretable images.

Thermal imaging is distinguished between radiometric and non-radiometric images. Radiometric thermal images preserve pixel level temperature data, enabling post capture analysis and calibration adjustments. Non-radiometric images by contrast are limited to qualitative visualization and cannot be used for quantitative evaluation, which is essential for photovoltaic diagnostic to define regions of interest (ROI), apply different color pallets, and even export temperature profiles after the image was captured [44], [45]. ROIs isolate specific areas, such as individual modules, to perform targeted evaluations and reduce the influence of background noise. Manually applying individual temperature ranges, such as shown in Figure 2-3, allows specific temperature intervals to be highlighted, making them stand out visually. Temperatures outside the defined range are typically displayed in a uniform monotone, enhancing contrast and interpretability. [44]

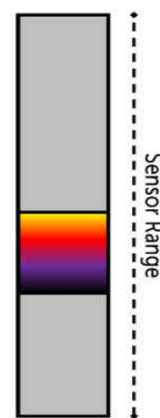


Figure 2-3: Manually defined temperature range [44].

The software used includes several image enhancement algorithms that optimize thermogram contrast and clarity without affecting the temperature accuracy. Through its Automatic Gain Control (AGC) settings, users can adjust how color is mapped to thermal data. The software offers three AGC algorithms – Plateau Equalization (PE), Digital Detail Enhancement (DDE), and Advanced Plateau Equalization (APE), which are each designed to improve image detail and highlight temperature variations more effectively [46]. Further enhancement can be achieved by applying thermal color palettes, which improve the effectiveness of temperature measurement by helping to identify subtle differences within a defined temperature range. The choice of palette can influence the visibility of subtle temperature gradients and should be selected based on the diagnostic objective.

2.5 Infrared Thermography in Photovoltaic Systems

IR Thermography has become an indispensable tool for the monitoring and maintenance of solar PV systems. It is particularly effective in identifying module defects that appear as thermal anomalies, such as hotspots caused by cell cracks, shunting, or interconnection faults. By visualizing temperature differentials across the module surface, IR thermography enables early detection of performance issues. Its integration into routine maintenance practices has significantly enhanced the system reliability, efficiency and operational lifespan. [28]

Depending on the PV technology analyses, IR thermography might behave differently in terms of thermal response, defect visibility and optical absorption. CIGS modules tend to show more diffuse thermal patterns due to their thin film architecture [47]. c-Si modules on the other hand often exhibit localized hotspots that are easier to detect with IR thermography, especially critical when faults such as cell cracks or interconnect failures are present. In addition, CIGS cells have a lower temperature coefficient, which means they heat up less under the same irradiance and thermal anomalies are subtler and harder to detect. Typical thermal signatures of PV-defects like cell mismatch bypass diode failure or module glass breakage can be read up on in multiple studies [27], [28], [29], [47].

As part of this work, an attempt was made to adhere to the relevant standard protocols for the thermography procedure. The main focus here was on DIN IEC/TS 62446-3:2018-04 [38], which is the German version of the IEC/TS 62446-3:2017 standard for reasons of availability. Full Name of the Standard is *Photovoltaic (PV) systems - Requirements for testing, documentation and maintenance - Part 3: Photovoltaic modules and plants - Outdoor infrared thermography* and “defines outdoor thermographic (infrared) inspection of PV modules and plants in operation. This inspection supports the preventive maintenance for fire protection, the availability of the system for power production, and the inspection of the quality of the PV modules. This document lays down requirements for the measurement equipment, ambient conditions, inspection procedure, inspection report, personnel qualification and a matrix for thermal abnormalities as a guideline for the inspection.” [48]

To ensure valid measurement results the following conditions must be taken into account during thermographic assessments:

- Irradiance in the plane of the module should be at least 600 W/m^2 .
- Windspeed should not exceed 4 Bft or 28 km/h.
- The coverage degree of a sky with cumulus clouds should not surpass 2 Okta.
- After a change in operating conditions, e.g. load or irradiance (e.g. due to cirrus clouds) of $>10\%$ per minute, a waiting period of 15 minutes is recommended to regain stable measurement conditions.
- The IR data should be captured as perpendicular to the surface of the PV module as possible. If a perpendicular angle cannot be achieved, the viewing angle should at least be greater than 30° to maintain measurement accuracy.

The Ross coefficient k is a parameter used in steady state PV temperature models to describe the linear relationship between solar irradiance in the plane of array (or module) G_{POA} and module temperature T_m :

$$T_m = T_{amb} + k \cdot G_{POA} \quad (2-2)$$

In the context of thermography for PV systems – particularly BIPV – it helps estimate surface temperatures by correlating thermal imaging data with irradiance levels under varying environmental and mounting conditions. [25], [49]

2.6 Difference between Indoor and Outdoor Thermography on PV

The IEC/TS 62446-3:2017 standard focuses specifically on outdoor thermographic measurements. However, CIGS modules are often analyzed in indoor settings, as controlled conditions can enhance the visibility and reliability of thermal anomalies. That said, it is important to address the distinctions between indoor and outdoor thermography, particularly since indoor measurements are simply not always feasible in certain applications. Thermal imaging conditions vary significantly between controlled indoor environments and dynamic outdoor settings. The following section highlights how outdoor parameters influence measurement accuracy and interpretation. A study conducted on c-Si PV modules after 20 years of operation found that outdoor IR measurements (illuminated) do not correlate with corresponding indoor IR measurements under dark thermography conditions, indicating significant environmental and operational influences on thermal imaging results [50].

In indoor thermography, current is supplied to the PV module in a dark environment. Degraded cells or regions appear cooler in the IR image as current does not flow through them, resulting in less heat generation. In outdoor thermography, no external current is supplied. Instead, incoming solar radiation generates current within the cells. Degraded cells or regions show up as hotspots, since they fail to convert solar energy into electricity efficiently and instead dissipate it as heat [51]. High quality images are best taken in a darkened environment for a better signal to noise ratio [26].

The following images compare the infrared thermography of the same module under indoor conditions (left) and outdoor conditions (right). The results show significant visual differences, which can quickly lead to misinterpretations, if environmental influences are not properly taken into consideration.

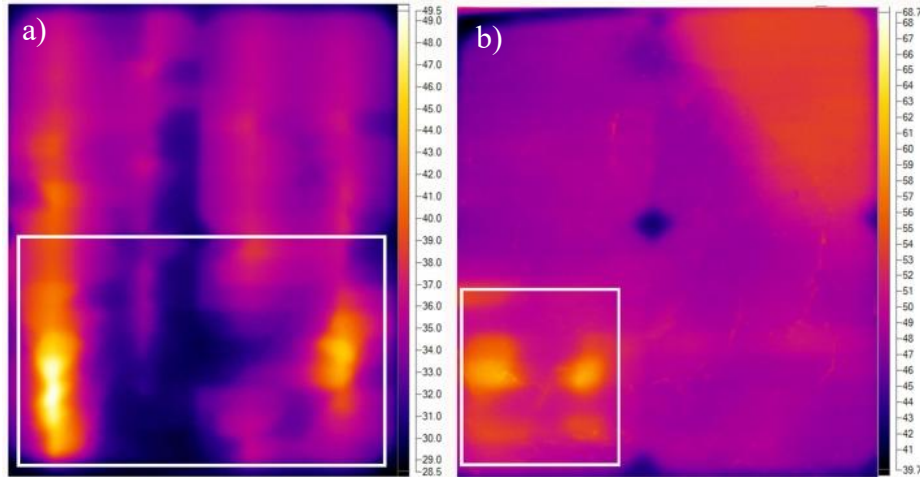


Figure 2-4: IR images of module in defective condition a) indoor, and b) outdoor. [51]

As shown above, even with the use of a professional-class camera in accordance with [26], some defects are not detectable under outdoor conditions. The IR image in Figure 2-4 b) reveals several hotspots near the bottom left corner, but these do not sufficiently correspond with the indoor IR image. In addition, a warm zone appears near the top-right area in the outdoor image, which is not present in the indoor image. The identified defect regions are marked in the figure above [51]. The regions appearing as hotspots in b) may not actually exhibit elevated temperatures, but could instead be the result of unaccounted for reflections from the surrounding measurement environment.

3 Building-Integrated Photovoltaic

Building-Integrated Photovoltaics (BIPV) present an efficient approach of generating renewable energy on-site, while simultaneously satisfying architectural design criteria and serving one or multiple functions in the building envelope. BIPV refers to photovoltaic modules/ systems that are added seamlessly into the building envelope and replace conventional building components. As such, they are required to meet both electrical and building requirements to ensure safety and reliable performance. [52]

To fulfill these architectural and constructional requirements BIPV modules have special features compared to standard PV modules – the simplest BIPV structure consists of a PV laminate formed by bonding the following layers: front cover (*front sheet*)/ encapsulant/ PV cells/ back cover (*back sheet*). If both the front and the back covers are out of glass, the structure becomes a PV glass laminate (PVGL). The mechanical properties of the laminate are determined by the characteristics of the glass panes in combination with the encapsulant. Commonly used encapsulant materials are ethylene-vinyl acetate (EVA) or polyvinyl butyral (PVB). [52]

3.1 Color of Building-Integrated Photovoltaic

As mentioned, BIPV is characterized by the fulfillment of the high architectural requirements and therefore using color to conceal the PV cells. The realization of invisible PV technology can be achieved either by monochromatic dark modules in cell color (e.g. black or blue) or by colored layers, behind which the dark cell layer cannot be seen. For the former, the dark cell color is used and all the other surfaces such as busbars or the back sheet of conventional modules are masked by darkening them the same color [53]. To widen the color selection, another technical option is to place semi-transparent, colored layers in front of the PV cell layer. A high transmittance of the colored layers is necessary to reduce impact on the efficiency and thus the energy yield of the BIPV modules.

For the following work, the focus will be on the option featuring a colored coating on the inner surface of the front glass. These colors can be achieved by using ceramic pigments, spectrally selective interference coatings, or other photonic structures. The use of organic materials is crucial to ensure long service life. This approach limits relative efficiency losses compared to a black module to less than 15%, and in some cases, even below 7%. [53]

The perceived color of an opaque object under sunlight depends on the spectrum of the reflected light directed by the human eye. Highly efficient PV modules appear dark or black due to their low reflectivity and high absorption. To make such modules appear white, their reflectance across the visible spectrum must increase, which in turn reduces the amount of solar energy available for conversion [54]. As IR cameras detect surface emitted radiation, the surface layer in contact with the environment dominates the thermal signature. Consequently, the visible color of a module is not directly recorded by an IR camera. Instead, the accuracy of thermography depends primarily

on the emissivity of the outermost surface. Dark, high emissive surfaces provide more reliable thermal data, whereas reflective or light-colored materials may distort measurements due to ambient IR reflections.

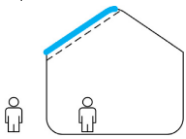
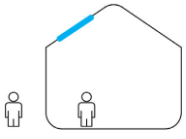
In glass-glass BIPV CIGS modules, the color giving coating beneath the front glass has minimal influence on thermal emission captured by IR imaging, as the emission is almost entirely governed by the glass surface itself. Standard PV glass has a high emissivity (see Figure 2-2), so the subsurface color layer is not directly visible in the camera. However, the color coating still affects the module's thermal behavior indirectly, as different colors absorb and reflect visible sunlight differently. Darker coatings increase absorption and thus local heating, while lighter coatings reflect more light and run cooler. These differences in absorption alter the internal heat distribution, which can become apparent in IR thermography as temperature variations. Yet these variations are the result of optical absorption differences and not changes in emissivity. [55], [56]

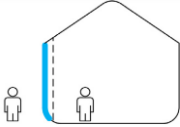
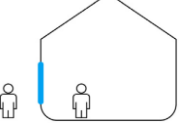
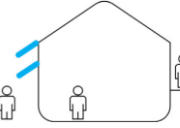
3.2 Installation Typologies for BIPV

The integration of modules often requires project specific customized BIPV modules in shape and size, or as discussed above the color. When approaching the planning and design of BIPV systems, it is helpful to distinguish between different types of installations, as each type imposes fundamentally different requirements on the PV module [57].

According to EN 50583-1, BIPV application typologies are divided into categories A-E. In summary, categories A and B include various roof integrations, categories C and D highlight facade integrations, whereas category E refers to integrations that include an additional functional layer, such as shading elements or balustrades [58]. Table 1 offers a more thorough overview of the different categories and their requirements.

Table 1: Installation categories for BIPV. [52], [53], [58]

BIPV system group	BIPV system	BIPV application category	BIPV performance requirements
BIPV roof systems	Continuous roofing Discontinuous roofing	A) 	<ul style="list-style-type: none"> - Fire safety - Mechanical resistance and durability - Electrotechnical - Hygro-thermal performance
	Atriums and Skylights	B) 	<ul style="list-style-type: none"> - Fire safety - Safety and accessibility in use - Mechanical resistance and durability - Electrotechnical - Daylight and solar gains - Protection against noise (if applicable)

BIPV facade systems	Rainscreen or ventilated facade	C)		<ul style="list-style-type: none"> - Fire safety - Mechanical resistance and durability - Electromechanical - Hygro-thermal performance
	Double skin facade Masonry wall			
	Window Curtain wall	D)		<ul style="list-style-type: none"> - Fire safety - Safety and accessibility in use - Mechanical resistance and durability - Electrotechnical - Hygro-thermal performance - Protection against noise (if applicable)
BIPV external elements	Parapet Balustrade Canopy Solar Shading Device	E)		<ul style="list-style-type: none"> - Fire safety - Safety and accessibility in use - Mechanical resistance and durability - Electrotechnical - Daylight and solar gains (if applicable)

The dashed line symbolizes blocked accessibility from inside the building. EN 50583-1 also describes further requirements for each category that will not be discussed in this context.

Well-known support systems for glass elements can be applied to mount BIPV modules. Figure 3-1 provides an overview of common support types for glazing elements that can be used to install BIPV. However, national and local regulations for use, design and construction apply.

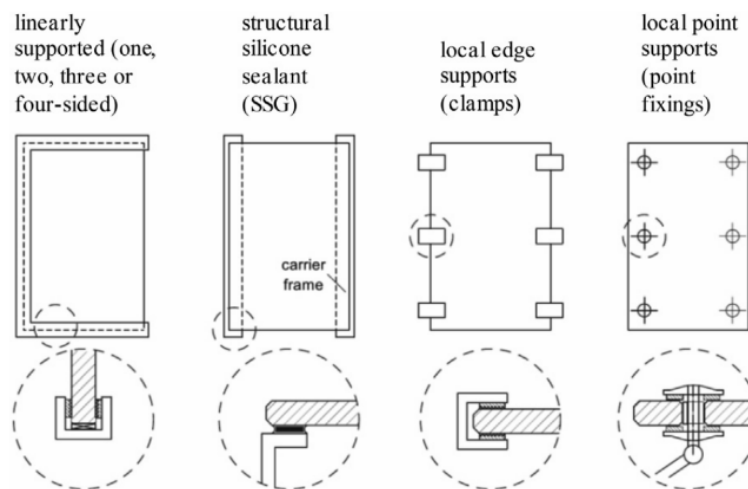


Figure 3-1: Common support types for glazing elements. [53]

When analyzing IR data from a BIPV facade, it is crucial to account for mounting-related influences to avoid misinterpreting thermal anomalies. Direct contact points can act as thermal bridges altering local temperatures. These areas may appear cooler in IR images due to enhanced heat dissipation potentially masking nearby hotspots or defects. Ventilated facades specifically

allow air circulation behind the PV modules, which helps regulate their temperature. As a result, IR images typically show lower and more uniform surface temperatures.

3.3 CIGS Solar Cell Technology

For the different integration forms for BIPV as described above, different module technologies are eligible. Following crystalline silicon (c-Si) technology – both multicrystalline (mc-Si) and monocrystalline (sc-Si), which are known for their high efficiency and reliable performance across various conditions – thin-film photovoltaics represent the second most commonly used PV technology for BIPV applications, although they are not as widely adopted. This category includes variants such as amorphous silicon (a-Si), CIGS (copper indium gallium selenide), and CdTe (cadmium telluride), and is characterized by its aesthetic versatility [52]. For the following work, the CIGS technology will primarily be elaborated on more thoroughly.

CIGS stands for its components copper (C), indium (I), gallium (G) and selenium (Se). One of the main characteristics of CIGS technology is the defining feature of the relatively thin semiconductor layer of approx. 2 μm , which is why CIGS belong to the group of thin film technologies. Figure 3-2 shows the cross-section of the layer structure from back to front in CIGS technology, used in the modules examined in this thesis. In this configuration, sulfur (S) is added to the four base elements, modifying the absorber layer composition. The bottom – orange – layer is the molybdenum (Mo) back contact layer deposited on the

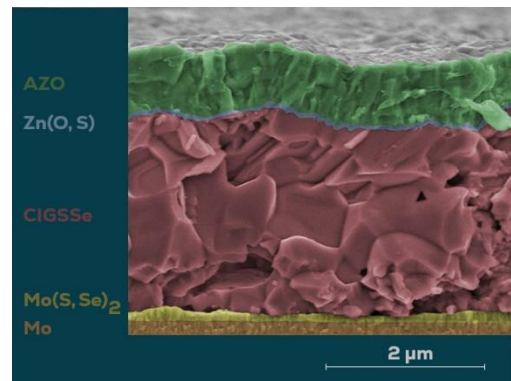


Figure 3-2: Construction of a CIGS solar cell on a microscopic scale [59].

substrate glass. It is followed by a molybdenum sulfoselenide ($\text{Mo}(\text{S},\text{Se})_2$) layer – yellow in the figure above – formed by the reaction of sulfur and selenium with the Mo back contact. [59] The red colored positively conducting CIGS Se layer is the absorber layer. In this case, a thin buffer layer consisting of zinc oxide sulfide ($\text{Zn}(\text{O},\text{S})$) is deposited on the CIGS absorber layer – colored blue. The layer stack is completed by a transparent conductive oxide (TCO), in this case a negatively conductive aluminum-doped zinc oxide (AZO) layer – colored green – which provides good surface passivation, thereby reducing surface recombination. It also offers high optical transparency in the visible and near-infrared wavelength regions. [59], [60]

3.4 Electrical Parameters in Photovoltaics

While IR imaging effectively reveals surface temperature anomalies such as hotspots, analyzing the IV curve provides deeper insight into the internal condition of a PV module. Electrical parameters such as short-circuit current (I_{sc}), open-circuit voltage (V_{oc}), current at maximum power

point (I_{MPP}), voltage at maximum power point (V_{MPP}), maximum power (P_{MPP}), fill factor (FF) and resistive effects can indicate underlying issues such as cell degradation, shunting, or interconnective failures that may not be visible through thermal imaging alone. Together they offer a more complete diagnostic picture of both thermal and electrical performance. Figure 3-3 a) illustrates the equivalent circuit module of a photovoltaic module, highlighting the key resistive components that influence its electrical performance. The series resistance R_s , shown in line with the current path, represents internal losses due to contacts and interconnections. In contrast, the shunt resistance R_{sh} , positioned parallel to the diode, models leakage currents that bypass the p-n junction. Together these resistances shape the IV curve seen in Figure 3-3 b) and serve as indicators of the cell condition. [49], [50]

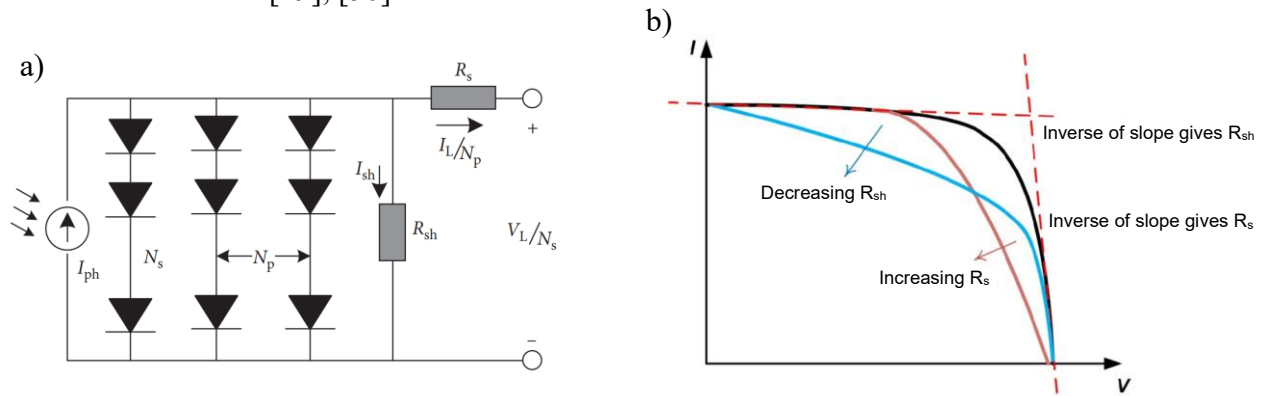


Figure 3-3: a) Equivalent circuit model of a PV module with N_s cells connected in series and N_p parallel connected cells where I_{ph} is the photogenerated current, I_L is the light generated current, and V_L the voltage across the load [61], b) Influence of series and shunt resistance to an IV curve. [62]

As Figure 3-3 b) shows, the IV curve is shaped by both R_s and R_{sh} . Efficient cells have a low R_s and a high R_{sh} , resulting in a steep, square shaped IV curve. Deviations such as a high R_s suggest poor conductivity or aging while a low R_{sh} may signal defects such as cracks or contamination. [49], [50]

3.5 Monitoring Technologies for Photovoltaic Systems

To collect meaningful data and interpret the introduced parameters accurately, selecting the appropriate monitoring technology is the essential first step. Monitoring technologies are essential to ensure PV systems operate efficiently and reliably long-term. PV systems experience different unexpected faults do to human errors, temperature, humidity, mechanical load, shading, equipment damage and degradation [63], [64], [65].

The most common monitoring method is electrical signature analysis (ESA), which involves measuring current-voltage curves (IV curves), power output or string level performance. Tools like IV curve tracers and electroluminescence (EL) imaging help detect microcracks, shunted cells, or mismatched modules. They are frequently used during commissioning or troubleshooting and increasingly integrated into automated monitoring systems, due to the low economic investment

required to implement this approach into the diagnostic task [66]. Beyond classical electrical performance monitoring and environmental and thermal analysis, building energy management systems integrate BIPV data into overall building operations, enabling more comprehensive and intelligent energy control.

The building envelope integration itself can be monitored as well through structural health sensors or moisture and leak detection. But also, thermography, including drone-based inspections, known as arial thermography, can be especially useful for identifying early-stage degradation and bypass diode failures. The general focus of thermography on PV systems is shifting to autonomous fault detection and classification of PV plants using visual, IRT and aIRT (autonomous IRT) images with accuracies up to 90%, though the autonomous procedure and classification task must still be explored to enhance the performance and applicability of the aIRT method [24]. The IEC 61724-1:2021 standard defines the key terms, required equipment, and procedures used to monitor and evaluate the performance of photovoltaic (PV) systems, however, it does not specifically refer to BIPV applications [67]. Additional literature provides more detailed insights into the monitoring strategies for multifunctional BIPV products [68], [69], [70].

4 Temperature Dependence of PV Modules

In real PV systems, weather conditions such as solar irradiance, ambient temperature, the local wind speed, and the rear surface temperature of the module play a critical role in system performance and are therefore commonly recorded as part of on-site monitoring applications. The energy balance linking environmental variables to the estimation of a PV cell is given by [71]:

$$Q_{solar,abs} = Q_r + Q_{conv} + P_{PV} \quad (4-1)$$

Where $Q_{solar,abs}$ is the solar irradiation absorbed by the PV front surface, Q_r is the long-wave radiation heat exchange, Q_{conv} is the overall heat convection for the front and rear surfaces, and P_{PV} is the output power. However, for building-integrated applications there is an additional heat exchange between the PV modules and the building itself. The following Figure 4-1 illustrates the schematic energy exchange between a PV module integrated into a ventilated facade and its surrounding environment – including the building – highlighting differences between bifacial and monofacial modules.

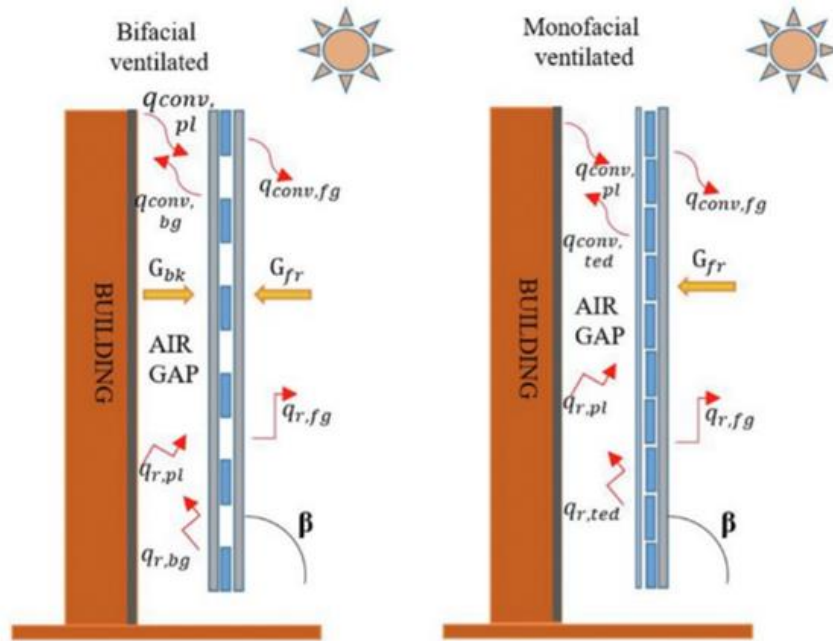


Figure 4-1: Heat fluxes between the PV facade, bifacial (left) and monofacial (right) modules, and the outdoor environment. [72]

In this context, G_{fr} is the solar radiation incident on the front surface of the PV modules, G_{bk} indicates the solar radiation reaching the rear side of bifacial modules. The terms $q_{conv,fg}$ and $q_{r,fg}$ refer to the convective and radiative heat fluxes at the front glass surface of the module. In addition, q_{pl} , q_{bg} and q_{ted} describe the radiative and convective heat exchanges occurring between the two sides of the ventilated cavity. (q_{bg} and q_{ted} both describe heat fluxes dissipated from the modules

rear side, while “bg” stands for back glass and “ted” stands for Tedlar® which is a widely used backsheet material.)

4.1 Heat Sources of a PV Module

By encapsulating solar cells into a PV module, the unwanted alteration of the heat flow into and out of the PV module causes the operating temperature of the PV module to slightly increase. This reduces the voltage of a PV module, resulting in lower power output. Furthermore, elevated temperatures contribute to various defect and degradation mechanisms in PV modules. As a general rule, degradation rates tend to double with every 10 K increase in temperature, primarily because higher temperatures intensify thermal expansion-induced stress within the module materials [73].

4.1.1 Heat Generation of a PV Module

Incident sunlight on a PV module generates heat as well as electricity. Depending on the PV technology, a module operating at its maximum power point typically converts only about 20% of incident sunlight into electricity, while the majority of the remaining energy is transformed into heat [74], [75].

Figure 4-2 a) shows the experimental and simulated external quantum efficiency (EQE) spectrum of a CIGS solar cell, illustrating how efficiently a solar cell converts incoming photons into electrical current across different wavelengths and is defined as [76]:

$$EQE = \frac{\text{Number of electrons collected}}{\text{Number of incident photons}} \quad (4-2)$$

As seen in the graph, CIGS cells effectively convert photons within the range of approx. 400 – 1,100 nm. However, the full solar spectrum extends well beyond this, up to around 2,500 nm, meaning a substantial portion of incoming radiation is either transmitted through the module or reflected, particularly in opaque configurations. Even within the active range, not all absorbed photons are converted into charge carriers. Losses due to recombination and other inefficiencies result in additional energy dissipation. Figure 4-2 b) presents the wavelength dependent absorption coefficient of CIGS, revealing a discrepancy between the absorbed photons and those contributing into electrical output. Photons that are absorbed but not converted, due to sub bandgap absorption, recombination losses or parasitic absorption ultimately contribute to heating the module. Thus, the EQE and absorption coefficient together indirectly provide a map for the spectral origins of thermal energy, which is a key focus of this chapter.

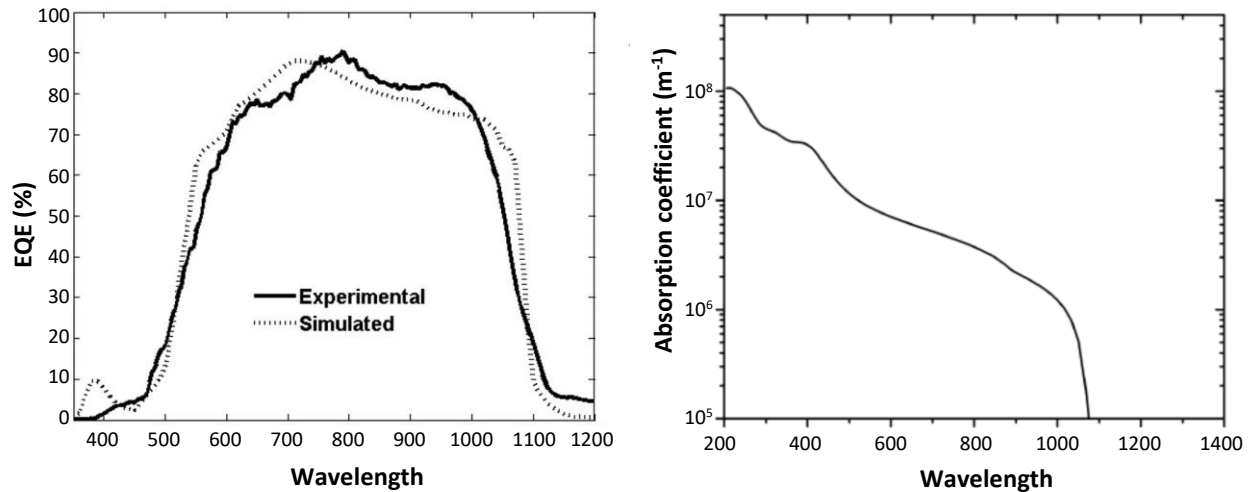


Figure 4-2: a) Simulated and Experimental EQE Spectra of a CIGS solar cell [77], b) Absorption coefficient of CIGS (for a bandgap of 1.2 eV). [78]

The operating point and efficiency of a solar cell determine the proportion of absorbed light that is converted into heat, with lower conversion efficiency resulting in a greater fraction of incident solar energy being dissipated as thermal energy.

When incident sunlight strikes a module, it is either reflected, absorbed or transmitted. As light reflected from the sunlight does not contribute to the electrical power generated, it is considered a loss mechanism that should be minimized. Thus, the maximum temperature rise of a module is calculated as the incident power multiplied by $(1-r)$, assuming transmission is 0. For typical PV modules with a glass top surface, the reflected light contains around 4% of the incident energy. Depending on the angle at which the light meets the module, more or less light is reflected. Ideally, the sunlight should meet the surface of a PV cell at a 90° angle to minimize reflection and avoid losses due to an angle mismatch.

Light absorbed by the cells will be converted into electricity, if the energy is within that of the bandgap of the solar cells. Light, which has an energy below that of the bandgap does not contribute to electrical power, but rather contributes to heating. For PV modules that have an opaque material at the rear side of the cells, infrared light tends to be absorbed here. For CIGS this would be the Mo layer. In PV modules that do not have full rear-side coverage of the solar cells, a significant portion of infrared light may pass through and exit from the rear, depending on factors such as material composition, color, surface texturing, and the installation method. Moreover, non-active components of the module – those not involved in electricity generation – can absorb light across various wavelengths, contributing to the overall thermal load of the module.

PV cells and modules are specially engineered to absorb light with photon energies near the bandgap, optimizing their ability to convert solar radiation into electricity. However, during operation, the cells generate a substantial amount of heat – typically exceeding the temperature of the module’s encapsulation and rear packing layers. A higher packing factor – meaning greater

surface coverage of solar cells within a module – leads to increased heat generation per unit area due to reduced heat dissipation capacity [79].

4.1.2 Heat Dissipation of a PV Module

A key factor influencing the temperature and performance of a PV module is the portion of solar energy that cannot be converted into electricity. This initially absorbed but later “lost” energy is primarily transformed into heat, contributing to thermal buildup within the module and affecting its overall efficiency. The three main mechanisms of heat loss are convection, radiation and conduction.

4.1.2.1 Convection

Convective heat transfer occurs when heat is transported away from a surface due to the movement of a fluid, such as air or liquid, across that surface, facilitating thermal exchange between the material and its surroundings. For a PV module, this would likely be wind blowing across the module surface. The heat transferred by convection is given by equation (4-3):

$$Q_{conv} = (h_{force} - h_{free}) \cdot A_{PV} \cdot (T_{amb} - T_{PV}) \quad (4-3)$$

Where h_{force} and h_{free} are the forced and free convection heat transfer coefficients in $W/(m^2 K)$ and A represents the area of the module. The forced convection coefficient in the plane of the module can be approximated as a function of windspeed v_w proximate to the module as [80], [81], [82]:

$$h_{force} = 6.5 + 3.3v_w, \quad v_w \leq 6m/s \quad (4-4)$$

The free convection for a vertical plane in air can be approximated to by [71]:

$$h_{free} = 1.31 \sqrt[3]{T_{PV} - T_{amb}} \quad (4-5)$$

4.1.2.2 Radiation

Any object will emit radiation based on its temperature. As a result, the PV module itself may transfer heat to the surrounding environment through radiation. The power density emitted by an ideal blackbody is given by Stefan-Boltzmann’s law mentioned in Chapter 2.1:

$$q_{max} = \sigma \cdot T^4 \quad (4-6)$$

Where q_{max} is the radiative heat flux or radiative power per unit area radiating from the blackbody in W/m^2 , σ is the Stefan-Boltzmann constant, which is $5.67 \times 10^{-8} W/(m^2 K^4)$, and T is the absolute Temperature of the surface in K.

However, a PV module is not an ideal blackbody. The equation is modified by a parameter called emissivity ε depending on the material of the object. Emissivity of a grey body lies between 0-1 with an ideal blackbody being a perfect emitter (and absorber) with an emissivity of 1.

The net power lost from a module due to radiation is the difference between the heat emitted from the surroundings to the module and the heat emitted from the module to the surroundings. Considering the area of the module, the power lost can be described as:

$$Q_r = \varepsilon \cdot \sigma \cdot A_{PV} \cdot (T_{PV}^4 - T_{amb}^4) \quad (4-7)$$

Where Q_r is the net power loss of a module through radiation in W, A_{PV} is the area of the module in m^2 , T_{PV} is the temperature of the solar cell in K, and T_{amb} is the ambient temperature. [83] [84]

4.1.2.3 Conduction

Heat losses through conduction occur due to thermal gradients between the PV module and adjacent materials in direct contact. However, these losses are often neglected in simplified models, as their magnitude strongly depends on the specific installation method. The ability of the PV module to dissipate heat into its surroundings is determined by the thermal resistance of the encapsulant materials used to integrate the solar cells into the module, the temperature difference between two zones being the driving factor behind the conductive heat flow. Assuming that a material is uniform and in a steady state, the equation between heat transfer and temperature is given by:

$$\Delta T = \Phi \cdot Q_{cond} \quad (4-8)$$

Where ΔT is the temperature difference between the two materials in K, Φ is the thermal resistance of the emitting surface in K/W, and Q_{cond} is the heat (power) generated by the PV module as discussed in Chapter 4.1.1.

The thermal resistance of a module depends on the thickness and the thermal conductivity of a material. This dependency is described by the following equation:

$$\Phi = \frac{l}{\kappa \cdot A_{PV}} \quad (4-9)$$

Where l is the length of the material through which the heat must travel, κ is the material specific thermal conductivity in W/(m K), and A_{PV} is the area of the surface conducting the heat. [83]

However, the thickness of laminated PV cells is usually very small, around 3 mm. As a result, it is commonly assumed that temperature variations across the module depth are neglectable, allowing heat conduction within the module to be disregarded in thermal analysis [85], [86].

4.1.3 Resulting Energy Fluxes around a PV Module

To better understand the behavior of energy fluxes around a PV module, Figure 4-3 from a study conducted by the Fraunhofer Institute for Solar Energy Systems ISE – presents calculated energy fluxes at both the front and the rear surfaces of a full-cell, glass-backsheet c-Si module. These calculations are based on a module inclination of 45° , which is important to note when interpreting the results.

In BIPV applications, additional thermal interactions occur between the module and the building envelope or the air gap behind the module [72]. These interactions influence heat dissipation on the rear side and must be considered for accurate thermal modeling in such contexts. Therefore, while the results shown in Figure 4-3 offer valuable insight into the distribution of heat flow between the module and its surroundings, they are only partially transferable to the BIPV configuration analyzed in this work.

The simulation assumes a front side irradiance of $1,000 \text{ W/m}^2$ and no albedo. Of this, 892 W/m^2 is absorbed by the module, while the remaining portion is reflected by the front glass, the solar cell surface, or inactive areas of the module. The primary source of heat generation during operation is a result of incomplete conversion of absorbed solar energy into electrical power. [75]

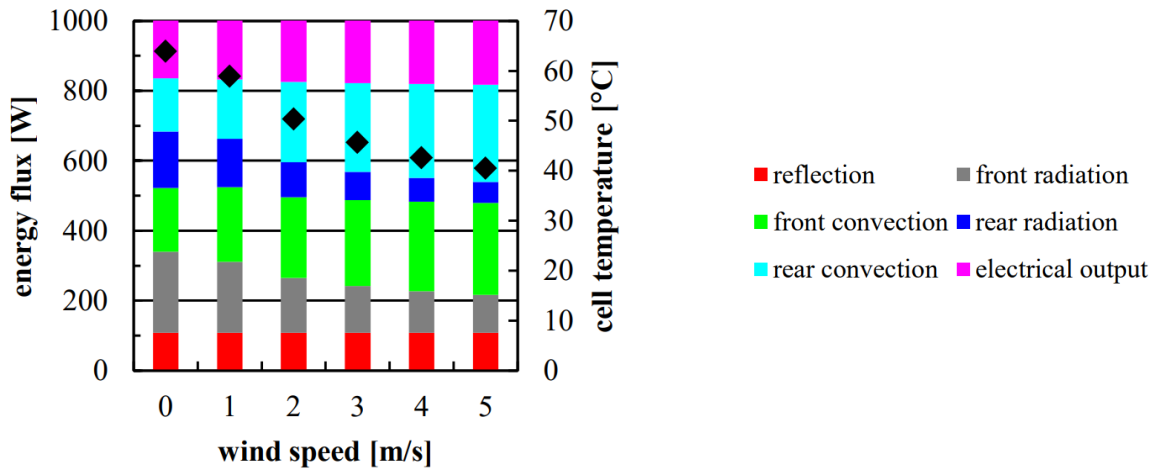


Figure 4-3: Energy flux from radiation and convection at the module front and rear sides for different wind speeds at $1,000 \text{ W/m}^2$, 45° module inclination and 25°C ambient temperature. [75]

Figure 4-3 illustrates the energy fluxes due to radiation and convection at front and rear surfaces of a PV module under varying wind speeds (0 - 5 m/s), with ambient temperature held at 25°C . While wind speed influences the module temperature, it does not affect the amount of energy absorbed. The electrical output varies with the cell temperature and is calculated to range between 164 and 182 W/m^2 . Consequently, the remaining absorbed energy is dissipated primarily through convection and radiation, while conduction is not considered in this particular calculation. An analysis of the outermost interfaces reveals that the front side of the modules accounts for more

than half of the total heat dissipation. As wind speed increases convective heat transfer becomes increasingly dominant over radiative losses. [75]

4.2 Temperature Profile of a PV Module

IR measurements provide insight into temperature variations across the outermost surface of a PV module, but they do not capture the full thermal behavior throughout its depth. The surface temperature of a PV module is primarily influenced by irradiance, ambient temperature, and wind conditions. These factors will first be briefly introduced and then examined in greater detail during the presentation of the results. The internal temperature gradient on the other hand depends largely on the thermal conductivities and heat capacities of the individual layers within the CIGS module, as discussed in Chapter 4.1.

In ventilated facade installations modules often exhibit a temperature drop toward their edges, where convective cooling is more pronounced. The overall temperature distribution across the module plane is strongly influenced by the cell technology [26]. A notable characteristic of CIGS modules is their typically homogeneous temperature distribution across the surface.

In the Fraunhofer ISE study mentioned in the previous chapter, researchers developed a 1-dimensional thermal model to simulate the operational temperature profile of PV modules. Although the model focuses on c-Si modules, its findings are partially applicable to thin-film technologies. While the thermal conductivity of c-Si is relatively high, it is lower in CIGS thin-film modules, which can result in localized heating and the formation of potential hotspots. Structural differences also play a role: c-Si modules generally feature thicker cells and built-in glass-glass or glass-foil configurations, whereas thin-film cells like CIGS are deposited onto substrates such as glass or polyimide. [75], [87]

The CIGS modules examined in this thesis are glass-glass types, which are commonly used in facade applications. Compared to polymer backsheets, glass exhibits a higher effective thermal resistance. As shown in Figure 4-4 (data sets on the right), this leads to a greater temperature drop across the rear glass (0.6 K, indicated by the red-toned data) compared to the backsheet (0.3 K indicated by the blue/grey-toned data). Nevertheless, under conditions without albedo ($A = 0$), the glass-glass module was found to be significantly cooler than the glass-foil variant, due to reduced internal reflection effects. The thermal behavior of full-cell (FC) and half-cell (HC) modules is comparable for both glass-glass (GG) and the glass-backsheet (BS) variations. All configurations show a temperature decrease toward the outer layers, with a further drop toward the front glass compared to the rear. This can be attributed to the increased potential for convective heat transfer. [75]

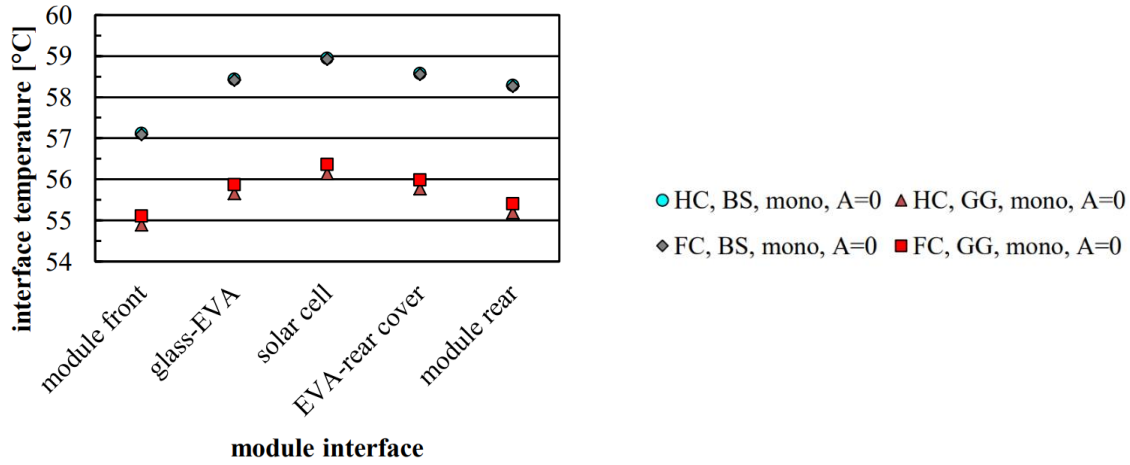


Figure 4-4: Layer temperature in different module setups. [75]

4.3 Effects of Operating and Temperature on PV Performance

The temperature dependency of performance parameters such as open circuit voltage (V_{oc}), short circuit current density (J_{sc}), fill factor (FF) and the maximum power output (P_{max}) or efficiency (η) of multiple PV technologies is investigated in [88] for a temperature range of 273 - 523 K. As the temperature rises, the reverse saturation current increases, causing V_{oc} to drop, which lowers the fill factor and overall efficiency. Meanwhile, the bandgap narrows slightly, which increases J_{sc} and contributed to improved efficiency. However, since V_{oc} decreases more than J_{sc} increases, the net effect is a reduction in solar cell efficiency at higher temperatures. [88]

The behavior of these parameters with changing temperature is quantified using temperature coefficients, which each indicate the change of each parameter per unit change in temperature. A distinction is made between four types of temperature coefficients – one for each V_{oc} , J_{sc}/I_{sc} , FF, and P_{max} , where γ_{rel} describes the relative decrease in power output and efficiency with increasing temperature and will be used throughout this work. The temperature coefficient of CIGS is generally about $-0.36\%/^{\circ}\text{C}$ [89]. The modules used this work specifically exhibit a γ_{rel} of $-0.39\%/^{\circ}\text{C}$ [90].

In practice, the bandgap of semiconductors changes substantially with the temperature. This is due to modifications of the band energies caused by electron-phonon interactions and thermal expansion of the lattice with rising temperatures [88]. There is no general relation between the bandgap (E_g) and the temperature dependency of the bandgap (dE_g/dT). However, for most semiconductor bandgaps an almost linear decrease can be noted with increasing temperatures. There are only few exceptions (e.g. perovskite semiconductor compounds) where the bandgap increases with the temperature. [91]

The temperature of PV modules is influenced by multiple factors, with the mounting type playing a major role. Integrated facade systems demand careful design to ensure sufficient cooling, which is typically achieved in PV curtain walls through rear ventilation gaps. Without such ventilation,

facade-integrated modules tend to reach the highest operating temperatures, leading to the greatest reduction in performance. [92]

4.4 Thermal Cycling Impact on PV Module Degradation

The commercial success of PV systems largely depends on their performance in the field, overall cost and operational lifespan. To enhance viability, it is essential for engineers to investigate and mitigate degradation and failure mechanisms throughout the system's lifetime [64]. PV modules are typically expected to maintain 90% of their power capacity for the first 10 years, and 80% after 25 years [64]. However, these projections are uncertain due to diverse environmental stress encountered during operation. One of the common failure reasons for PV modules is thermo-mechanical fatigue, which is among other things a consequence of thermal cycling. Thermal cycling exposes PV modules to repeated temperature fluctuations, causing expansion and contraction of their constituent materials. This cycle causes mechanical stress due to thermal expansion and contraction of different materials. This mechanical stress is a key driver of long-term degradation, as it can lead to microcracks in solar cells, delamination at module interfaces, fatigue in solder joints, and general loss of electrical contact – all of which contribute to an increase in series resistance. [64], [93], [94] CIGS in particular is affected by high day/ night temperature gradients compared to other technologies [93].

A study investigating degradation mechanisms in CIGS modules through damp heat exposure and thermal cycling observed a reduction in module efficiency in both cases, attributed to increased resistivity in the AZO and CIGS layers. After damp heat exposure, a reduction of the optical band gap was observed and associated with oxygen adsorption and generation of hydroxides in the AZO layer. The increase in resistivity following thermal cycling was also linked to oxygen adsorption as well as the formation of microcracks in the AZO films. [95]

5 Experimental Setup

During the course of the work, the primary focus of the measurements was on the BIPV facade of a particular building. In order to examine and discuss the measurement results from this building in more detail the measurements were extended to additional measuring stations, which are initially described in this chapter.

5.1 The Building - Living Lab PVcomB

5.1.1 The Building Setup

The measurements of the following thesis are carried out on the facades of the “living laboratory” for building-integrated photovoltaics at the HZB in Adlershof, Berlin. This research building with photovoltaic facades provides practical experience on the behavior of solar modules and the entire PV facade system in different seasons and weather conditions over a longer period and is seen in the following image from the southwest corner of the building. The building is divided into two sections – an older part on the east side and a newer part, which houses the PV facade. The total building dimensions are 61.45 x 18.92 x 9.90 m³ [96].

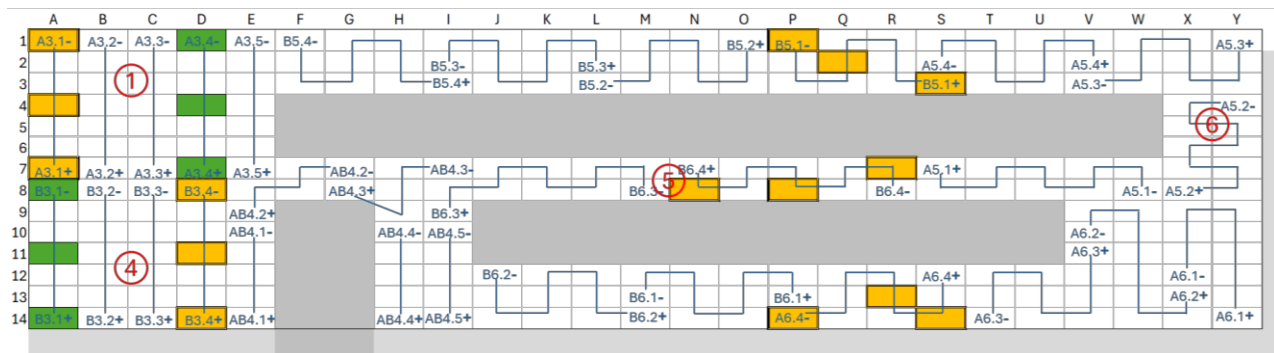


Figure 5-1: HZB Living Lab in Adlershof, Berlin from the southwest corner of the building during morning hours.

The photovoltaic modules have been in operation since June 2021. Since then, the 120 measuring points and sensors have been used to record not only electrical but also physical parameters like temperature, air speed in the ventilation gaps and solar irradiation.

A total of 360 frameless and homogeneously colored CIGS modules (Avancis SKALA 7003) were installed as a ventilated curtain wall. Across the south, west and north facades (south: 248 modules, west: 56 modules, north: 56 modules) a total area of 378 m² is covered with blue tinted PV modules. The north facade is equipped with only four columns of PV modules positioned near the

The system features 6 inverters – one each for the north and west facades and four for the south facade – which convert the DC current generated by the PV modules into AC current suitable for feeding into the electricity grid. This approach enables the collection of as much information as possible to be obtained about relatively small string groups. Each string consist of 7 to 10 modules. The positions of the modules and the way the strings are interconnected can be seen in Figure 5-2 and Figure 5-3 in form of blue lines. The markings at each end symbolize which of the 6 inverters each string belongs to as well as which end is the positive and the negative end of each string. Areas of the facade that are not photovoltaically activated are marked in gray. These include areas that are covered with aluminum modules or areas where windows are located. For clarity in subsequent analysis, each facade is visually divided into a grid, with module rows numbered sequentially from top to bottom and columns labeled alphabetically from left to right.



27

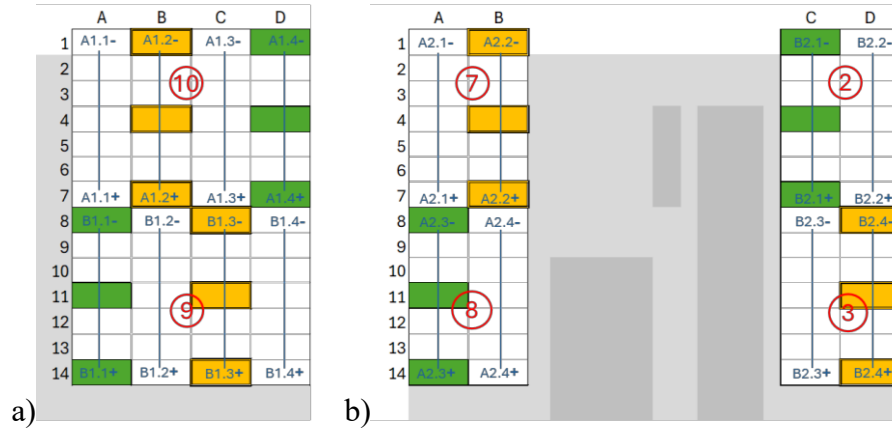


Figure 5-3: String layout of a) north and b) west facades with two temperature sensors on the back side marked yellow (one in the center and one on the edge), with one temperature sensor on the back side marked green (in the center), and the irradiance sensors marked with red circled numerals.

The string layout was designed to group together modules with similar expected performance throughout the day, while also minimizing cable lengths. Accordingly, the assignment of strings to the inverters was carried out in line with this approach. Apart from the module positions and the string layout the figure above shows the positions of the temperature sensors on the modules marked green and yellow. The green modules are equipped with one sensor in the middle of the back side, while the yellow modules have one sensor in the middle and one sensor applied close to the edge of the module. The positions and numbers of the irradiance sensors are indicated by red circled numerals.

5.1.2 Surrounding Grounds and Spatial Limitations

The building is located at the southern end of the HZB research campus. The Teltow canal runs parallel to the south facade about 50 m away from the building, separated by a tree-lined main road as seen in Figure 5-4. With trees along the road and the considerable distance between the water body and the building, the canal's thermodynamic/ reflective effects on the building can be neglected. The north facade faces a neighboring building approx. 9 m tall and situated about 10 m away. Its facade, which is partially painted white and partially constructed from plexiglass, directly faces the Living Lab's north facade, which can roughly be seen in Figure 5-4. The west facade is largely unobstructed apart from a small hill located further away from the facade. The satellite image below shows the Living Lab from a southwest perspective with the PV-active facade area highlighted in red. The resulting spatial limitations influencing the measurement setup are marked blue.

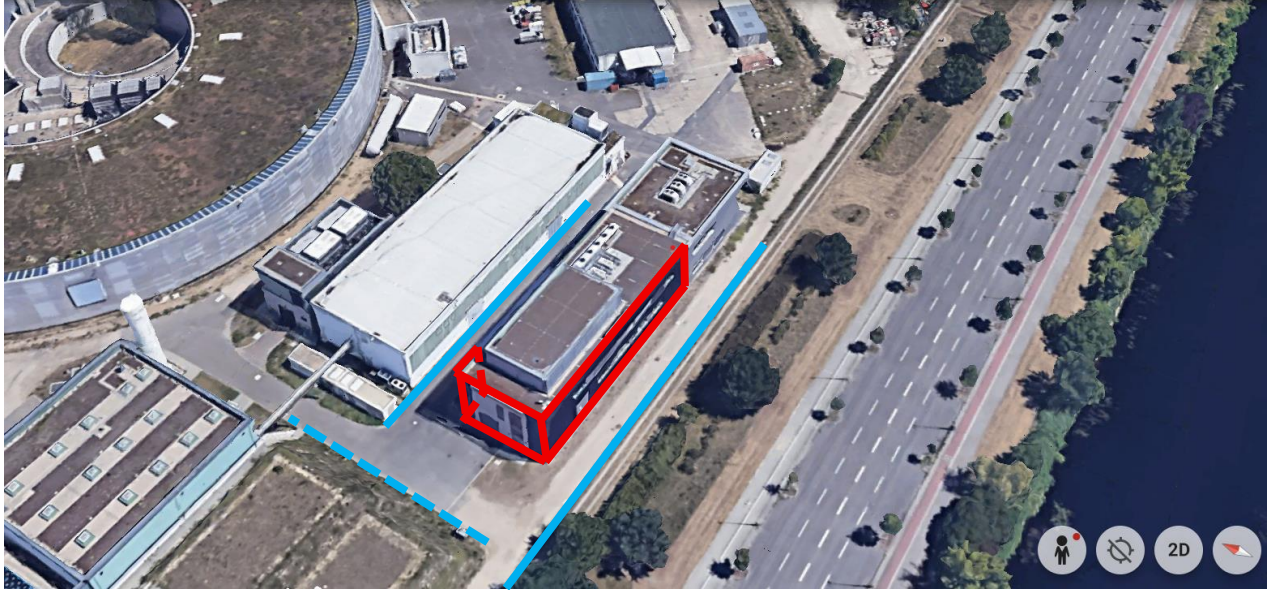


Figure 5-4: Surrounding grounds of the Living Lab and spatial restrictions when measuring the facade. [98]

The variation in viewing angles due to spatial limitations plays a recurring role throughout this work. While a consistent angle is preferred for all IR measurements, spatial limitations in addition to the absence of a zoom function of the camera require manual adjustment of the camera's distance to the target surface. The north and south facades are enclosed by adjacent structures with the consequential boundaries of these spatial constraints marked blue in the image above. The west faced offers a broad open area, with an elevation of approx. 5 m at a distance of 15 - 20 m from the Living Lab. This elevation, marked by the blue dashed line, allows for a full view of the facade, when measuring from a raised level, though it introduces additional factors into the measurement frame that may influence the obtained data.

5.1.3 The Modules and the Mounting System

As mentioned, the modules used are the Avancis SKALA in the shade blue (7003). The CIGS modules are visually uniform under direct view but exhibit angle-dependent color shifts as shown in the following picture. Additionally, their matt finish hides the CIGS cell structure.

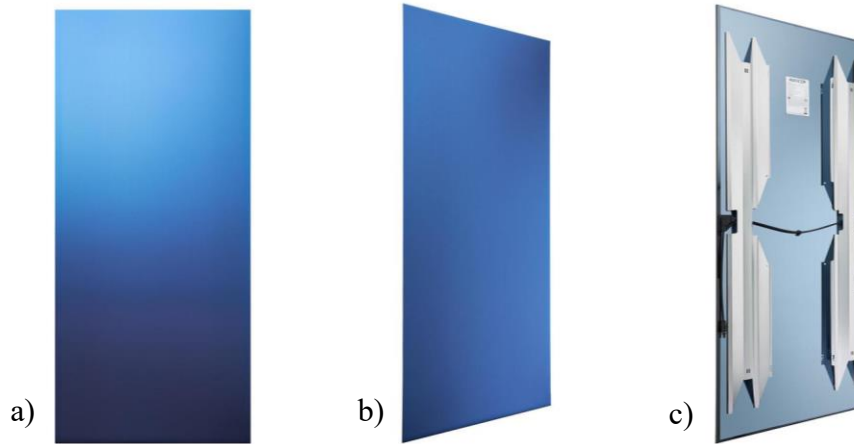


Figure 5-5: Avancis SKALA Module in the shade blue 7003 from a) the front, b) the side, and c) the back view including part of the mounting system. [99]

The modules are frameless, opaque glass modules, which is one of the key reasons for their selection. Their nominal power of 130 – 135 Wp depending on the manufacturing batch (130 in batch V 4.6.47 and 135 in V 4.6.6.) with a manufacturing tolerance of -5%/ +10% reflects the dimensions of 1,587 x 664 mm with 135 cells running horizontally and connected in series [90]. The temperature coefficients of the modules are the following: $\gamma_{rel} = -0.39\%/^{\circ}\text{C}$, $\beta_{abs} = -230 \text{ mV}/^{\circ}\text{C}$ and $\alpha_{abs} = 0 \text{ mA}/^{\circ}\text{C}$, where β_{abs} and α_{abs} represent the absolute temperature coefficients for the V_{oc} and I_{sc} [90]. As the mounting system is fully concealed – an additional reason for their selection – the result is an even facade appearance. The installation uses a backrail system designed for hock-in mounting within a standard facade substructure, creating a rear ventilated facade configuration. The primary purpose of the modules is weather protection, which is why the air gap on the rear side of the modules meets the unprotected insulation on the building side. The front glass features a matt structure giving the modules a homogenous look and concealing the PV cells from view, which only become visible at close range. Unfortunately, the matt structure of the front glass surface causes diffuse radiation, which is not ideal for thermography. The modules have a BIPV type approval, confirming that the product meets specific technical standards and legal requirements for facade integration. Further detailed technical data about the modules used can be found in Appendix A2.

According to the official datasheet and installation manual the SKALA module is a glass-glass CIGS thinfilm module with the following structure: front and rear glass is a 3.0 mm thick tempered safety glass providing mechanical protection and optical clarity. Avancis does not explicitly state whether the color layer is directly behind the front glass or embedded deeper [90], [100]. Yet given the matte and homogeneous surface, and the emphasis on color uniformity, it is likely that the coloring layer is a thin coating applied directly to the inner side of the front glass. The active CIGS layer is applied to a rear substrate, which means that thin-film modules only require an encapsulant on the front side to ensure adhesion and moisture protection [12], [59].

5.1.4 Obtaining Infrared Data on the PV Facade

This work focuses on the acquisition of infrared thermography data from a PV facade, with the following chapter detailing the measurement procedure. As the majority of measurements were conducted on the south facade, the setup described here is based on that orientation but structured to be transferable to the east and west facades as well. For this specific experimental setup, the camera does not have a zoom function in a way that the image section can be enhanced or vice versa while the camera position remains the same. To ensure conditions in which the images are obtained in a way to view the facade system completely, the following method was applied.

As emissivity has an enormous impact on the temperature reading captured by the FLIR (forward looking infrared) camera, it is essential to consider the angle at which the camera is positioned relative to the plane of the PV module. As discussed above, the emissivity value of glass varies depending on the angle. As all recordings were taken from the ground level, a certain change in angle must be accepted, however, taken into account as shown in the following Figure 5-6.

The following image depicts the measurement setup: on the left, the IR camera is mounted on a tripod positioned approx. 5 m from the south facade, visible on the right side of the image. The camera is connected to a laptop running the appropriate software for real-time data evaluation. The tripod allows for adjustment along all three axes, enabling the camera to maintain a consistent position when repositioning and adjusting the frame during measurements. The image was taken during late morning hours, as indicated by the camera's shadow cast by the sun positioned in the southeast.



Figure 5-6: Measurement setup for the south facade.

The image clearly shows that following the recommendation to measure perpendicular to the module surface is only feasible for the lowest module row. For the top row, the angle drops below

30°, as the ability to move further back is limited by the fence on the left side of the image above. Maintaining an angle greater than 30° was only possible for the west facade, as access on the north side is restricted by a neighboring building.

5.2 HZB Outdoor Performance Laboratory

As none of the modules installed on the Living Lab were damaged and the effects of a damaged module were supposed to be analyzed, a damaged module that recently was removed from the facade was inspected. It was mounted in the HZB outdoor performance laboratory on the roof of the “Zentrum für Photovoltaik” (ZPV) building. The modules are installed on a substructure for the examination of industrial PV modules at a 90° angle simulating a facade integration in terms of their orientation for the IR measurements. The measurement setup can be seen in the following image. This clearly demonstrates the different ventilation conditions on the backside of the modules compared to an actual facade integration, as the rear surface is almost as exposed to cooling wind as the front, with only the mounting rails providing some restriction.



Figure 5-7: Measurement setup at the HZB outdoor performance laboratory measuring module 0069.

When measuring on the roof of the ZPV the space was restricted by other modules, as they are mounted in long-term test setups, and by the shape of the roof. What immediately stands out are the modules with an incline positioned between the camera and the measured modules. These can cause external reflection disturbing the image, yet they were not seen in the measurements taken. Positioning the camera in front of these modules allowed close-up measurements of the relevant modules.

5.3 Measuring Tools

5.3.1 FLIR Camera and Software “FLIR ResearchIR Max”



Figure 5-8: FLIR 6700sc [101]

The IR camera used during measurements is the FLIR A6700sc by Teledyne FLIR LLC and is displayed in Figure 5-8. This cryogenically cooled infrared camera features a cooled indium antimonide (InSb) detector operating in a wavelength range of 3 – 5 μm and therefore measuring the short-wave area of the IR-C range. The camera captures detailed data with 327,680 pixels and, among other qualifications, is specifically designed for non-destructive material testing – ideal for evaluating PV modules. It allows both still images and movie recordings, adaptable to various measurement requirements [101]. The camera is mounted on a tripod, providing maximum flexibility in its orientation during measurements. (Further details can be found in Appendix A2.)

The data can be evaluated in real-time using the camera or analyzed at any later point using the FLIR ResearchIR Max software. This enables detailed data analysis at pixel level and the generation of real-time graphical evaluations. The temperature scale can be adjusted to the temperature range needed, with the pixel distribution visible in the image enhancement section. In the following image a screenshot of the software interface is displayed with the image enhancement section at the bottom.

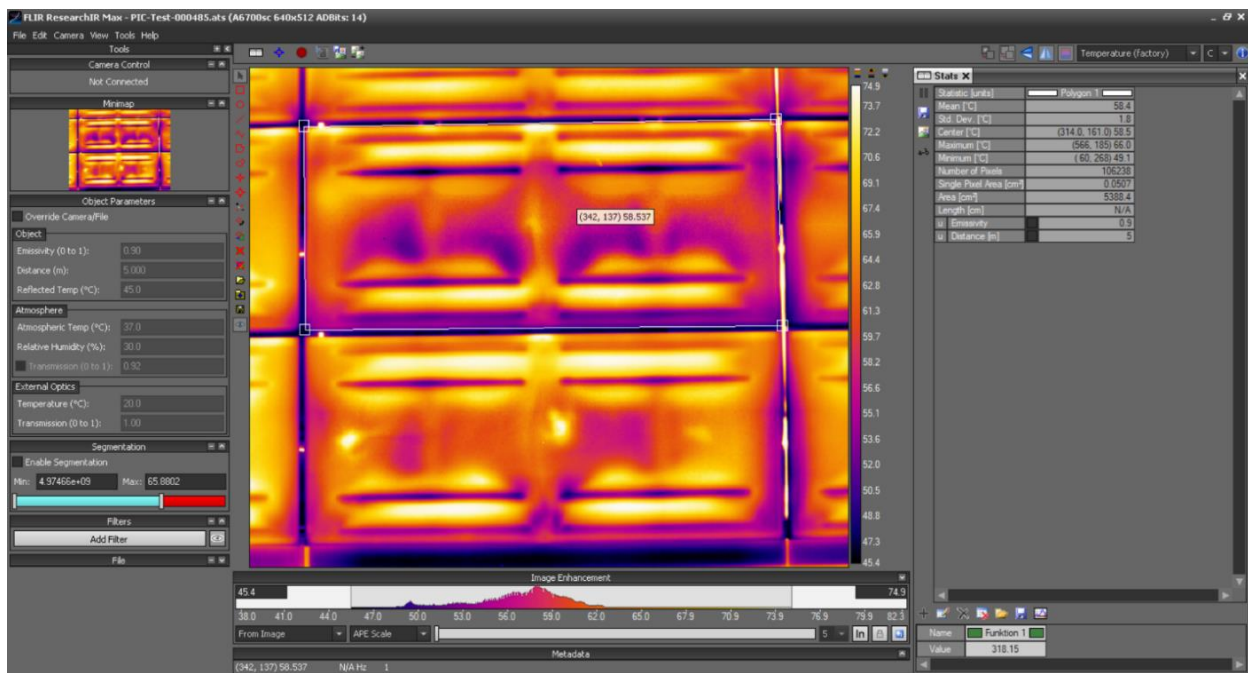


Figure 5-9: Software environment to evaluate IR measurement data.

Data can be recorded and saved or exported as .ats-data, allowing it to be reloaded into the software at a later time while retaining most of the software's functionality. While image enhancement techniques can be applied retrospectively, object parameters must be set before measurement, as they significantly influence the absolute temperatures recorded by the camera. The software includes multiple image enhancement algorithms that improve thermogram contrast and clarity while maintaining temperature accuracy. Its Automatic Gain Control (AGC) setting allows users to regulate how color is mapped to thermal data. Among the three AGC algorithms the APE setting was used continuously throughout this work. Image subtraction or addition is a further option to amplify anomalies. This method is only suitable for extremely stationary measurements, which were not performed in this study. However, it could be valuable in future work, as temperature differences in a CIGS PV facade are often too subtle to be detected due to more dominant effects – effects that could potentially be eliminated through image subtraction.

5.3.2 Built-in Sensors of the PV Facade

The temperature sensors used for installation on the rear of the module are the DS18B20 Programmable Resolution 1-Wire Digital Thermometer. The 1-Wire interface requires only one port pin for communication and has an accuracy of 0.5°C between -10°C to $+85^{\circ}\text{C}$ [102]. Each sensor measures the temperature at its respective measuring point every 2 minutes, with the data then assigned to the corresponding sensor ID.

Ten irradiance sensors are mounted across the building's facades: each attached to the front side of the modules at the corners. They measure the plane of array irradiance (G_{POA}), which is the irradiance received directly on the surface of a PV module. This includes direct beam irradiation, diffuse sky irradiation and reflected albedo irradiation from the ground and the surrounding surfaces. The sensors are compact enough to be installed at the edge of the modules, positioned in inactive areas to avoid shading the active cells and thereby prevent any impact on the module's performance. The sensor is displayed in Figure 5-10 with its dimensions.



Figure 5-10: Irradiance sensor ML-02/ EKO-Instruments used on the Living Lab with dimensions. [102]

Irradiance data was measured at 1-minute intervals with a sensitivity of approx. $50 \mu\text{V}/\text{W}/\text{m}^2$. However, the sensors only measured within the wavelength range of 400 – 1,100 nm, rather than capturing the entire solar spectrum [102].

5.3.3 Miscellaneous Measuring Tools

To tailor the object parameters to the specific measurement conditions, ambient temperature and relative humidity were recorded using a digital thermo hygrometer from TFA Dostmann. This device (seen in Figure 5-11) is suitable for temperature ranges between -30°C and $+60^\circ\text{C}$ and humidity levels from 20% to 90% relative humidity. The sensor offers an accuracy of $\pm 1^\circ\text{C}$ within the 0°C to 50°C range and $\pm 5\%$ RH for humidity measurements between 30°C and 80°C [103].



Figure 5-11: Digital thermo-hygrometer 30.5048 from TFA-Dostmann.[103]

A type K thermocouple was placed at the edge of the module's front glass to provide a reference temperature for comparison with IR measurements. Type K thermocouples are among the most widely used due to their broad operating range and reliable performance. Constructed from nickel-based alloys, they offer good corrosion resistance and can measure temperatures from -270° to $+1,260^\circ\text{C}$. Within the relevant range of 0°C to 275°C the sensor provides a typical accuracy of $\pm 2.2^\circ\text{C}$ [104].

5.4 Flash Testing and Electroluminescence Measurements

In addition to IR imaging, the electrical parameters of selected modules were examined using a flasher in collaboration with HTW Berlin, and electroluminescence (EL) measurements were performed in the same setup.

Flash testing enables the measurement of module performance under standard test conditions or low-light scenarios, ensuring comparable results. Flash testing is the process of exposing a PV module to a short – in this case 10 ms – and bright flash of light from a xenon filled lamp, while the spectrum of the lamp resembles the spectrum of the sun as accurately as possible. With correct calibration this method allows to measure the modules electrical characteristics like current and voltage at maximum power (I_{mpp} and V_{mpp}), open circuit voltage (V_{oc}), short circuit current (I_{sc}), maximum power (P_{mpp}) and fill factor (FF). By varying the intensity of the flash the behavior of these parameters can be mapped at different irradiation levels. [105]

The set-up of the PV module in the dark room for both measurements can be seen in the following image. The dark room ensures that no external factors disturb the measurement.

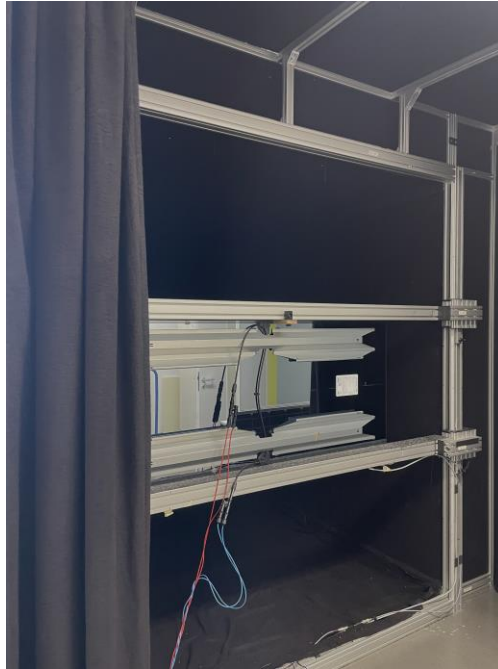


Figure 5-12: Construction of the module in the dark room of the flasher at HTW Berlin before closing the curtains.

Electroluminescence is the emission of light from a semiconductor when an electric current or field is applied. It is caused by radiative recombination: when electrons in semiconductors are excited to a higher level of the bandgap (to the conduction band), they leave behind holes in the lower energy level (the valence band). When the electron falls back into a hole, it releases energy in form of a photon (light). Consequently, light is emitted, when electrons and holes recombine. Non-radiative recombination is energy released as heat or vibrations – its thermal consequence is visualized by IR measurements.

For PV modules a voltage is applied in the dark to force radiative recombination. EL imaging reveals microcracks, broken fingers, or bus-bar interruptions, as well as shunts, inactive (dark) cells or strings, and cell-to-glass delamination. It is also used to identify early signs of potential-induced degradation and other hidden defects in PV cells or modules [26], [106]. Combining flash test measurements and EL measurements with IR measurements of the PV modules, allows to identify electrical anomalies and to quantify their impact on the module performance. By overlapping IR and EL images, the precise locations of defects can be compared and discussed with greater accuracy.

6 Measurement Procedure

With the relevant measurement setups established, the following section outlines the methodology used to acquire the infrared data. A clear understanding of the measurement procedure is essential to later evaluate which factors may have influenced the results and to what extent. Particular attention is given to environmental conditions, equipment handling and procedural consistency, all of which play a critical role in the reliability of the thermographic data.

6.1 How to Interpret the Data

When interpreting IR images, it is important to recognize that observed effects may result from external influences – such as mounting systems or reflections – or from internal factors like damage or nonfunctional components within the module. External impacts that are visible in IR images amount to various reflections, such as those from the horizon, clouds, surrounding buildings, as well as surface contaminants like dirt or bird droppings.

Especially in thermography of BIPV systems – for example, on facades where modules are often installed vertically, reflections play a key role and can significantly influence image interpretation. In comparison to the typical 30°-orientation of roof and free-standing PV installations, the reflective “clean” zenith of the sky is replaced by a disharmonious horizon for facade applications. The following illustrations demonstrate this relationship with the IR measurement setup at the south facade on the left in comparison to reflection angles for measurements on a tilted module on the right.

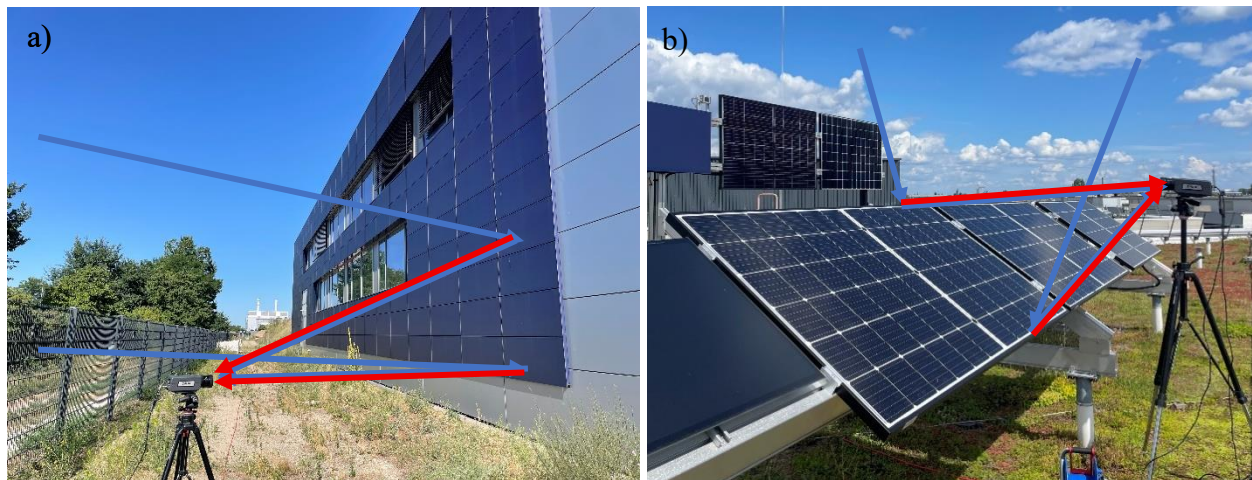


Figure 6-1: Relevance of the vertical orientation of most facade modules for IR measurement, b) facade modules with reflection of the horizon in comparison to a) 34°-angled modules with reflection of the (ideally cloudless) zenith, where the blue arrows represent the reflected ambient radiation and the red arrows represent the actual module radiation.

The orientation and the weather conditions are thus crucial for the data interpretation. When measuring exactly perpendicular to a module’s surface, a reflection of the camera and people standing behind the camera is likely to obscure the image data as well and needs to be identified.

This is why, following the recommendations of other studies, measurements taken close to 90°, but not exactly at 90° [106]. In addition, the Avancis modules (seen in Figure 6-1 a)) in the facade of the Living Lab have a highly structured surface and an increased proportion of nondirectional reflection.

6.2 Absolute Temperatures

Thermography is a reliable technique for detecting relative temperature differences. However, accurate absolute temperature measurements require consideration of environmental factors such as ambient temperature and sky coverage. Emissivity is the primary parameter that can be directly configured in most IR analysis software. Emissivity depends not only on the material and surface characteristics, but also varies with the angle of observation. For most common solar glasses, emissivity starts close to 0.9 when viewed perpendicularly. However, as the viewing angle decreases, emissivity drops significantly, causing infrared cameras to register a lower apparent temperature. [36], [38]

When measuring PV modules on a facade, the main challenge lies in capturing each module from the same angle, ensuring consistent emissivity settings across all measurements. Ultimately, capturing the entire facade with accurate temperature readings is not feasible, as the infrared camera is typically positioned at ground level, resulting in oblique viewing angles that affect emissivity and temperature accuracy. When recording the entire facade, the camera is always positioned at ground level (the change in viewing angle is illustrated in Figure 7-3 and Figure 7-4), the impact of its positioning is discussed in greater detail during data interpretation. In each measurement series, efforts were made to vary the viewing angles within a limited range, as outlined in Chapter 7.1.2, to introduce a level of consistency across the dataset. This approach facilitates more reliable comparisons between results.

The glass structure of the modules front glass is a matt structure providing a diffuse reflection, which is not ideal for IR measurements. To validate the recorded temperatures, a thermocouple was mounted on the front side of the module, positioned at the edge where the surface is non-active, ensuring it does not interfere with the active cell area (see Figure 6-2). The thermocouple was mounted using insulating tape and thermal paste¹. The temperature recorded by the thermocouple was compared with the IR reading from the same region. On a module not exposed to direct sunlight, the two measurements closely aligned: the IR camera registered approx. 24.6°C, while the thermocouple measured 23.7°C on 02.06.25 at 12:08 in the west facade – yielding a temperature difference of less than 1 K. In contrast, when measuring a module under direct irradiance, the discrepancy increased. The thermocouple indicated 40.2°C, whereas the IR camera showed 42.5°C on 20.05.25 at 12:37 in the same region of interest (ROI), resulting in a difference exceeding 2 K. Although the observed deviation remains within the sensitivity limits of both the

¹ which is an arctic cooling silicon heat sink compound consisting of 50% silicone, 20% carbon, and 30% metal oxide [107]

IR camera and the thermocouple for shaded and unshaded regions, the temperature difference more than doubles in areas exposed to direct sunlight. Comparable discrepancies have been observed under similar conditions, suggesting that reflective effects may be influencing the IR measurements.

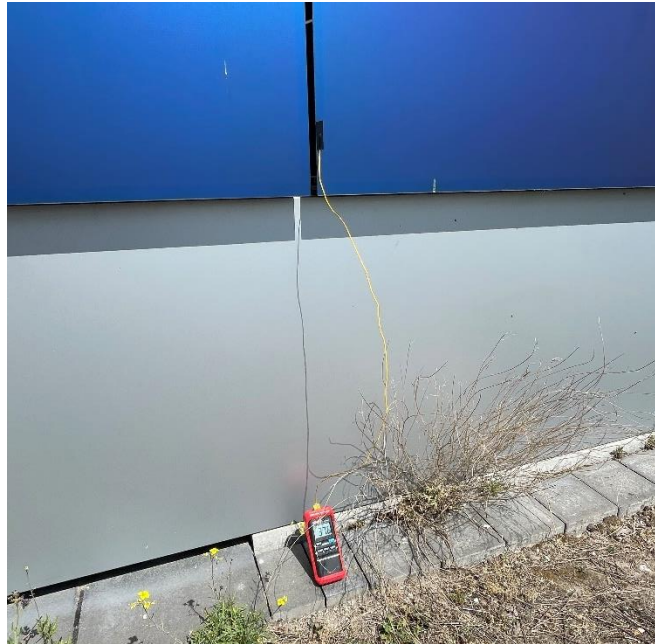


Figure 6-2: Thermocouple setup on the inactive area of the module.

When comparing temperatures recorded by an infrared camera or thermocouples mounted on the front glass of a PV module with data from temperature sensors installed on the back side, it is important to account for the inherent temperature difference between the front and back of the module. In a monocrystalline BIPV application used as a reference, the backside of the module is typically about 0.5 - 1 K warmer than the front glass. The solar cell itself tends to be approx. 0.5 - 1 K hotter than the backside. These temperature differences become more pronounced when the front side is windward, and conversely, may decrease when the wind has a less cooling effect. [49]

6.3 Image Processing after Measurements

During the measurement process, images were saved in form of .ats files, allowing the files to be reloaded into the analysis software. This format preserves most processing options and enables access to the raw data at any later point, ensuring the most accurate and flexible post-processing possible. It is important to note that calibration must be performed prior to measurement, as it cannot be adjusted retrospectively. To analyze specific data within a measurement, such as isolating the temperature data of a single module in the facade, regions of interest (ROI) can be marked using polygonal shapes to trace the module's edges. ROI-specific data is displayed immediately, allowing for initial assessments, as shown in Figure 5-9. Additionally, .csv and .tif

files were saved to enable further analysis on devices that do not have access to the proprietary software.

For measurements with a lot of background noise, for example a cloudy sky that could not be avoided, the temperature scale was sometimes adapted manually to emphasize the modules temperature range and make smaller temperature changes more visible. The exemplary result of adapting the temperature scale can be seen later in Figure 7-21 b) cutting out all temperatures below 37.8°C.

When visualizing infrared measurements APE was used constantly as an AGC algorithm together with the default set color palette called “fusion”.

6.4 Limitations during Measurements

Due to previously discussed spatial limitations, capturing the entire facade in a single measurement is not feasible without introducing extreme viewing angles, which distort the results. As discussed in Chapter 5.1.2, specific spatial limitations around the building restrict the OR camera’s positioning, allowing only relatively small sections of the facade to be measured at a time. Measurement of the west facade with the most spatial freedom allows larger facade areas to be measured at once with a close to perpendicular orientation. However, it is still not possible to measure the entire west facade in a single recording.

As discussed in Chapter 2.5 specific weather conditions are suggested, when measuring, to exclude as many external factors from the measurements as possible. This results in a certain dependance on weather – especially regarding the degree of cloud coverage. Measuring with a minimum irradiance of 600 W/m² in the module plane is not achievable during summer months for the south facade, as the position of the sun is too high. Consequently, a clear sky was more important, to get as close as possible to the desired irradiation minimum.

Surface interference was also an unavoidable factor. Since the effects of dust and other contaminants, such as bird droppings, on the module’s temperature dependance were to be analyzed during these measurements, these factors also emerged as very dominant influences. Consequently, it is recommended by DIN IEC/TS 62446-3 to clean the modules prior to IR measurements unless localizing critical pollution is the goal of the measurement.

Furthermore, there was limited access to the rear of the modules to verify any assumptions when analyzing the measurement results, as they are part of an active system. Inspecting the rear would require at least a lifting platform and the interruption of operation. The rear of the modules could only be inspected in the setup of the ZPV roof. However, thermography on the module backsides is ineffective due to highly reflective, almost mirror-like back glass, which primarily reflects the camera’s background rather than revealing thermal features of the module itself.

6.5 Mitigation Strategies during Measurements

To minimize the impact of limiting factors, the following mitigation strategies were applied.

Since the entire facade could not be captured in a singular recording – which would have resulted in varied viewing angles of each module regardless – each module was instead recorded from the same or similar angle. This was done as much as possible by measuring each module from the ground. As a result, each module was measured both from the front and from the side with an offset of 45° , varying only the angle between ground plane and facade plane. This approach is discussed more thoroughly in Chapter 7.1.2 as the procedure is essential to data interpretation. Consistent measurement angles and their careful documentation contribute to limit the varying factors needing consideration during the interpretation of anomalies. Calibration routines like feeding the software with parameters such as the expected emissivity, ambient temperature and humidity add to comparability between the individual modules.

If anomalies are measured, identifying them under varying conditions can exclude certain external factors being the cause. Measuring at varying times and even seasons and weather conditions can rule out most reflection factors surrounding the PV module if not stationary. In this case documenting these influencing factors like clouds is crucial for later interpretation.

Image subtraction or enhancement techniques can be applied to reduce noise or isolate the patterns discussed above. Nonetheless, these techniques are only meaningful for very stationary measurements conducted over extended periods – typically several hours – and were therefore not applied in this work.

7 Results and Evaluation of Measurements (Analytics)

The discussion of the results will begin with data interpretation, followed by an assessment of their significance for PV modules and systems. Finally, the measurement uncertainties identified during the process are put into perspective as future guidelines.

7.1 Interpretation of Data

7.1.1 IR Measurement at Modul Level

To examine IR measurements at module level the upcoming chapter focuses on the measurement of module P13 as a representative example. The position in the facade is low enough for a near optimal viewing angle with the IR camera while avoiding edge effects. Modules located at the facade's perimeter tend to exhibit different thermal behavior due to increased convection and reflective interactions. Additionally, the adjacent modules to the right and below are equipped with temperature sensors for reference. Notably, placing sensors directly on the module's back surface itself would interfere with the IR image as seen in the bottom of Figure 7-1.

When analyzing an IR recording at module level (Figure 7-1), it becomes immediately apparent that the most dominant factor in every IR measurement of the Avancis SKALA module is the back rail mounting system. The main cause is the cooling of the regions in direct contact to the metal backrails, as indicated by green arrows in Figure 7-1. Ultimately, the regions where the backrails are glued to the back glass and the reduced convection in the areas between them, result in a pronounced temperature difference. A more thorough discussion of the backrails can be found in Chapter 5.1.3. The effect of this can be seen clearly in the following figures.

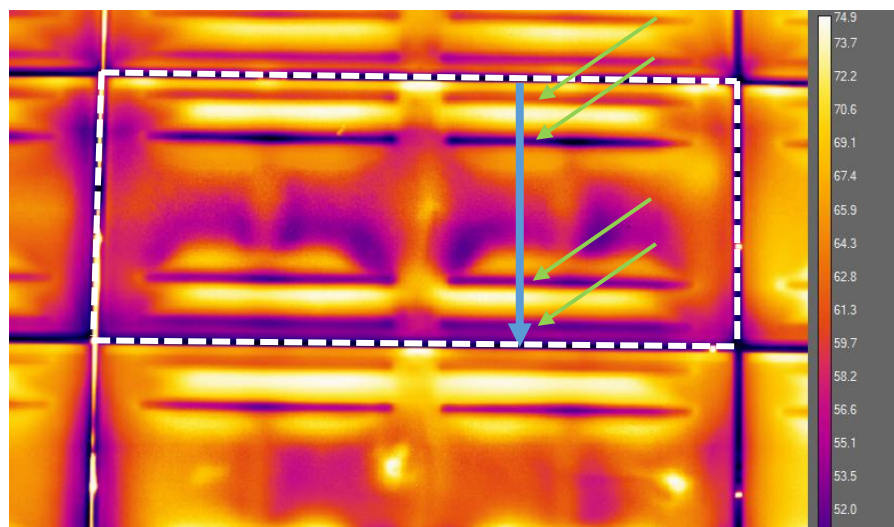


Figure 7-1: IR picture of module P13 along the south facade while P13 is marked with a white dashed outline and the line scan analyzed in Figure 7-2 marked light blue.

Figure 7-1 presents an IR image of module P13 taken from the front under ideal weather conditions. The ambient temperature was 30.6°C, while the mean module temperature was 58.0°C. The dominant pattern of the backrails running horizontally at the top and bottom part of the module can clearly be observed. Also, the cabling running vertically along the center of the module can be seen due to reflection of radiation on the back side of the module. The temperature behavior of one pixel column from top to bottom is illustrated in the following picture for an area of the module affected predominantly by this phenomenon. It is marked in Figure 7-1 by a blue arrow.

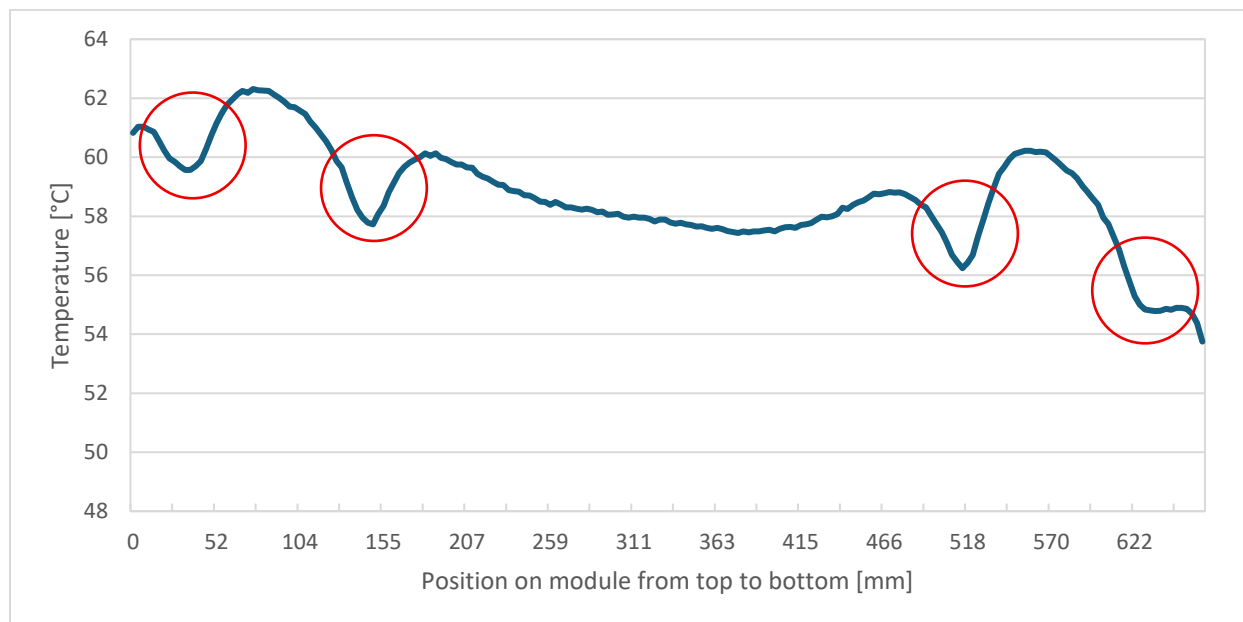


Figure 7-2: Temperature course from top to bottom of module P13.

A clear temperature dip can be observed in the areas of direct contact having a cooling effect on the area. In the “tunnel” of the backrail a temperature rise of about 2 K is visible due to less convection as discussed above. However, a slight temperature increase in the regions immediately adjacent to the contact areas on the outer sides (at positions around 10 mm, 170 mm, 470 mm, and 650 mm) can be determined – the reason likely being either reduced convection because of limited air flow or reflection of the backrails in these areas. Overall, a temperature drop from the top to the bottom of the module can be registered. This is likely due to the angle of the sun, the position of the sun at the time of the recording (13:05) being very high.

Although the manufacturer Avancis has made several attempts to enhance air circulation and thereby promote forced convection to passively cool the “tunnels” within the backrails, no effective solution has yet been found to prevent excessive heating in these areas [108].

To put the absolute temperatures discussed into context, they are compared to the temperatures measured by the sensors on module P14 (below P13) and on module R13 (to the right of module P13). The sensors on module P14 measured 52.81°C at the center and 53.25°C at the edge on the

rear side. Considering the typical temperature difference between the front and the back of the module, approx. 1°K must be added to the reading for direct comparison with the front side measurements. Furthermore, a temperature of 55.00°C was recorded at the edge of module R13, while the central sensor on its backside was nonoperational at the time. Assuming R13 exhibits similar thermal behavior to module P13 and the edge tends to be roughly 0.5 K cooler than the center, the IR camera readings are about $1 - 2\text{ K}$ higher than those from the sensors. This aligns with the thermocouple reference measurements discussed in Chapter 6.2. One possible explanation for this discrepancy is the influence of reflected radiation from the surrounding surfaces, such as the ground, which likely has an albedo of $0.17 - 0.26$, but changes with every measurement position. If the environmental conditions are unknown, a value of $A = 0.2$ is commonly used, falling into the range of the albedo for this environment [39].

7.1.2 IR Measurement at System Level

To gain insight into the interaction between modules and strings at system level, the thermographic data from each individual module along the south facade was compared. This chapter presents the results by displaying the mean temperature value for each module across a facade.

7.1.2.1 Angle Variation during IR Measurements on the Facade

In order to more accurately distinguish angle related effects from actual thermal effects, each module was measured twice: once at a 90° angle, in accordance with the relevant standard to a limited extent [38] as well as with a 45° offset. The following illustration shows the measurement setup with a perspective from the top for each measurement. In this illustration, the red module on the left represents the unit captured by the IR camera:

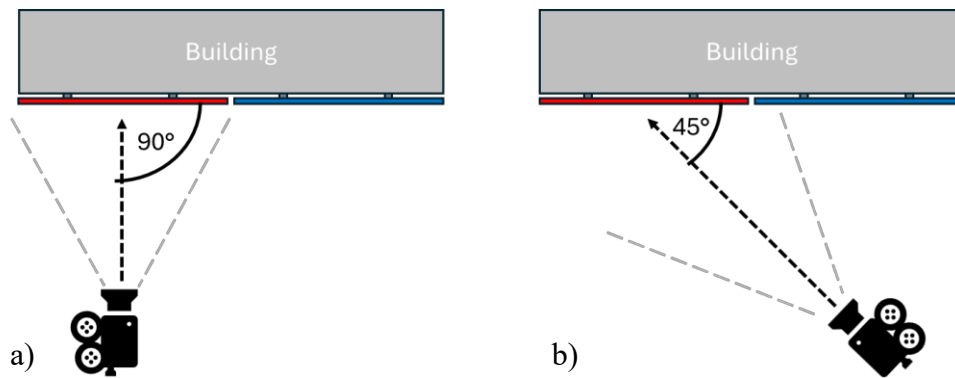


Figure 7-3: Top view illustration of the measurement setup with the module being recorded by the IR camera positioned on the left side and marked red, a) being the setup as in Figure 7-5, and b) being the setup as in Figure 7-6.

The measurements were conducted over the course of an entire day. Data was collected column by column from right to left, with each column measured from bottom to top. The time stamp for the start of the measurement of each column is noted at the bottom of Figure 7-5 and Figure 7-6 together with the corresponding irradiance measured by the closest sensor at that time.

As mentioned before, all measurements were conducted from ground level. Thus, while the recording angle relative to the ground plane remains constant – as shown above – the angle between the camera orientation and the plane of the facade or module decreases as the module’s height increases – as shown in Figure 7-4. Starting at around 90° to the center of the module – as recommended in IEC/TS 62446-3 – the measurement angle for the lowest modules in row 14 gradually decreases to about 24° for the top row, as shown in Figure 7-4, with $\delta_{14} \approx 90^\circ > \delta_i$. Due to the constraints of the measurement environment, it was not possible to maintain a precise measuring angle of 90° . As a result, only an approximate angle could be achieved.



Figure 7-4: Visualization of camera angle changing according to height of module position, δ represents the angle of the camera to the plane of the module, and the index i indicating the position of a module in a column.

Figure 7-5 displays the mean module temperatures (in degrees Celsius) of each module across the facade, based on measurements taken using the 90° setup illustrated in Figure 7-3 a). The color gradient ranges from dark red, indicating the highest recorded temperatures, through yellow down to green for cooler temperatures. For better orientation on the facade, the module positions are labeled numerically and alphabetically as introduced in Chapter 5.1.1. Additionally, the figure includes the locations of the windows (dark grey), temperature sensors (single frames for one sensor and double frames for two sensors) and irradiance sensors (red circled numbers).

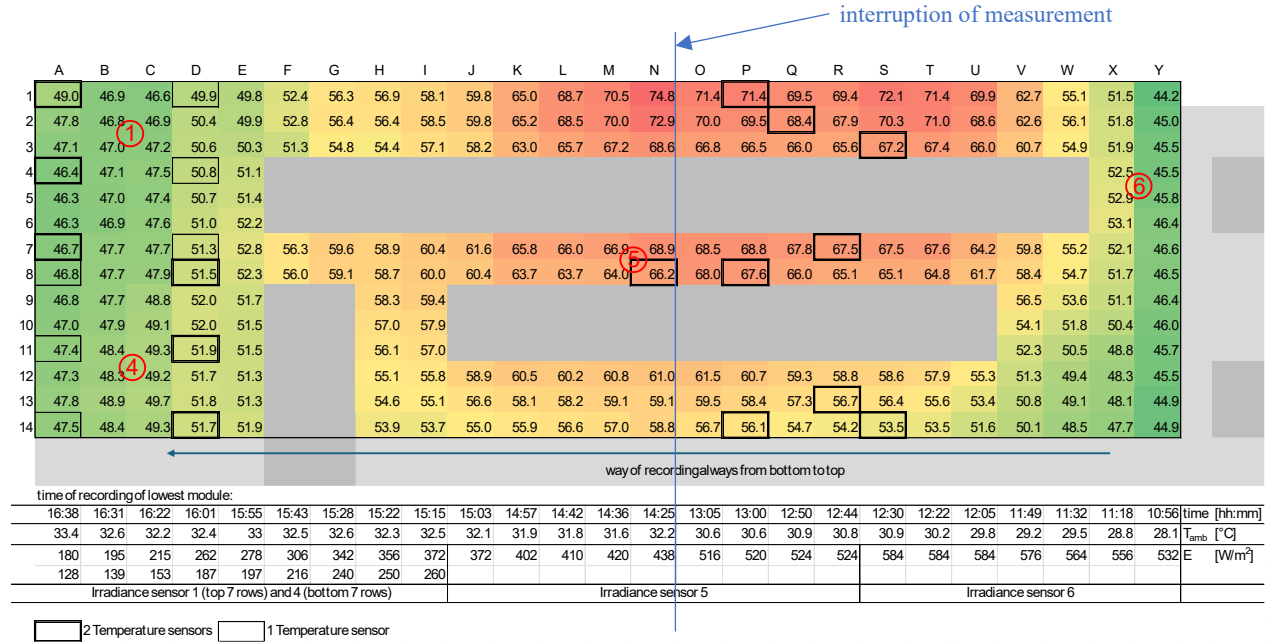


Figure 7-5: Temperature distribution of south-facing facade recorded from the front (90°) at ground level over the course of the day, visualized from hot (red) to cool (green) – the position of temperature sensors on the backside of each module marked by a thin box for one sensor in the middle and a thick double-lined box for one sensor in the middle and one on the edge of the module, the irradiance sensors are marked by red circled numbers.

The temperature recorded by the camera depends on the angle at which the camera is oriented relative to the plane of the facade, since the emissivity of the modules varies with the observation angle. As the angle between the camera the plane of the module decreases, the higher the modules are positioned – i being 1 or close to 1 – the temperature recorded slightly decreases. This does not match the results of another study conducted on the same facade in 2022 implying a change of emissivity dominating the IR measurements [57]. The effect can be seen in the outer module columns in Figure 7-5 and the far-right columns in Figure 7-6. The temperature measured by the IR camera decreases with increasing height of the module position as the angle at which the camera records is reduced. In reality, the air in the ventilation gap heats up and rises – known as the chimney affect [57] – meaning the upper modules are actually warmer than those bellow.

For the data in Figure 7-6, the measurement setup was identical the one in Figure 7-5, except for an offset of the camera position to record the modules at an angle of 45° (see Figure 7-3 b)). In this case, the effect of the camera angle can also be observed horizontally: Due to time constraints during the measurement as of 12:16, two parallel columns were recorded simultaneously whenever possible. As a result, the measuring angle for the left module was slightly less 45°, while the angle for the right module was slightly greater than 45°. Clear examples of this effect can be seen in measurements starting at 14:21 (columns K and L) or 14:59 (columns H and I). For modules at the same height, minor temperature differences of 1 - 2 K are typical, but these can increase to a ΔT of up to 7 K.

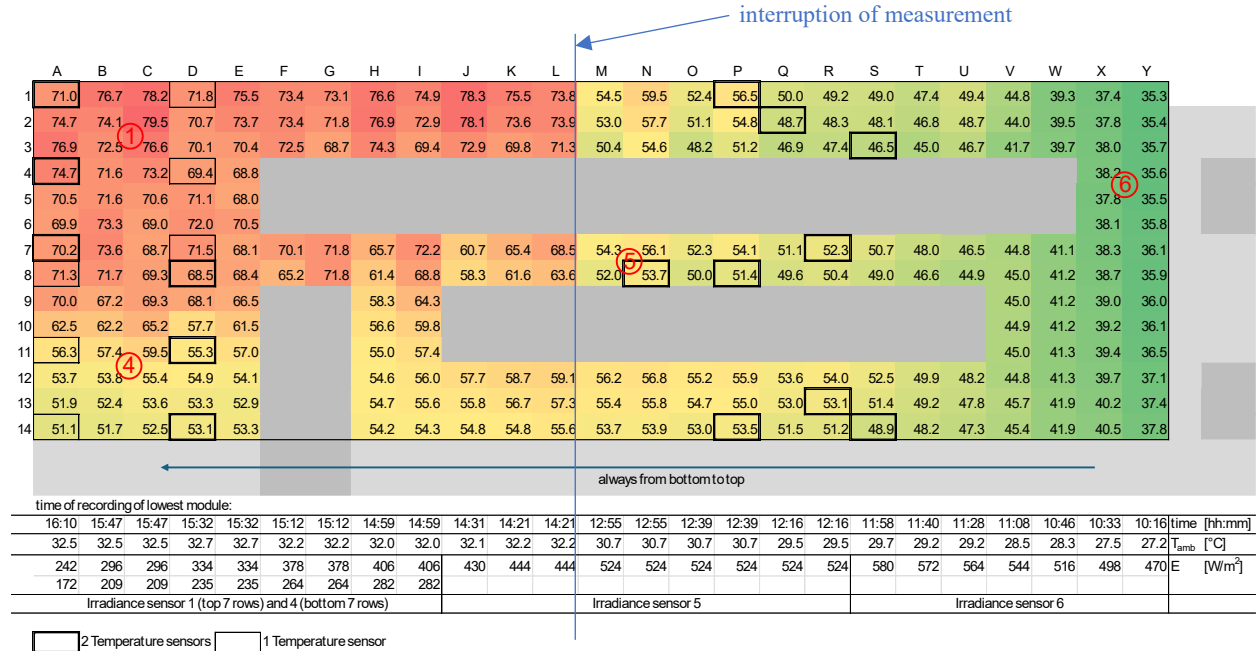


Figure 7-6: Temperature distribution of south-facing facade over the course of the day, visualized from hot (red) to cool (green), recorded at a 45°-angle at ground level – the position of temperature sensors on the backside of each module marked by a thin box for one sensor in the middle and a thick double-lined box for one sensor in the middle and one on the edge of the module, the irradiance sensors are marked by red circled numbers.

The jump in temperature between the left and the right sides of Figure 7-6 is due to a break of just over an hour in the measurement process, as data collection was interrupted at around 13:00 and resumed at 14:21. The extreme temperature differences are a result of the changing position of the sun during this period, which will be discussed in more detail in the following section.

7.1.2.2 Sun Reflection during IR Measurements on the Facade

Contrary to the previously discussed theory, there are some columns in which the temperature of the modules increases with height, even though the angle of the camera alignment decreases. This is the case for the modules in the center to right area in Figure 7-5 and the modules in the center to far-left area in Figure 7-6, and is due to the reflection of the sun on the modules. Even if the pattern is not directly visible in the IR image, it is clearly recognizable in the data. During the noon hours between 13:00 - 14:00 (during summertime – so 12:00 - 13:00 without daylight saving time), the sun reaches its highest position. The sun was at its highest point at 13:13 [109] and in direct line of reflection for a south-facing facade, as shown in Figure 7-5. The same applies to the recordings in Figure 7-6 during the afternoon hours. When the sun moves to the southwest and the camera is oriented toward the northwest and angled upward to record the top modules, the sun reflects directly into the camera. This occurs when the angle of incidence and angle of reflection are equal. The following illustration depicts this interaction for both cases, with the angle of incidence and the angle of reflection both denoted as δ .

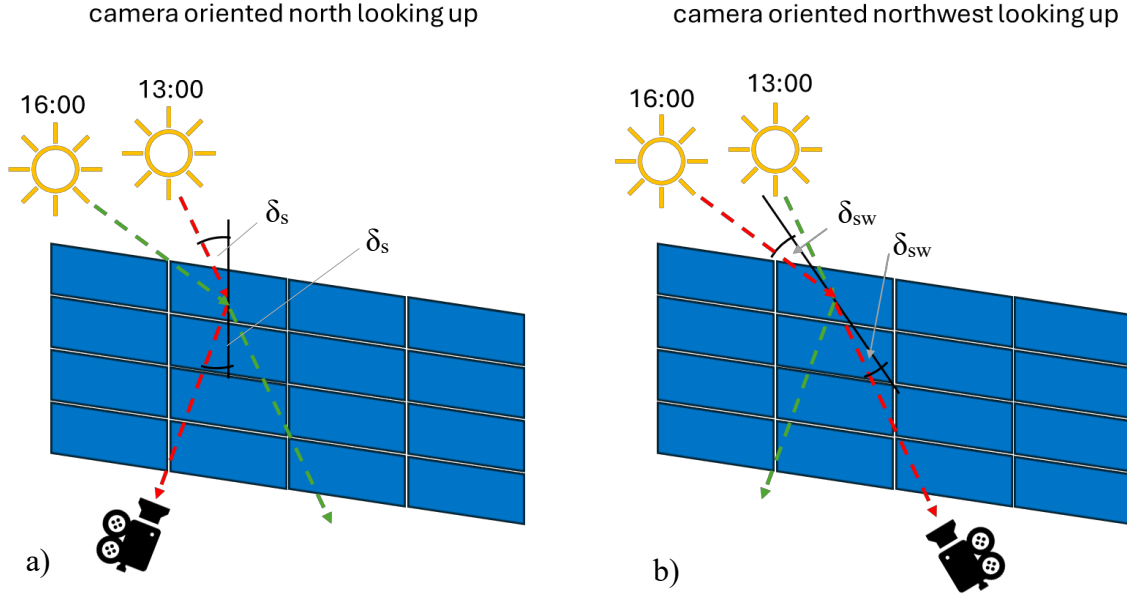


Figure 7-7: Illustration of sun reflection on modules depending on time of day and camera orientation, a) reflection for recordings in Figure 7-5 at around noon with angle of incidence and angle of departure denoted as δ_s for a south positioned sun, b) reflection for recordings in Figure 7-6 in the afternoon with angle of incidence and angle of reflection denoted δ_{sw} for a southwest positioned sun.

The obtained temperatures above of 70°C are not the actual temperature of the modules, but rather a reflection. This is also confirmed when comparing the data to the data of the temperature sensors on the back side of selected modules. The temperature differences between the mean values recorded by the IR camera and those measured by the temperature sensors mounted on the backside of the modules are presented in correlation with the timestamps shown in Figure 7-5 and Figure 7-6. These comparisons differentiate between sensors placed at the center and those positioned at the edge of each module, allowing for a more detailed analysis of spatial temperature variations.

As discussed in Chapter 6.2 the assumed temperature difference between the front and back of a module of 1 K has been considered and implemented to visualize the deviation of the results. The values have been determined as follows:

$$\Delta T_{IR,sensor} = T_{mean,IR} - (T_{sensor} + 1\text{ K}) \quad (7-1)$$

While $\Delta T_{IR,sensor}$ is the temperature deviance displayed in the following figures, $T_{mean,IR}$ is the mean temperature of all pixels recorded by the IR camera for one module as displayed in Figure 7-5 and Figure 7-6, and T_{sensor} is the temperature recorded on the back side of the module where the sensors have an accuracy of 0.5°C .

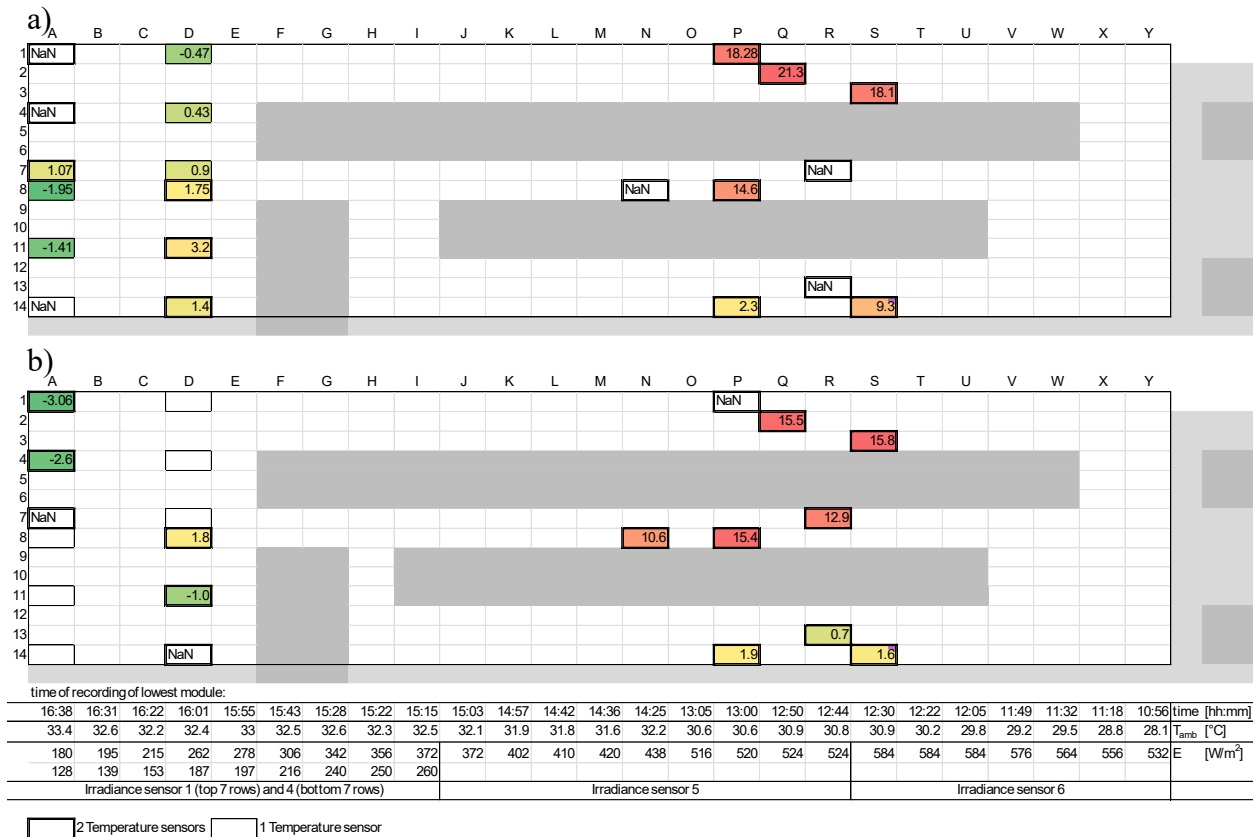


Figure 7-8: Temperature difference (ΔT) of mean temperature measured by IR camera as in Figure 7-5 and measured by temperature sensor on module backsides of selected modules at the same time, a) with the sensor placed in the center of the module, and b) with the sensor placed at the edge of the module.

The data in this figure supports the hypothesis that solar reflection influences the temperatures recorded by the IR camera. This corresponds with the temperature pattern in Figure 7-5, where the highest temperatures at the top center of the south facade coincide with the largest discrepancies between IR-measured temperatures and those measured by the sensor on the backside. This can also be observed for measurements with a 45° offset (as in Figure 7-6) as displayed in Appendix A1.

7.1.3 IR Measurement at String Level

Although temperature distribution across PV modules is primarily influenced by irradiance conditions, mounting orientation and ambient environment, the investigation of thermal gradients along a string due to electrical and environmental factors can be insightful. This can be done, for example, to detect string heating patterns due to inverter-related faults or to isolate localized defects and assess their impact on neighboring modules within the same string. Due to previously discussed effects (sun reflection and angle dependency) the temperature dependencies on string level will be analyzed using the data provided by the temperature sensors placed on the module backsides of selected modules. The positioning of the modules in the facade and the placement of

the sensor (either in the center of the backside or close to the edge) is depicted in Figure 5-2 for the south facade and Figure 5-3 for the north and west facades.

The following data was taken at 13:00 on 01.07.25 with the sun being close to its highest point for the day and a time specific ambient temperature of 30.6°C. For this timestamp the south facade was exposed to direct sunlight while the west and north facades were shaded and predominantly received diffuse light. POA irradiance on the north facade ranged from 133 W/m² at the bottom half of the building to 197 W/m² for the higher modules, on the west facade from 224 W/m² at the bottom half up to 231 W/m² at the top. The south facade logged irradiance values in the range of 195 W/m² at the bottom left up to 318 W/m² at the top left, while the sensors located on the right side of the facade recorded irradiance values between 272 W/m² and 306 W/m². The exact positions of the irradiance sensors can also be seen in Figure 5-2 for the south facade and Figure 5-3 for the north and west facades.

In the following visualizations, the data is organized sequentially from the negative to the positive terminal of each string. Only sensor readings from the center of each module are included, for strings where all three sensors (beginning, middle and end of each string) were fully operational. Some of the data could not be used due to sensors either malfunctioning or failing to establish reliable contact during measurements, often as a result of module de- and reinstallation.

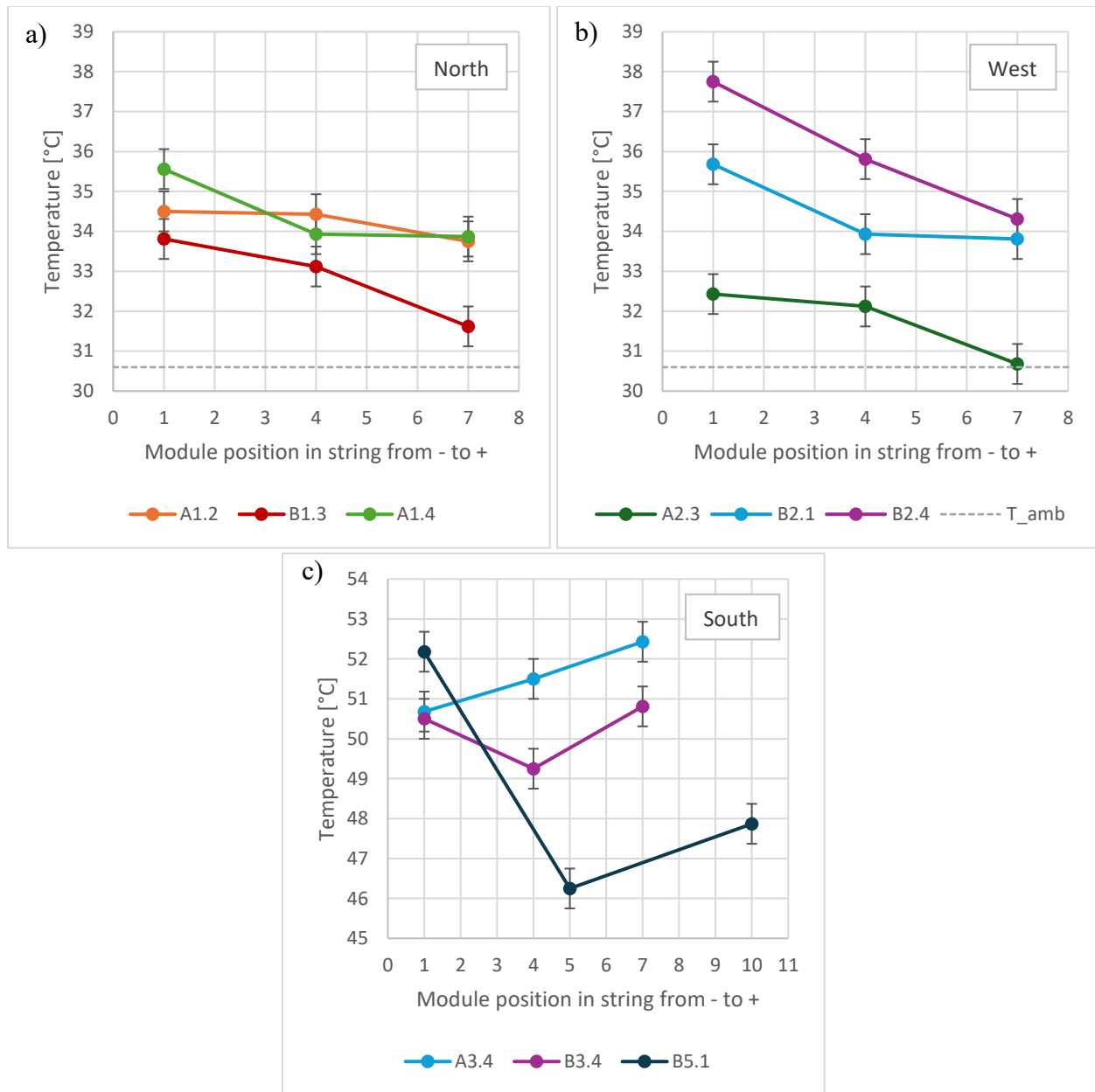


Figure 7-9: Temperature development of strings equipped with temperature sensors with 0.5°C measuring accuracy from negative to positive pole a) for the north facade, b) for the west facade, and c) for the south facade.

The data in Figure 7-9 a) and b) shows a temperature degradation from the negative to the positive pole of each string. Since all strings analyzed in Figure 7-9 a) and b) are oriented vertically – with the negative pole at the top and the positive pole at the bottom – it appears reasonable to assume a correlation between a module’s position within a string and its temperature for facades that are not directly illuminated. However, this does not apply to strings fully exposed to the sunlight at the south facade. Because some modules are installed around windows or doorways, the strings are not always arranged vertically as in the other facades but also run horizontally or follow serpentine

paths. The exact arrangement of the strings can be taken from Figure 5-2 and Figure 5-3 respectively.

Overall, the temperature differences between the modules within a string increase with greater exposure to light. Also, the lower placed modules along the north facade are cooler than the top modules. This pattern cannot be clearly observed in the data from the west or south facades, which is likely due to sunlight reflecting off the facade of the adjacent building affecting the upper modules.

Generally, the phenomenon of a universal correlation between a module's position in a string and its temperature is not widely established in literature – most studies focus on module-level temperature modeling, thermal effects on efficiency or system wide thermal behavior [71], [75], [85], [87]. Though, the absence of a clear trend in south-facing strings, where direct irradiation dominates, strengthens the hypothesis that thermal uniformity is supported primarily under diffuse-light conditions and the temperature drop might hint at electrical or thermal propagation effects.

7.1.4 IR Measurement on Disconnected Strings

To complement the preceding analyses at module, string, and system levels, infrared measurements on disconnected strings provide additional insights into their passive thermal behavior. If a solar cell operates at either short-circuit or open-circuit conditions, it does not generate electrical power. Consequently, all the energy absorbed by the solar cell is converted into heat [79]. Consequently, a module in open-circuit conditions would be hotter than a module under regular operating conditions. To assess the extent to which IR thermography can detect such conditions in a PV facade, two strings – A3.4 and B3.4, both located in column D – were switched to open-circuit. The results of these recordings are presented in the following figures, with the disconnected strings highlighted using a light gray dashed outline.

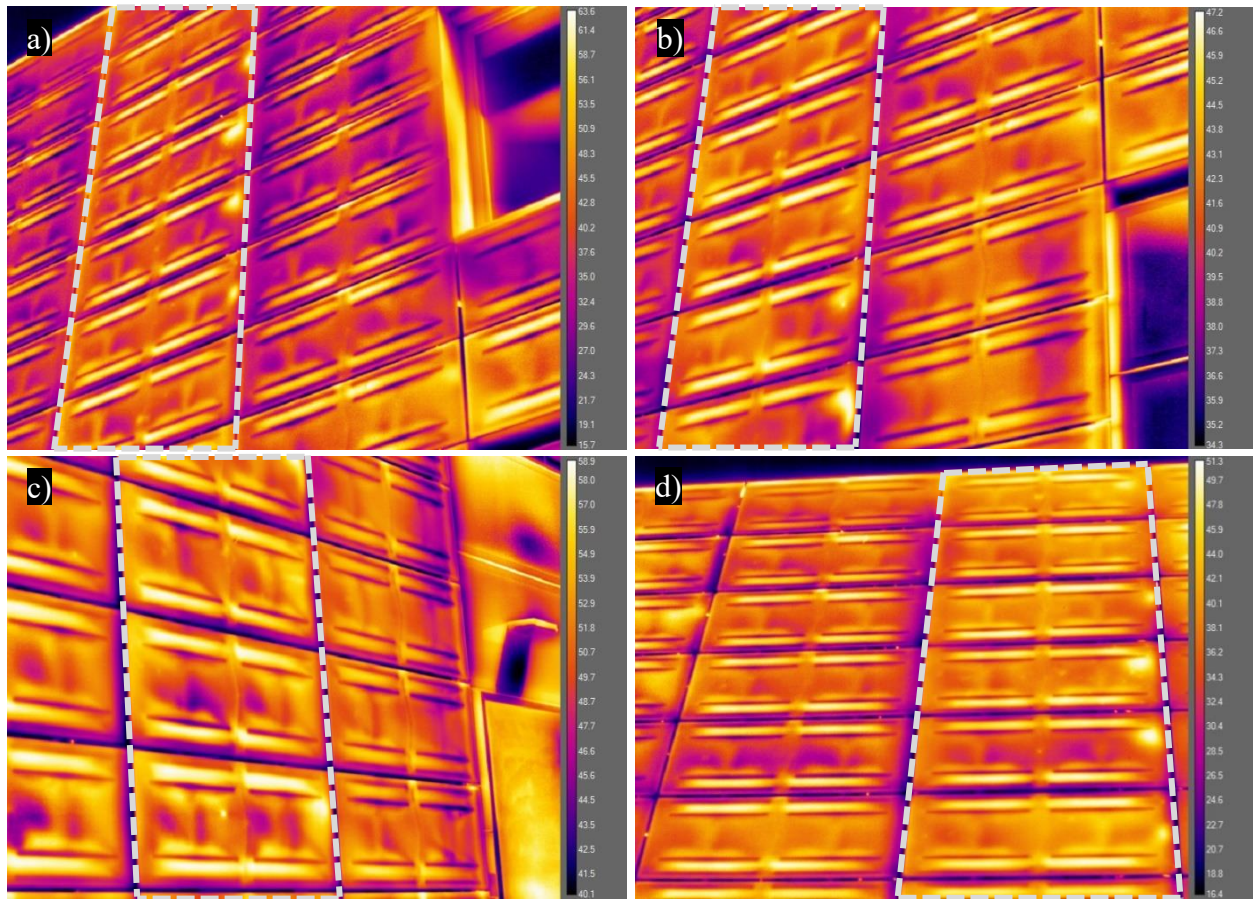


Figure 7-10: IR recordings of open-circuit strings marked by grey dashed border, a) showing modules D2 to D8 from the right, b) showing modules D6 to D10 from the right, c) showing modules D10 to D13 from the left, and d) showing modules D1 to D7 from the front.

The infrared images clearly reveal the expected temperature differential caused by the open-circuit condition of the strings in column D, marked by light grey dashed lines in Figure 7-10. The visibility of this thermal anomaly varies depending on the angle of incidence of solar radiation, with the effect becoming more or less pronounced based on the sun's position. Images a) and b) show the temperature increase more clearly as these recordings are least affected by the sun rising in the southeast at the time of the measurement. However, images c) and d) also show the temperature increase from the front and left sides, each captured from different viewing angles. The ability to observe temperature increases in disconnected modules from multiple positions – including those affected by sunlight reflection – demonstrates that IR thermography is a reliable method for identifying disconnected strings.

The exact times and temperatures recorded are presented in Figure 7-11, shown as the mean temperature across the ROI of each module. The color coding is the consistent with that used in previous chapters, ranging from green for low temperatures to red for high temperatures in this context.

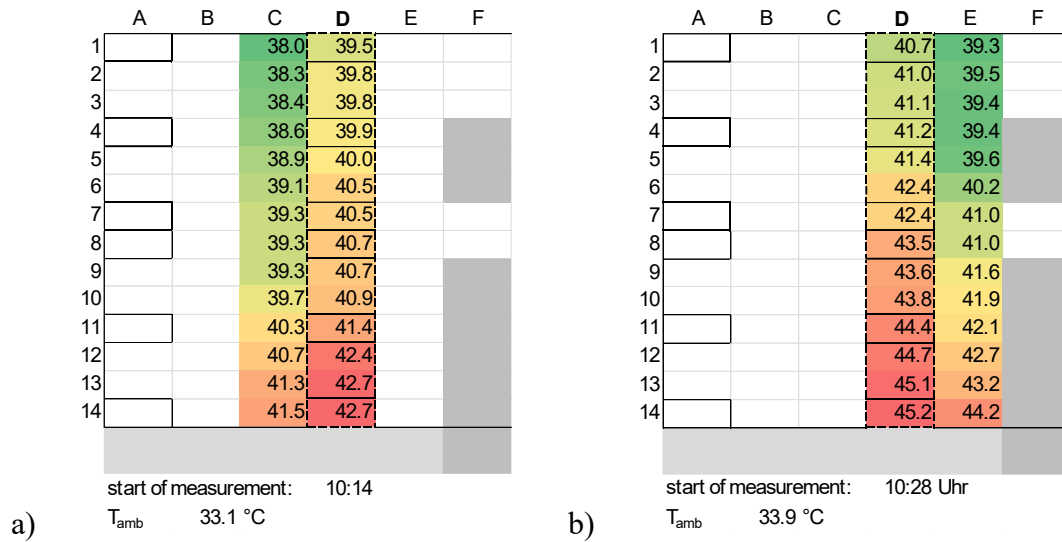


Figure 7-11: Temperature effects of column D being in open-circuit, a) measurement of column C and D at an irradiance of about 460 W/m² for the top half and 306 W/m² for the bottom half of the modules, and b) measurement of column D and E at an irradiance of about 486 W/m² for the top half and 324 W/m² for the bottom half of the modules.

Due to the specific constraints, it is not possible to thermographically capture the entire facade in a single infrared recording, resulting in the following procedure being the same as in Chapter 7.1.2. Only the results of the recordings with an offset of 45° to the right are visualized in the figure above, as these values are least affected by the sun's reflection.

Across all measurements, a consistent mean temperature difference of approx. 1 - 1.5 K was observed between two horizontally adjacent modules, based on their average module surface temperatures – the hotter module always being in open-circuit condition. Consequently, it can be expected that by converting the incident radiation into electrical energy and dissipating it through the flow of current a cooling effect of the same magnitude is achieved. The effect of smaller angles resulting from a higher module position can be seen, the reduced temperature with higher position is clearly visible as well.

7.1.5 Integration of a Damaged Modules

The effect of a broken module could not be measured on the Living Lab building site, as all of the modules on the analyzed facade are intact. However, a recently damaged module was demounted and stored for further research. This module with the last digits of its serial number being 0688 will be called such in the following chapters. It was compared to an intact module – its serial number ending with the digits 0069.

While module 0069 is an unused module that was stored under darkened and dry conditions, module 0688 is a functioning but damaged module with the front glass completely shattered and only held together by the characteristics of the safety glass (see Appendix A1). It was stored in darkened dry conditions after being replaced in the facade.

Measurements in the flasher were initiated with module 0069 that was exposed to approx. 25 flashes before usable data could be retrieved. Following the IR and flashing measurements, electroluminescence (EL) recordings were taken of each of the modules, these will be compared first.

7.1.5.1 Thermography and Electroluminescence of a damaged Module

Since no visible physical damage was observed on the modules currently installed in the investigated facade, a previously removed damaged module was examined separately. Its thermographic behavior was then compared to that of an intact module to gain deeper insight into the thermal characteristics associated with module damage. These IR measurements were taken in the measurement setup of the ZPV roof. To enable conditions similar to those for facade integration, at least in terms of module inclination, the modules were installed at a 90°-angle as described in Chapter 5.2. Yet the ventilation conditions are not comparable to facade integration. These IR imaging results together with RGB images and the EL measurements of both modules are compared to each other in Table 2.

The damage of the front glass is not always visible at first glance and often only becomes visible at close proximity as seen in Appendix A1. However, identifying damage to the front glass at an early stage is crucial. If the cells still work initially, apart from the safety measures not being met, water damage and further microcracks due to less stability are likely to severely affect the modules long-term. Consequently, identifying damaged modules through IR would be an efficient method to determine defect modules in a big system without having to inspect each module individually from up close. When analyzing the following IR images, it is important to note that they do not share the same temperature scale, instead each scale has been adjusted to best visualize the temperature behavior observed in each measurement.

The IR images in Table 2 demonstrate that the dominant features discussed in Chapter 7.1.1 are also evident in a damaged module. Without the insulation on the back of the modules, additional features – such as backrails and temperature sensors – become identifiable. Furthermore, elements like adhesive labels on the rear side appear more pronounced. However, the overall image appears blurrier and patchier due to the reflectance of the shattered glass. Additionally, an uneven hot area can be observed on the lower left side of the module, extending up to the top left corner. This indicates a localized temperature rise and likely damage that prevents the cells in this region from functioning properly. Along the right side of module 0688 a yellow shaded patchy area becomes visible in the IR measurement as marked in the image. When comparing this area to module 0069, a similarly shaded but less patchy region can be identified, suggesting the influence of external factors. However, the extent of the “hotter” area is much more pronounced in module 0688.

Additionally, the top edge of the damaged module appears to be hotter compared to the intact module. This is likely due to the cracked front glass breaking away along the edges (see Appendix A1), which results in intensified diffuse reflection of the sunlight. IR images including the Temperature scale can be taken from Appendix A1 as well.

Table 2: IR and EL imaging of a damaged module 0688 in comparison to an intact module 0069.

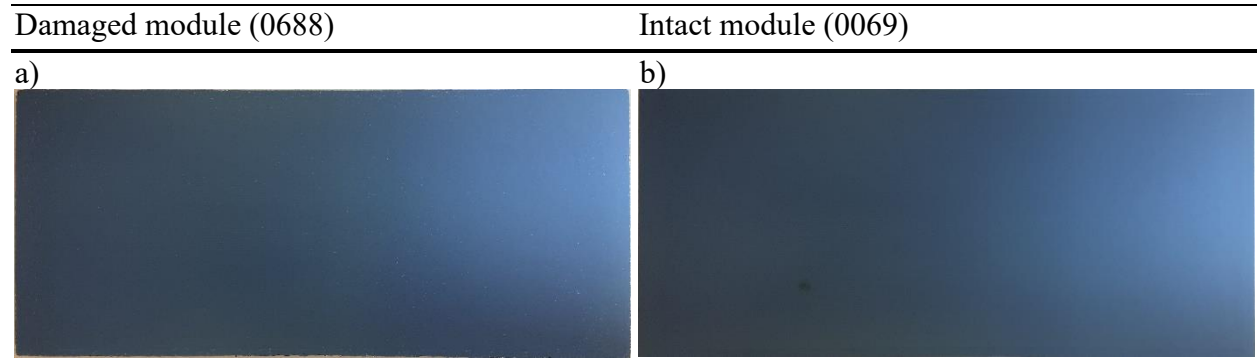


Figure 7-12: Image of a) a damaged module 0688, and b) an intact module 0069 in an indoor environment with incident irradiation coming from the right.

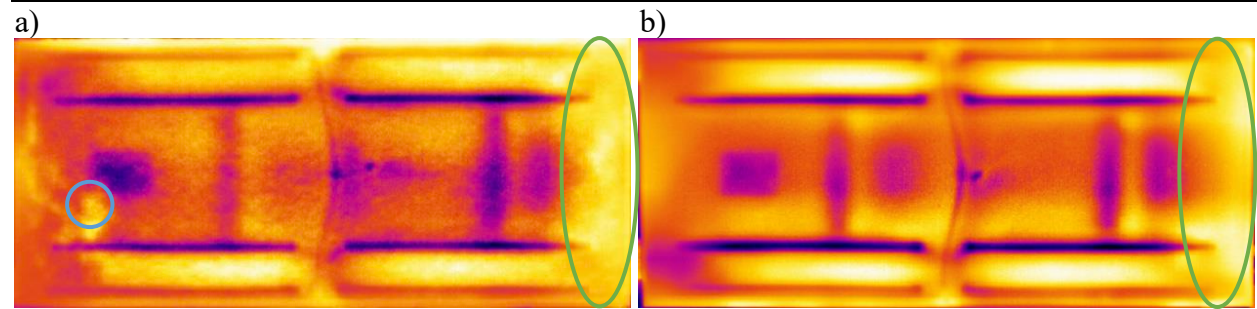


Figure 7-13: a) IR recording of module 0688 on 30.07.25 at 14:04, and b) IR recording of module 0069 on 30.07.25 at 13:50.

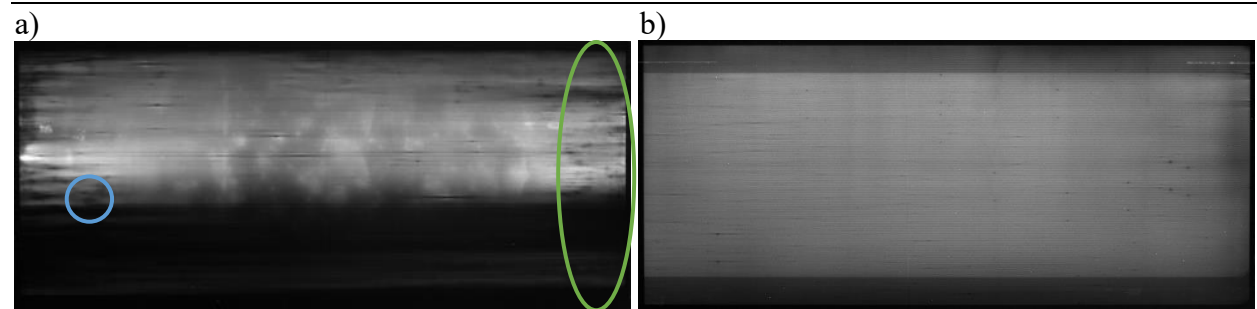


Figure 7-14: a) EL recording of a functioning module but with damaged front glass (module 0688), b) EL recording of an intact module (module 0069).

Electroluminescence (EL) makes radiative recombination visible, which is when an electron recombines with a hole in the semiconductor emitting a photon to release energy. The measurements of an active module area of 135 cells per module, with a cell area of 4 x 1,570 mm, were taken by inducing a 300 mA current which resulted in a 78.5 V operating point for the undamaged module and a 76.9 V operating point for the damaged module. Figure 7-14 b) shows the EL image of a perfectly intact module that has a darker bar on the top (positive connection) as well as on the bottom (negative connection). These edge regions can also contribute to higher effective series resistance (R_s), especially if carrier collection near the contacts is hindered due to recombination losses. Consequently, higher surface recombination at the edges of a module, due to edge related trap formation and caused by Shockley-Read-Hall (SRH) recombination, becomes

visible in the EL images, but is a regular event [110]. Traps – typically crystal defects or impurities, grain boundaries, or surface damage or roughness – cause the energy to not be released in form of a photon but in turn lift another electron to a higher energy level. When an electron falls into a trap, a free hole later fills the same trap, the electron and the hole then recombine without emitting energy in form of light, but in form of heat through lattice vibrations. The impact lowering the overall voltage output and the fill factor (FF). However, this heat cannot be detected in the IR images, as it is likely to be drowned out but other more dominating factors, the heat increase is not enough to be measurable and the edges are more likely cooled by the air flow.

In Figure 7-14 b) dark spots indicating shunts in the right center area of the module can also be seen showing that even though a module is new and unused, it does not come from the manufacturer in an absolute perfect condition. A shunt is an unintended low-resistance path bypassing the p-n junction and thereby reducing the V_{oc} , especially at low irradiance levels (see Figure 7-18, where a saturation of the V_{oc} is observed with increasing irradiation), as well as the fill factor. Thus, these two events are most likely the main reasons why the maximum power calculated in Table 3 is only around 115 W, even though the data sheet specifies a nominal power of at least 130 W.

Compared to the intact module, the damaged module exhibits significantly more shunts, most of which are concentrated in the right central area. The most prominent feature is the entire lower third of the module, which appears as a dark region. This suggests that the entire lower third section of the module consists of nonfunctioning cells, which would typically result in the V_{oc} dropping proportionally by one third, since the cells in a CIGS module are interconnected in series. This expected reduction does not occur in Table 3, where, surprisingly, the V_{oc} of the damaged module barely exceeds that of the intact module. This counterintuitive phenomenon may indicate measurement abnormalities, altered recombination dynamics, or enhanced carrier extraction from the remaining functional cells due to uneven internal electric field distributions. This situation will be discussed more thoroughly in the following chapter when analyzing the electric parameters of the modules with flasher measurements. Furthermore, the staining observed in the remaining area of module 0688, with some spots appearing extremely light, is likely due to the breakage of the glass. In these regions, photons may be absorbed less by the fractured glass.

A study conducting postmortem analysis on a CIGS PV module after potential-induced degradation, observed that the edges of the module were significantly more affected, as revealed by EL measurements. The root cause of degradation in this case is assumed to be ion migration-induced bulk defects and CIGS/ CdS (cadmium sulfide) interface defects. However, this conclusion is based on current-voltage modelling, which predicts significant voltage and current losses that are not expected to occur in the present scenario. Therefore, while this reasoning is not directly applicable here, it remains a noteworthy consideration. [111]

The events seen in the IR images correlate with those in the EL images. The hot area in the lower left corner of the IR measurement for module 0688 does not, by itself, fully explain why the lower

third appears darker in the EL measurement. However, if both images are overlaid, the hotspot aligns with a dark region that extends higher than the lower third area marked in blue in Figure 7-13 a) and Figure 7-14 a). Additionally, the hot area along the right edge of the module corresponds to a cluster of shunts visible in the EL image of module 0688. These are marked in green in Figure 7-13 a) and b), as well as in Figure 7-14 a). This special correlation between thermal anomalies and electroluminescence features suggests localized electrical defects, although further analysis is required to determine the exact nature and impact of these regions.

After analyzing the data in Table 2, it becomes evident that while EL and IR imaging highlight fundamentally different mechanisms – carrier recombination in the case of EL, and thermal dissipation in IRT – there are few direct correlations between the two image types. Nevertheless, one observation is the presence of blotchy areas where cracked glass leads to uncontrolled light reflection.

7.1.5.2 IV-Characteristics of a Damaged Module

To complement the insights gained from IR and EL analyses, this chapter presents quantitative data obtained through IV characterization of both modules. The measurement setup is discussed in further depth in Chapter 5.4. The following measurements provide a deeper understanding of the damaged module's electrical response under varying light conditions and help contextualize the findings discussed previously.

Each module was tested using a flasher under standard irradiance conditions of $1,000 \text{ W/m}^2$ to obtain baseline IV curves. To further investigate module behavior in low-light conditions with reduced irradiance, additional measurements were conducted at 700 W/m^2 , 400 W/m^2 , and 200 W/m^2 . For each irradiance level, both forward and reverse sweep methods were applied. The forward sweep involved gradually increasing the voltage from 0 V to V_{oc} of 91 V being the target voltage, while the reverse sweep measured the module's response under decreasing voltage.

The preconditioning of CIGS modules through light exposure plays a central role in determining cell and module performance [112]. Prior to acquiring the data discussed below, module 0069 was exposed to approx. 25 flashes. As the flasher was initially not calibrated for CIGS modules, primary measurements resulted in current limitation (reverse) and saturation errors (forward) until the flasher was then calibrated properly. The additional light exposure should be taken into account during evaluation. However, its primary influence lies in altering the light-induced metastability of the CIGS absorber layer [112]. While this effect is documented, it could not be sufficiently verified with the available data in this study. The effects on metastability are discussed further in Chapter 7.2.1.

Figure 7-15 shows the IV curves of both a damaged and an intact module at multiple irradiance levels. When comparing the following IV curves of both modules at multiple irradiance levels, a proportional drop I_{sc} can be observed in both the damaged and intact modules. This behavior is consistent with the expected linear relationship between irradiance and photocurrent generation, and indicates that both modules are functioning as expected.

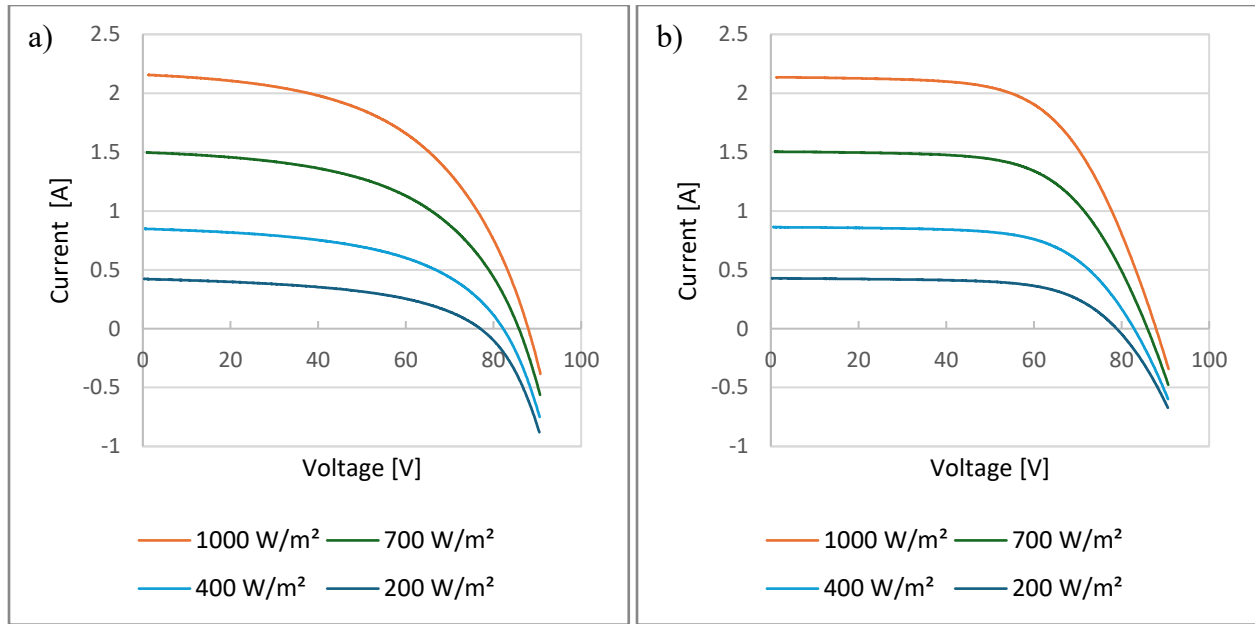


Figure 7-15: a) IV curves of forward measuring method of module 0688 (damaged module) at varying irradiances, b) IV curves of forward measuring method of module 0069 (intact module) at varying irradiances.

At second glance the comparison in Figure 7-15 shows that the curves of the damaged module are clearly flattened, which suggests the presence of shunt and series resistive effects. This thesis is initially supported by numerical evidence, as shown in Table 3, through a comparison of the FF and additional electrical parameters of both modules. Additionally, a slightly higher V_{oc} at an irradiance of $1,000 \text{ W/m}^2$ is noticeable. However, this observation must be interpreted with caution, as the two modules originate from different manufacturing batches – while the damaged module 0688 has a listed V_{oc} of 89.9°V the intact module 0069 only has a listed V_{oc} of 89.3 V . Modul specific data can be found in Appendix A2 for both module batches.

Table 3: Comparison of electrical performance data of measured modules 0069 and 0688 at $1,000 \text{ W/m}^2$.

Damaged module (0688)			Intact module (0069)		
P_{\max}	99.56	[W]	P_{\max}	114.99	[W]
V_{oc}	87.92	[V]	V_{oc}	87.87	[V]
I_{sc}	2.16	[A]	I_{sc}	2.14	[A]
V_{mpp}	60.68	[V]	V_{mpp}	62.09	[V]
I_{mpp}	1.64	[A]	I_{mpp}	1.85	[A]
FF	0.53	[-]	FF	0.61	[-]

A reduction in FF of approx. 16.4% at $1,000 \text{ W/m}^2$, attributed to damage to the front glass, appears plausible and is visually represented by the dashed lines in Figure 7-16. This figure displays the IV curves of both modules at $1,000 \text{ W/m}^2$ alongside their respective curves at 200 W/m^2 highlighting the performance disparity under varying irradiance conditions. A similar reduction in FF is also evident under low-light conditions, further supporting the impact of front glass damage on module performance. The blue curves represent the more realistic average operating point of

modules when integrated into a facade. Additionally, the curves would likely have a slightly higher I_{sc} and a lower V_{oc} at higher operating temperatures [113].

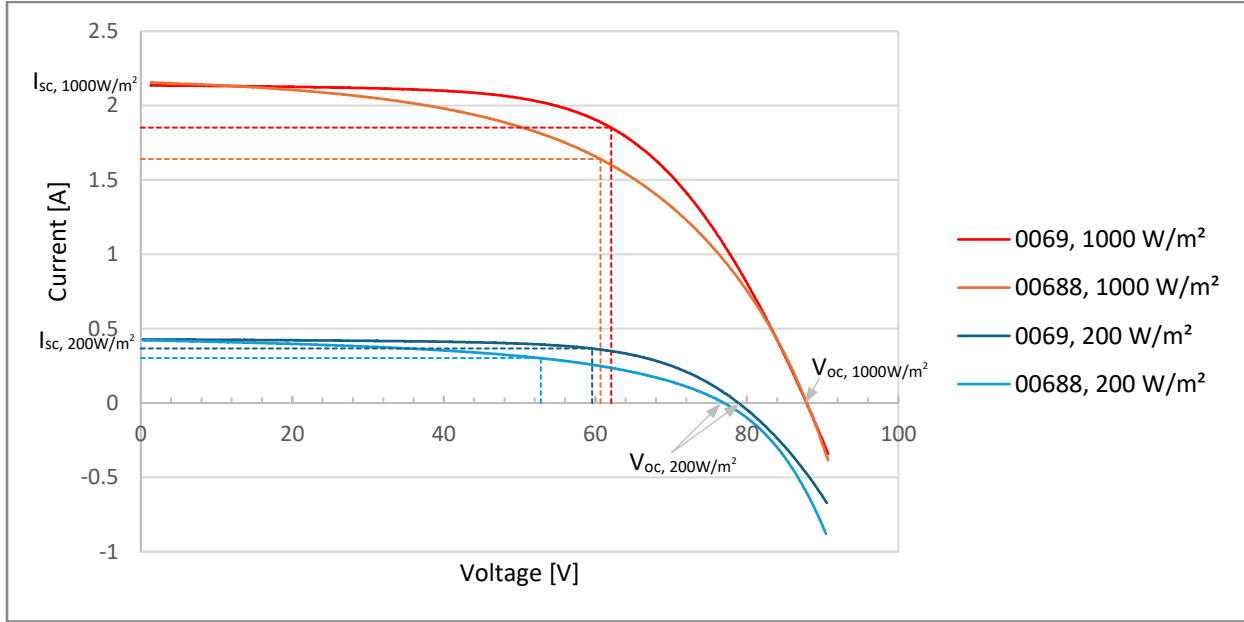


Figure 7-16: IV curves of both modules at irradiances of 1,000 W/m² and 200 W/m².

The lower FF in the damaged module, as illustrated by the areas marked with dashed lines in Figure 7-16 and detailed in Table 3, suggests the presence of internal losses. To better assess the impact of the damaged front glass, both the FF and the V_{oc} were plotted over irradiance, as shown Figure 7-17 and Figure 7-18.

Figure 7-17 demonstrates that the FF decreases with lower irradiance in the damaged module, whereas this trend is not observed in the intact module. This likely indicates an increase in series resistance R_s at lower irradiance levels, possibly caused by microcracks or contact degradation. Since series resistance is influenced by carrier effects such damage becomes more pronounced under reduced irradiance. The damaged front glass might also lead to uneven light distribution, which might cause local hotspots and further FF deterioration.

At high irradiance levels, the difference in FF between the damaged and intact module (approx. 0.8 at 1,000 W/m²) highlights the extent of the series resistance (R_s) in the damaged module. The increased difference in FF between the two modules at lower irradiances (approx. 0.16 at 200 W/m²) suggests a significant impact of shunt resistance (R_{sh}), as R_{sh} becomes more pronounced at lower irradiance levels. The elevated R_s may also explain the darker cells observed in the EL image of the damaged module. In contrast, the nearly unchanged V_{oc} suggests that the V_{oc} is predominantly influenced by the R_{sh} , which appears to be less affected in this case [114].

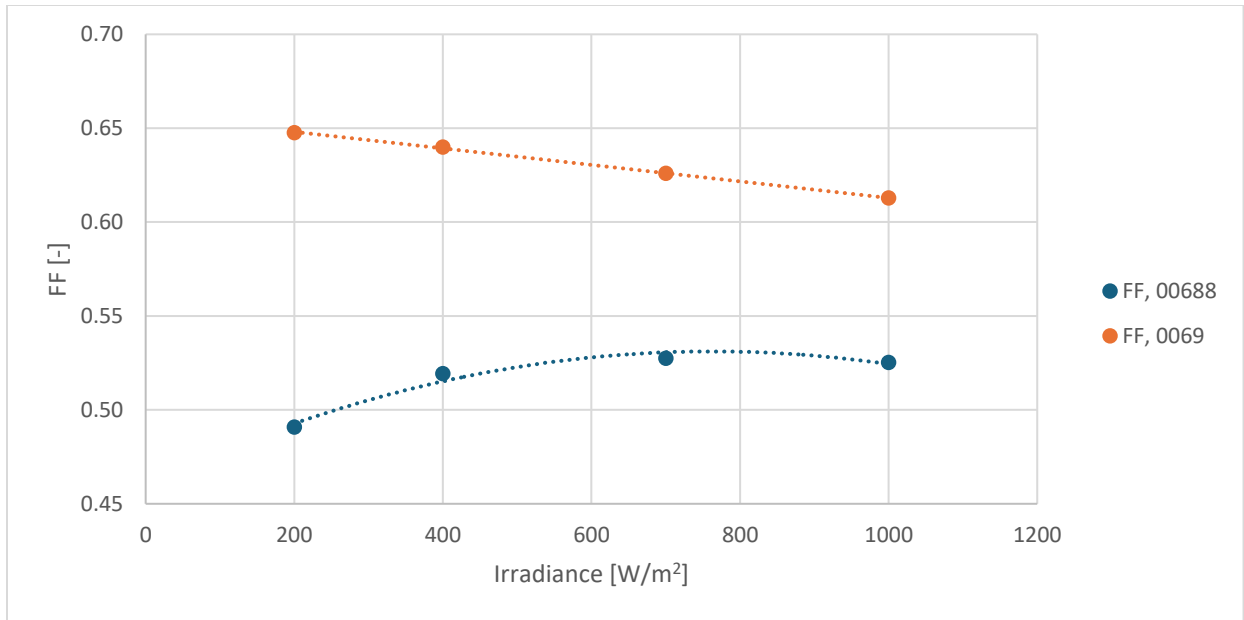


Figure 7-17: Development of fill factors across irradiance for module 0069 and module 0688.

The increased influence of R_{sh} at low irradiance levels is also evident in Figure 7-18, where the V_{oc} is plotted against irradiance. For the damaged module, V_{oc} drops more significantly at lower irradiances, indicating that the effect of R_{sh} becomes more pronounced compared to higher irradiances [114]. The difference is small but clearly visible at 200 W/m².

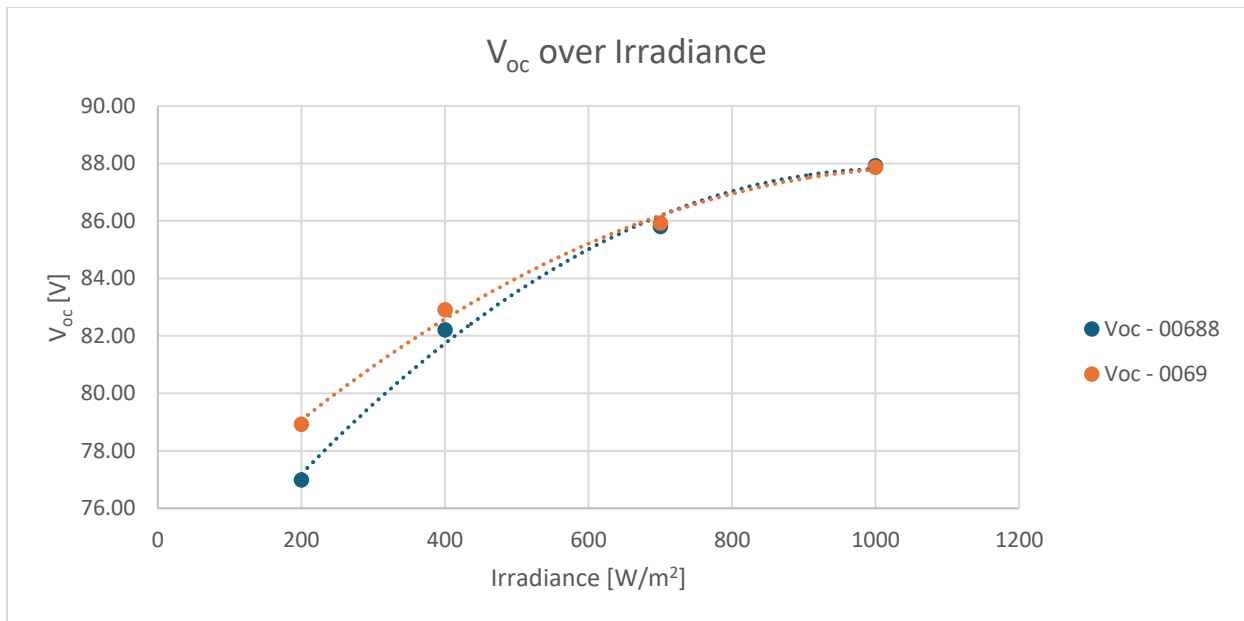


Figure 7-18: Development of V_{oc} across irradiance of module 0069 and module 0688.

These results suggest that the cells appearing darker in the EL image of the damaged module likely have intact interconnections but are limited in current output, provided there are no significant

shunts presents. These features are visible in the EL image in Figure 7-14 a), however, this interpretation is only partially supported, as the I_{sc} is not reduced in the damaged module.

Both series and shunt resistance serve as key indicators for identifying factors that influence the electrical behavior of PV modules. Their impact can be estimated from the previous diagrams in Figure 7-17 and Figure 7-18. Both resistances were quantified by calculating the inverse slope of the IV curves at irradiance levels of 1,000 W/m² and 200 W/m², using equations (7-2) [114]. For this analysis, 40 data points closest to I_{sc} and V_{oc} were used from a total of 1,700 data points. The resulting resistance values for both modules at the two irradiance levels are summarized in Table 4 below:

Table 4: R_s and R_{sh} values calculated from IV curve slopes.

Module	Irradiation	a) $R_s = \frac{dV}{dI}$ near V_{oc} ,	b) $R_{sh} = \frac{dV}{dI}$ near I_{sc}	(7-2)
0069	1000 W/m ²	8.8 Ω	2500.0 Ω	
0688	1000 W/m ²	8.5 Ω	555.6 Ω	
0069	200 W/m ²	25.4 Ω	3333.3 Ω	
0688	200 W/m ²	35.5 Ω	714.3 Ω	

The decline of the R_s from the intact module compared to the damaged module is minimal, but surprising, suggesting the series path is still physically connected and only the front glass is physically damaged. This changes at low irradiance levels, where the R_s of the damaged module increases by about 40% compared to the intact module during low-light measurements. The decrease in R_{sh} between both modules to nearly one-fifth at both irradiance levels is severe and is likely caused by local shunting due to cracks or water ingress prior to demounting the module from the facade after it was damaged. That can also be observed in the EL measurement in Figure 7-14 a). The low R_{sh} can also result in hotspot formation where leakage paths are enhanced and the current bypasses the cell structure [115].

These measurements demonstrate that, under the appropriate conditions previously discussed – such as clear skies, low wind velocity, or optimal measuring angles – damaged yet still functioning CIGS modules can be distinguished from intact modules using IR thermography. Although the IR measurements were not conducted in a facade-integrated setup, the technique proved effective in identifying physical damage – particularly shattered front glass – that may not be visually apparent from mid-range viewing distances. Since such damage impacts parasitic resistances and leads to measurable performance losses, electronic characterization provides additional support for damage detection. However, the extent of degradation can vary, making a combined approach with thermographic imaging together with electrical parameter analysis, a suitable method. Although damaged modules may retain partial functionality, they pose safety risks and must be detected and removed to meet applicable safety requirements.

7.1.6 Localized IR Anomalies across the Facade

When measuring the facade of the Living Lab a few abnormalities could be made out, which will be discussed. Throughout this Chapter modules are referred to using the letter-number nomenclature established in Chapter 5.1.1. All occurrences discussed have been recorded at different angles and/ or slightly varying weather conditions to avoid misleading reflections being interpreted as hotspots. Some misleading effects can be seen repeatedly and are discussed in more depth in Chapter 7.3, including the temperature sensor positions or lens damage.

7.1.6.1 North Facade Module B12

Starting with the north facade the hotspot circled in Figure 7-19 can be determined from multiple angles on module B12. While the north facade was shaded, the overall temperature of the modules is relatively low compared to a module exposed to direct sunlight. A hotspot, marked by a green circle in each image, appears in the center of the module. It closely resembles the contact points of the temperature sensors but exhibits a higher temperature difference. Both of the following images were recorded on the same day (20.06.25) in the afternoon, but from different viewing angles.

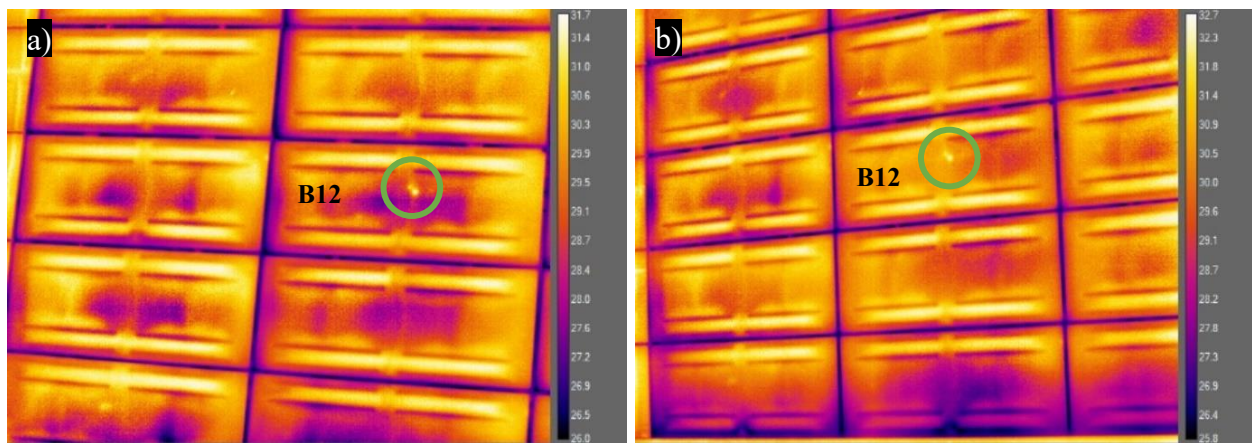


Figure 7-19: North facade with hotspot in module B12 circled green, measured on 20.06.25 a) at 16:41 and b) 16:21.

Due to its similarity to the sensor contacts, this feature suggests a related contact point. However, it is unlikely to be a cable, as cables – while also identifiable – typically appear darker and cooler in the image, rather than being visible as hotspots. If the source is not internal to the module, it is possible that a component responsible for holding the insulation in place has loosened and is now leaning against the module's backside. However, a definitive cause can only be determined by dismantling the module.

7.1.6.2 West Facade C10

The occurrence shown in Figure 7-20 was recorded on 20.05.25, 02.06.25, and 20.06.25, two of these recordings displayed below. Although the hotspot is small, it exhibits a temperature increase of 3 - 5 K in module C10.

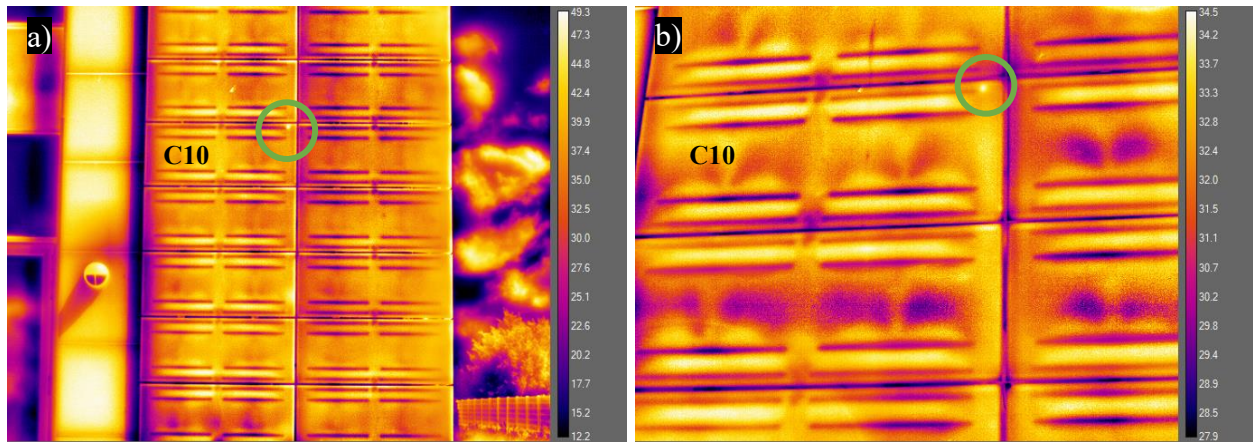


Figure 7-20: West facade module C10 with hotspot on top right corner measured a) on 20.05.25 at 14:01, and b) on 02.06.25 at 12:27.

The exact cause of this hotspot remains unclear. According to the manufacturer, it could be due to excess adhesive from the backrail accumulating at the rail's edge as a result of a manufacturing defect. However, this seems unlikely as the connectors were attached to the back of the modules upon delivery, the adhesive was not removed, and it can still be found on the module's backside. Nonetheless, these adhesive residues cannot be seen in the IR images.

7.1.6.3 West Facade D1

Module D1 in the west facade has a crescent shaped cooler area close to the corner of the facade. This event was observed on at least three separate occasions – 20.05.25, 02.06.25, and 20.06.25 – and is most clearly visible on the last day, with correct calibration as seen in the following images. In Figure 7-21 b), the scale was manually adjusted to mask temperatures below 38°C, resulting in those areas appearing blacked out.

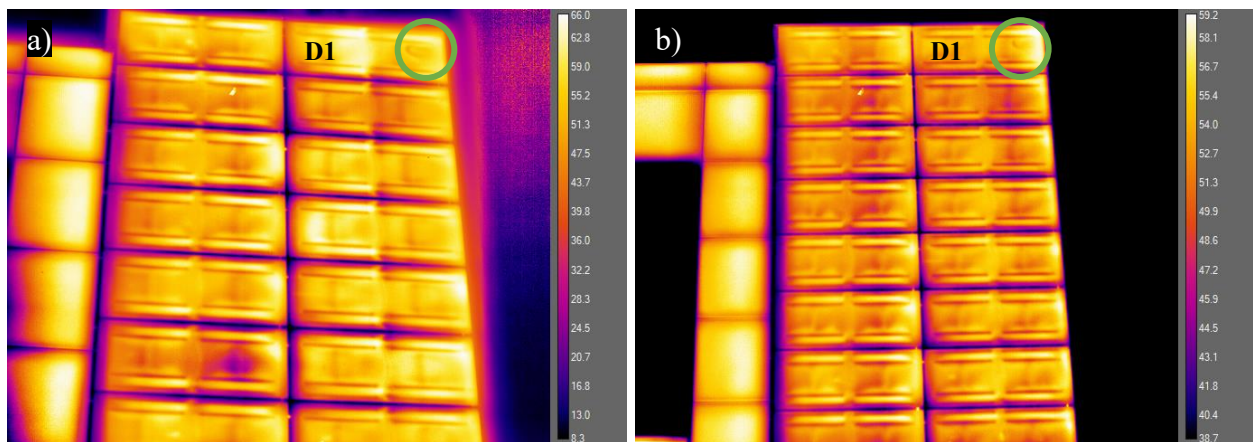


Figure 7-21: West facade crescent shaped cool area on module D1 measured on 20.06.25 a) at 15:50, and b) at 15:29.

The most likely explanation for this occurrence, again, is that the insulation was not properly fastened and has fallen. The setup of the facade is discussed in Chapters 5.1.1 and 5.1.3. The location at the corner of the facade makes this assumption plausible. Since the observed

temperature difference is not greater than those caused by the backrails, for example, no harmful consequences are expected.

7.1.6.4 South Facade A7, A8, A9

As the south facade has the most modules installed, a large range of reoccurring incidents was recorded over the course of the measurement period. Nevertheless, the following occurrence is the most noticeable, as it spreads over the larger module areas. Modules A7 and A9 both exhibit hot areas on the left side of the module, located between the backrails. In contrast, module A8 displays a cold, patchy area in the center of the module. It is important to note that module A7 has temperature sensors in the center and at the edge of the module, each marked by a green arrow. Module A8 also has a sensor mounted in the center of the module. All three of them are visible through small hotspots. It is noteworthy that, while the temperature sensors in the facade measurements presented in this chapter appear visibly hotter, the temperature sensors mounted on the test facades in the outdoor performance laboratory – discussed in Chapter 7.1.5 to compare a damaged and an intact module – appear as cooler spots. The reason for this difference is unclear, but it may be attributable to the fact that the sensors applied to the modules in the outdoor performance laboratory were connected only shortly before the IR measurements, whereas the sensors on the facade are long-term installations.

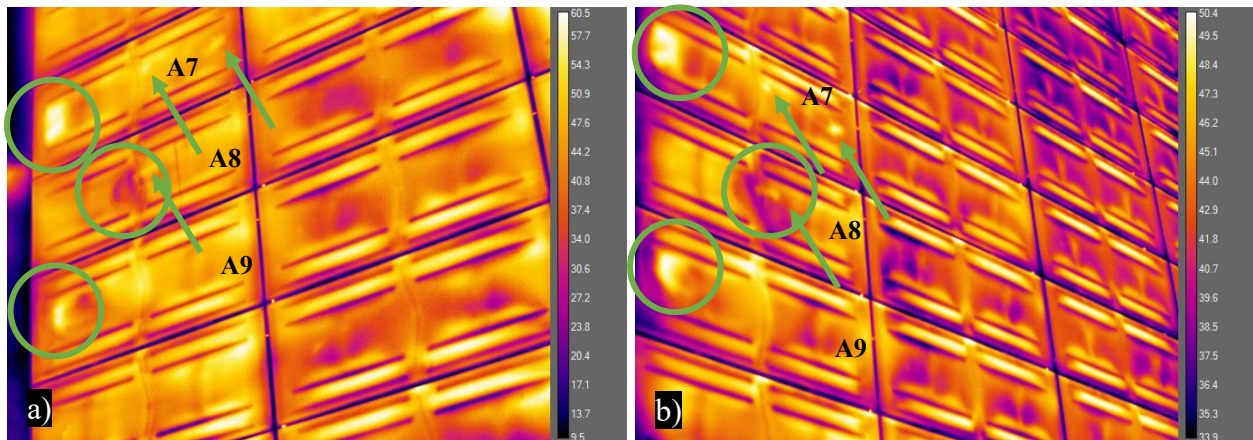


Figure 7-22: South facade with a hot and cold spot pattern along modules A7, A8 and A9, a) on 20.05.25 at 13:30, and b) 20.06.25 at 14:02.

This thermal pattern was observed consistently across multiple days and from various measurement distances and angles but is most clearly visible in Figure 7-22. This consistency confirms a long-term anomaly. The module group is not part of one singular string, but the string connection runs through the center of the pattern. While Module A7 belongs to string A3.1, modules A8 and A9 are part of string B31. In this context, insulation appears to play a significant role and cannot be excluded as a contributing factor. Particularly given that the air gap behind columns A and B is only 5 cm wide, instead of 15 cm as in the rest of the facade [57]. However, these findings did not appear to affect the performance of the strings.

Given the limited means to confirm or refute these interpretations, the hypothesis discussed above remains unsubstantiated. Further investigation may be warranted if the potential for severe damage is anticipated. If the identified temperature difference is clearly lower than the temperature differences caused by the backrail contacts, acute damage is not to be expected.

The preceding chapter examined the most significant anomalies identified during the measurements. While additional irregularities, such as hotspots, were observed throughout the IRT process, they were not discussed in detail, as the remaining cases exhibited recurring characteristics.

7.2 The Significance of IR Measurement Results to BIPV Facades

The results discussed highlight that when conducting IR measurements on PV facades or any vertically oriented modules, multiple factors must be considered to eliminate potential reflections originating from the surroundings of the camera itself. These include varying the camera angle, considering the time of day, and the position of the sun, as well as the weather conditions. To ensure the most accurate interpretation of IR measurements, additional factors such as dirt, staining, and the mounting structure on the rear side of the modules should also be taken into account.

As a general rule, orienting the camera east during morning hours or west during afternoon and east hours should be avoided when conducting IR measurements in Central European regions. For vertically oriented modules, this also applies to northeastern and southeastern orientations in the morning, as well as northwestern and southwestern orientations in the evening, due to the increased risk of reflective interference. Furthermore, a north-facing or south-facing orientation of the camera should be avoided during the noon hours. These guidelines are especially important when the measurement site requires recordings to be taken from below at a shallow angle δ_i as illustrated in Figure 7-4, since such configurations are particularly susceptible to reflective effects.

7.2.1 On Module Level

Localized temperature differences of up to approx. 10 K within a PV module, as measured in this study, can lead to localized power losses. These losses reduce the overall power output and contribute to electrical mismatch between individual cells. The backrails, which significantly influence temperature distribution, run horizontally and parallel to the cell layout. This alignment intensifies the electrical mismatch between cells by reinforcing localized thermal variations. Given the temperature coefficient of -0.39%/K for the CIGS modules used in this study, a temperature increase of 10 K would result in an efficiency loss of approx. 3.9% for the hottest cells compared to the coolest cells within the same module [89], [90]. Since all cells in a CIGS module are connected in series this is particularly important: localizes efficiency losses due to temperature differences impair the performance of the entire module, not just the affected cells.

Temperature variations within the operational range of PV modules can influence the thermally induced metastability of the CIGS material (as opposed to light exposure-induced) and subtly degrade overall module performance. It has been observed that under short-circuit light soaking, both V_{oc} and FF decline more rapidly at elevated module temperatures. This temperature-assisted light-induced degradation (LID) is associated with enhanced trap-assisted recombination and a reduction in the ideality factor under bias [112]. Additionally, a more rapid rate of defect detection was observed when CIGS samples were subjected to light soaking during periods of rising temperature [113]. However, thermal annealing intensifies at elevated temperatures, leading to a continuous reduction in deep trap energy [113], [116]. The metastability of the PV cell material serves as a useful tool to manipulate electronic defect density, thereby enabling the assessment of its impact on the device performance. This also facilitates the stabilization of device parameters, including chemical composition [113], [116], [117].

Morphological changes such as grain growth, pore closure or vacancy diffusion are typically expected at temperatures well over operating temperatures. Such temperatures are not reached in this specific setup and remain negligible below 200°C – above which structural changes affecting optical properties like absorbance and transmittance have been observed [118]. Elevated heat-treatment temperatures typically begin around 300°C with post-deposition annealing processes often utilizing temperature ranges between 400°C and 600°C. [119], [120], [121]

Furthermore, due to the uneven heat load caused by the back rails, the morphological state of the CIGS material may remain unchanged, however, the degradation process is likely to be accelerated compared to conventionally roof-mounted modules [122]. In long-term research, it would be valuable to investigate whether the heating and cooling effects caused by the backrails lead to varying degradation rates across the cells, potentially preventing most cells from maintaining their original performance levels. The thermal influence of the backrails – through both cooling at contact points and heating due to stagnant air and lack of convection within their slots – is a dominant factor, which is consistently visible in all IRT images, even under suboptimal conditions. Module manufacturers have explored ways to mitigate the heating effect by promoting airflow to enhance convection. However, this approach did not yield noticeable improvements [108]. A potential future research approach could involve increasing the enclosed space closed within the backrails to promote improved convection conditions, mitigating localized heating effects.

7.2.2 On System level

At the system level, infrared measurements offer valuable insights into the thermal dynamics of BIPV facades, particularly with regard to long-term performance and degradation risks. It is important to note that the elevated temperatures act as a key driver of accelerated degradation, significantly influencing the rate and severity of material and performance deterioration. Although south-facing modules generally receive the highest irradiation during summer months, the vertical orientation of facade-integrated systems shifts peak irradiation to the winter months. This results in higher energy yields, but not necessarily higher temperatures as the ambient temperature is much lower during these months. [92], [123], [124]

Although the vertical alignment of facade systems reduces direct solar irradiance during peak sun hours by roughly 30 - 40% compared to optimally tilted modules [125], field measurements from the University of Applied Sciences of Southern Switzerland (SUPSI) reveal that, particularly on clear winter days, the average temperature of ventilated facade modules can be more than 20 K higher than that of a roof added module [92]. High temperatures together with high humidity, which is secondary in this specific case, are the main degradation accelerators [126], [127]. While a larger ventilation gap might not may not significantly affect the module's short-term performance [57], long-term degradation is likely to be accelerated by smaller air gaps due to increased stress and reduced cooling efficiency [128]. Faster degradation of facade modules, depending on their orientation, can enhance electrical mismatch across the system. However, in this specific case, these are trivial, as each facade orientation is assigned to at least one dedicated inverter.

IRT allows many modules to be thermally assessed at once, which is particularly convenient for large systems. To enhance convection, ventilation strategies can be developed based on thermographic images, or facade geometries can be adjusted accordingly. Conduction heat dissipation, on the other hand, is often neglected in thermal models (see Chapter 4.1.2), as its contribution is generally considered negligible. However, it appears to be high enough to dominate thermographic images. The images show that the mounting design choice clearly has an impact on thermal patterns of a PV module. Consequently, thermography enables manufacturers to research and optimize extreme temperature differences within a PV module or system.

7.3 Measurement Uncertainties Resulting from Measurements

Especially in outdoor thermography, the list of sources for potential error is extensive due to the numerous external factors that cannot be controlled. Nevertheless, these sources can and should be minimized to prevent misleading results. In the following chapter, the main sources of uncertainty are discussed in order to form future guidelines for reliable and reproducible IR measurements.

7.3.1 Evaluation of Temperature Data at Pixel Scale

For a representative evaluation of pixel data, the data for module P13 is listed below. The data in Figure 7-5 and Figure 7-6 represents the arithmetic mean of pixel temperatures in an IR image for the region of interest (ROI) defined as the area of a single module. Due to factors such as sensor noise, angle of view, and emissivity variations, each pixel is associated with a certain measurement uncertainty. Thus, the ROIs examined had standard deviations (std. dev.) of up to 3.9 K. The std. dev. helps quantify thermal uniformity of each module and in a more general context a std. dev. this high might indicate defects or hotspots worth investigating. As discussed in previous chapters, the large standard deviation and the high variability or noise in the data visualized in Figure 7-23 are primarily caused by the dominant effect of the backrails on the modules.

Figure 7-23 a) illustrates the temperature distribution across individual pixels within a defined ROI of one module (module P13). Pixel counts were gathered within 0.5 K intervals over a temperature range from 50°C to 64°C. The resulting histogram reveals a broad spread of values, with a pronounced peak occurring between 58°C and 59°C. This peak aligns closely with the calculated mean temperature of 58.41°C, depicted in Figure 7-23 b). Figure 7-23 b) presents a box plot that illustrates the temperature distribution of all pixels within the same ROI. While a substantial portion of the pixel values clusters around the median (which is close to the mean value), the plot reveals considerable spread, particularly toward lower temperatures. Notably, the difference between the mean temperature and the minimum recorded pixel value within the ROI approaches 20°K, indicating significant thermal variation across the module surface.

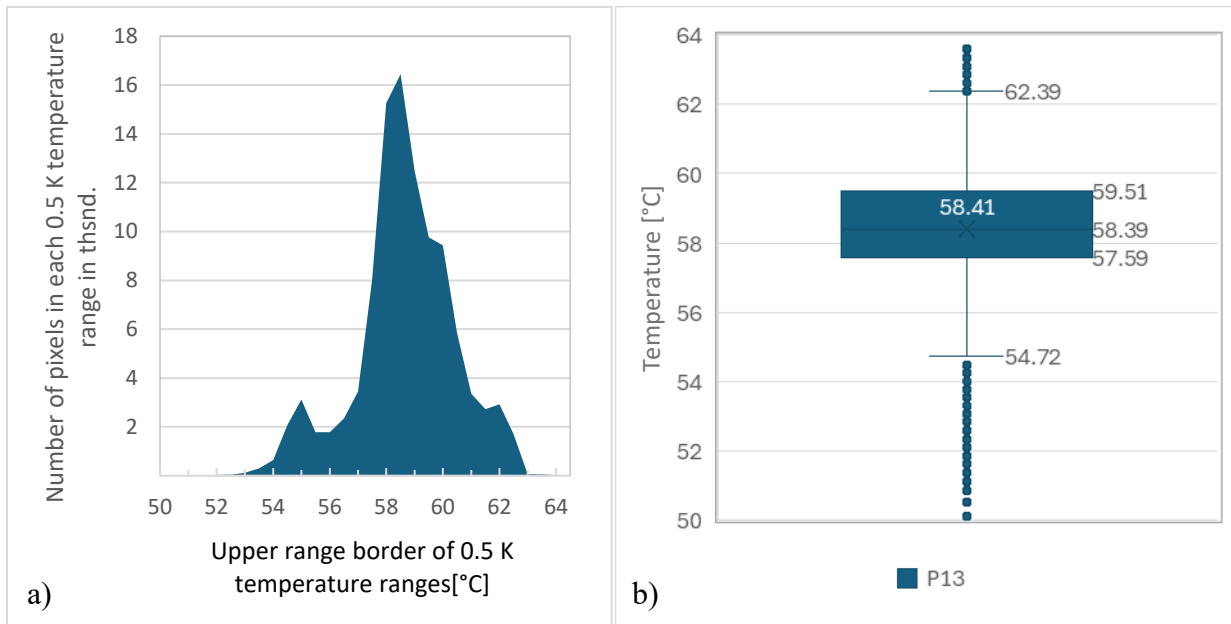


Figure 7-23: Temperature distribution across the radiometric thermal image of module P13 on the south facade on 01.07.25 at 13:30, a) pixels of the IR recording sorted by 0.5 K temperature ranges, b) box plot of the temperature distribution.

Using the median value allows us to detect systematic patterns rather than being misled by isolated abnormalities. Depending on the purpose of the IR recording, defining the arithmetic mean of each module considers isolated anomalies like cell mismatch, bypass diode issues, dirt, reflection effects or other incidents causing hotspots while the median helps analyze patterns on a system level. As seen in Figure 7-23 b) the median (58.39°C) and mean value (58.41°C) only vary by 0.02 K. This is well in the range of error for outdoor IR which is why the mean value could be used interchangeably in the evaluation chapter.

A peak each at around 55°C and 62°C in Figure 7-23 a) shows just how much the heating and cooling of the backrails affects the temperature distribution of the module. The temperatures of each pixel recorded ranging across an area of almost 14 K visible in both diagrams show that average temperatures must be used carefully.

7.3.2 Camera

To ensure reliable measurement results, devices should be cleaned regularly – particularly during outdoor setups, where dust and debris can accumulate on camera lenses and affect data quality. The camera itself with 640×512 pixels has a very high resolution, which is important to identify smaller temperature differences in the CIGS technology with a sensitivity of $\pm 2^\circ\text{C}$ or $\pm 2\%$ of the measured value. Unfortunately, dirt or damage was registered on the camera lens that could not be removed over the course of the measurement period. There are two areas in each picture which are sometimes more or less visible, depending on the angle of the light. The following pictures show these effects.

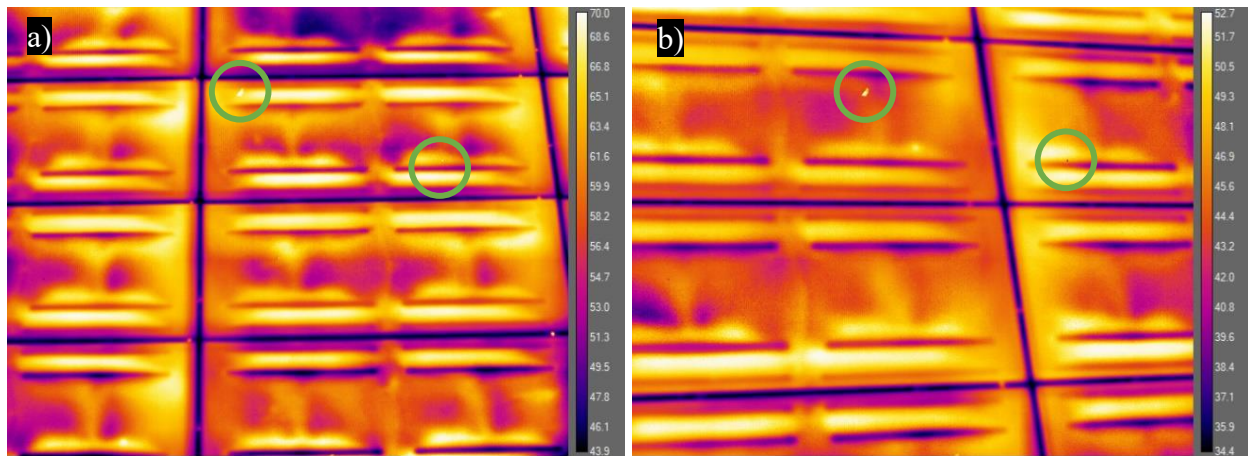


Figure 7-24: Effects of lens damage throughout the measurements recorded on different days circled green, a) on 20.05.25, and b) on 02.06.25.

The lens was cleaned thoroughly in the hopes of being able to remove the dirt, which is not uncommon after doing outdoor measurements, but the negative effects remained. A consequent issue could be that because the camera registers this area as extremely hot/ cold, these pixels are crucial for the program when defining the temperature scale. This issue can be lifted by manually adjusting the temperature range and canceling out the edge ranges, where only a few pixels artificially distort the temperature scale.

7.3.3 Reflection

Reflections from nearby surfaces – such as glass facades, metal structures, or water bodies – can distort thermal readings by introducing extraneous radiation signals. These reflected components may be misinterpreted as actual surface emissions if not properly accounted for. The reflection of the surrounding buildings plays a critical role, especially for the north facade, and is not easy to interpret in the IR images.

The effect becomes more apparent when examining the power output of the north facade over the course of a representative sunny day, as shown in Figure 7-25. Between approx. 8:20 and 19:00 the facade received no direct sunlight. Nevertheless, as the sun's height and the overall irradiation

intensity gradually increased and decreased over the course of the day, a corresponding subtle rise and fall in power generation was observed throughout the day. This power production is due to solar irradiation being reflected onto the north facade from surrounding surfaces.

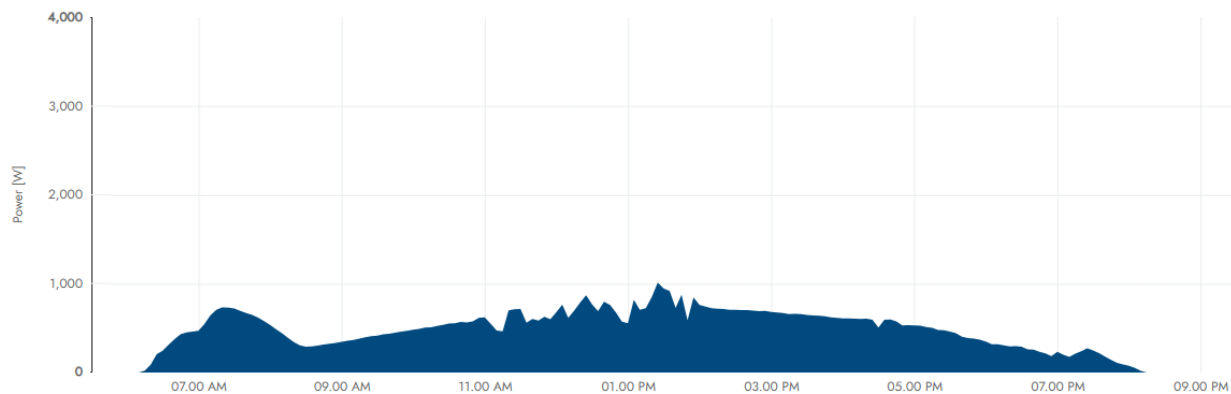


Figure 7-25: Power generated by the north facade on 09.08.25 – an exemplary sunny day. [124]

Figure 7-25 shows the effect of the partially glass partially white painted facade of the building across from the north facade reflecting the high standing sun when located in the south, allowing the north facade to produce electricity, even when the facade is totally shaded, also if only in small areas. The only periods during which direct solar irradiance reaches the north facade – and thus influences power production – are around 7:00 \pm 1h and 19:30 \pm 0,5h (7:30 PM as shown in the image). These increases in production are especially pronounced around the 21st of June of each year which is the “longest day of the year” in the region of Berlin.

The reflection of the camera lens became visible in the image when the camera angle was too close to the direction of incoming sunlight, often appearing as rings in the image. This would be the case if measuring the west facade in the morning or early noon hours as seen in Figure 7-26 a) or when measuring the north facade in the early afternoon hours as seen in Figure 7-26 b).

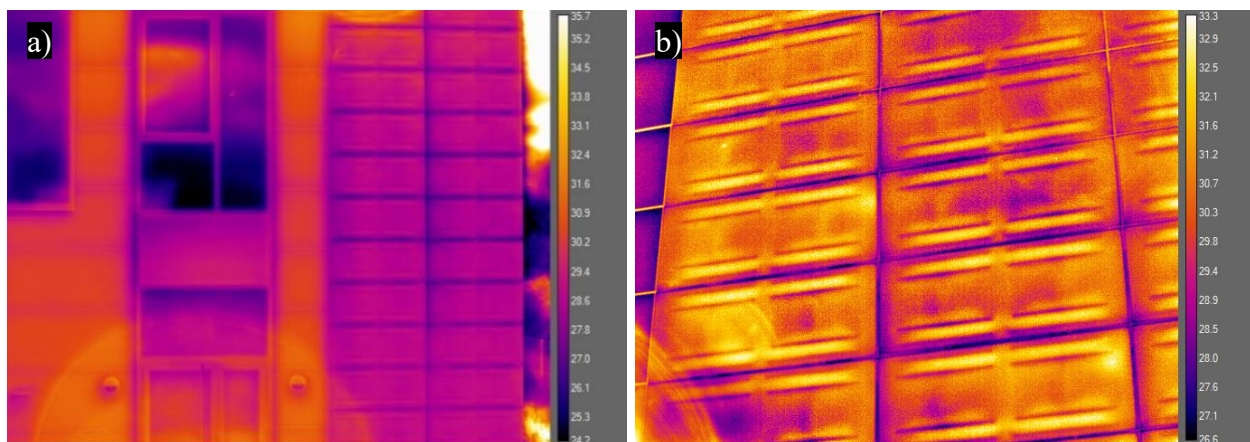


Figure 7-26: Bad positioning of the camera in reference to the sun's position causing reflection of the lens a) on the west facade during morning hours with AGC algorithm: PE on 02.06.25, b) on the north facade during early afternoon hours with AGC algorithm: APE on 20.06.25.

Nevertheless, achieving results without lens reflection depends on the operator's ability to assess and adapt the positioning conditions during measurement.

Clouds, rather than their reflections, can also obstruct infrared imaging, as they are registered as significantly hotter due to their behavior as near-ideal blackbodies with an emissivity of close to 1, while the emissivity of a clear sky depends on the dew point temperature and usually ranges between 0.7 - 0.8 in the region of Berlin [129]. Consequently, if any clouds are directly in the picture, they obstruct the temperature scale of the measurement. As reflections, these artifacts are only detectable to a schooled eye, which is why it is recommended to conduct measurements with a clear and homogeneous zenith reflection.

If measured exactly perpendicular to the modules, surface it is likely that the camera itself might be reflected as a "hot" dot in the image. Objects around the camera, such as people standing nearby, can also be reflected in the module surface and appear as hot areas. Surrounding bodies of water are likely to be a source of uncontrolled reflection, which can make IR measurements impossible. The canal running on the other side of the road is far away enough and not a factor, yet the cars and their reflections could lead to misleading interpretation and should be considered. By taking multiple measurements just minutes apart, disturbing reflections can be considered.

7.3.4 Emissivity

Since emissivity depends on multiple factors – such as material, angle, and distance – it would need to be determined separately for each measurement to achieve more accurate temperature values. For the measurements in this study an emissivity of 0.9 was used as an approximate value, which is typical for PV glass. Emissivity is also temperature dependent, meaning that its exact value would vary across the module surface if measured precisely. However, in practice, it is typically applied as a uniform value for the entire measurement frame. [38]

7.3.5 Sensitivity of Sensors

The sensitivity of sensors installed on the building is specified by the manufacturer, but this specification is only guaranteed under ideal conditions. As mentioned in Chapter 7.1.3, not all temperature sensors are fully operational, often due to insufficient contact with the back side of the module. It is not unreasonable to expect that some sensors providing data may not be ideally contacted, resulting in deviating measurements. The sensors used are programmable resolution 1-wire digital thermometers. With ideal contact, these temperature sensors can accurately measure temperatures from -55°C to $+125^{\circ}\text{C}$ (-67°F to $+257^{\circ}\text{F}$), with a 0.5°C accuracy from -10°C to $+85^{\circ}\text{C}$.

The irradiance sensors used to measure irradiance in module plane operate within a wavelength range of 400 – 1,100 nm. This covers the effective spectral range of the PV modules, but not the entire solar irradiance wavelength range. Consequently, when analysing the impact of the unused proportions of solar irradiance, the data used is incomplete. The sensors measure irradiance in the module plane across a range of 0 - 2,000 W/m^2 with a sensitivity of $50 \mu\text{V}/\text{W}/\text{m}^2$, enabling precise detection of irradiance within the defined spectral range.

8 Summary and Conclusion

This thesis investigated the application of infrared thermography (IRT) to assess large PV facade areas with focus on CIGS technology in BIPV. While thermography is established for large, rack mounted PV arrays, applying it to vertical installations introduces distinct challenges related to geometry, structural integration and environmental influences.

When conducting an IRT analysis on PV facades two primary factors must be considered: the positioning of the camera as well as the position of the sun. The orientation of the facade, daytime variations in ambient temperature and angle of solar incidence all effect module heating and cooling dynamics. Ensuring the near perpendicular viewing angle of the camera to the plane of the module minimizes emissivity errors and reflections of the measurement setup as established in relevant standards [26], [48]. If building height, access limitations, or surrounding obstacles restrict freedom to choose the measurement angle, an angle of at least 30° is recommended as the emissivity remains relatively stable within this range.

IR measurements taken within this case study indicate that using a narrow observation angle to the module plane will result in underestimation of absolute surface temperatures. More critically, measurements taken with solar reflection on the module surface have shown temperature overestimations of well over 20°C . Such distortions are not always immediately apparent and typically emerge only upon closer analysis of absolute temperature data. To mitigate, upward measurements taken at relatively shallow angles should be done at low sun positions or oriented away from the direction of irradiation incidence to avoid direct solar reflection. Environmental and seasonal variables such as ambient temperature, the degree of cloud coverage in the sky and wind conditions should be close to stable to ensure steady temperature conditions measured.

Throughout IR measurements structural and mounting elements consistently appear as pronounced thermal signatures, often masking more subtle anomalies related to cell degradation or electrical faults. Temperature differences measured were more than 10 K within a modules ROI likely causing cell mismatches and diminishing the modules' performance. Thermal images have shown intensive conductive heat dissipation in areas of direct contact between the mounting rails and the module's backsides, altering heat transfer patterns. This calls into question the widespread practice of neglecting this type of heat dissipation in PV module temperature modelling (see Chapter 4.1.2), as conduction is high enough to dominate IRT imaging.

In BIPV systems IRT can visualize ventilation behavior where areas with good air circulation appear cooler due to increased convective heat dissipation. Notably, a temperature decrease along the edges due to increased convection is also detectable. By identifying and mapping cooler zones, air flow paths can be verified and areas with insufficient ventilation can be pinpointed.

Thermography is a viable method for BIPV system maintenance, but its effectivity depends on the PV technology involved: IRT performs best on silicon-based modules with strong thermal contrasts between ideally functioning and faulty areas. CIGS modules yield low contrast IR images

making subtle anomalies hard to detect. Consequently, IRT on CIGS based facades require careful handling as their inherently muted thermal contrast limits standalone IR assessments. Nonetheless, the measurements conducted have demonstrated that physically damaged CIGS modules can be distinguished from intact modules – even though they continue to operate at the majority of their nominal capacity. Complementary diagnostics, such as monitoring of electrical parameters enhance the reliability of fault detection in PV systems. Expert interpretation is recommended to accurately identify and assess diagnostic findings. When embedded into a comprehensive maintenance framework, IRT can reveal localized overheating, thermal bridges and ventilation patterns, all of which are critical factors for sustaining the long-term safety and efficiency of BIPV installations.

In conclusion, this thesis demonstrates that IR thermography holds significant potential as a non-destructive diagnostic tool for facade-integrated PV systems if applied in combination with complementary monitoring methods, such as electrical parameter analysis. While the vertical orientation and structural complexity of BIPV installations introduce reflection challenges not typically encountered in conventional systems mounted on tilted racks, these challenges can be mitigated through careful measurement planning, contextual analysis and complementary diagnostic methods. By carefully scheduling inspections around sun position, selecting optimal camera angles and accounting for the thermal influence of mounting structures, practitioners can extract thermal understandings. The insights gained from this work contribute to a deeper understanding of thermal behavior in BIPB modules and support the development of more reliable, efficient and maintainable solar building technologies.

As urban environments continue to evolve and the demand for sustainable energy solutions grows, the relevance of BIPV systems will only increase. Ensuring their long-term performance and safety requires robust diagnostic tools capable of operating effectively within architectural constraints. IR thermography, despite its limitations, offers a promising pathway toward achieving this goal, especially when integrated into a broader framework of system monitoring and predictive maintenance. By bridging the gap between thermal imaging and electrical performance, this thesis lays the groundwork for more informed, data-driven approaches to BIPV system management.

9 Outlook

Throughout the thesis numerous avenues worth investigating beyond the scope of this work have evolved. One of them would be to develop a technique to maintain a consistent camera angle during facade inspections – even if spatial conditions do not allow for a complete examination of the facade at once. In this context, experimental studies could be conducted to explore how a lifting platform or drone based arial inspection might be employed, without introducing thermal interactions between the measurement setup and the modules, which could affect the accuracy of thermographic assessments. Establishing best practices for angle consistency could help develop standardized IR inspection protocols for BIPV systems, particularly in urban environments where access is limited.

Additionally, investigating the camera's response to varying glass structures could provide vulnerable insights for more accurate calibration of the camera and its software. The modules investigated have a matt glass structure that causes diffuse radiation and reflection, resulting in blurred IR images during thermographic measurements. Particularly in BIPV applications, it is common for architects to incorporate a variety of glass textures and colors as aesthetic considerations often take precedence over optimal energy performance. Evaluating and comparing the behavior of different surface structures, coatings, and tinting techniques in IR thermography could tailor calibration profiles for different surface types and improve diagnostic accuracy of thermal data across a diverse range of facade module types.

In this context, examining whether physical damage on PV module surfaces, such as shattered glass, can be reliably detected from viewing distances beyond 5 m remains a relevant question, as this aspect was not addressed within the scope of the present study. If damage detection at extended distances proves feasible, this could lead to more remote facade monitoring reducing the measurement workload.

Finally, the incorporation of AI-assisted thermographic analysis and automatic defect detection is growing as confidence in machine learning applications continues to rise [30], [130]. A dedicated follow-up could focus on curating representative datasets and validating machine learning models specifically for BIPV contexts, in order to improve the reliability and interpretability of monitoring technologies. This could predominantly include combining high resolution optical imaging with electrical parameter monitoring and environmental sensor data. Integrating AI-driven thermographic analysis could enable real-time fault alerts and even calculate predictions, which would shift PV maintenance from reactive to proactive, resulting in enhanced system productivity. [28], [131]

By recognizing both the opportunities and limitations of these emerging approaches, this outlook establishes a research agenda for advancing IRT in BIPV. Addressing these gaps through targeted field studies will deepen the understanding of thermal behavior in facade-integrated PV systems and enhance long-term reliability.

10 References

- [1] International Energy Agency, “Global Energy Review 2025 – Analysis,” Mar. 2025. Accessed: Jun. 28, 2025. [Online]. Available: <https://www.iea.org/reports/global-energy-review-2025>
- [2] D.-J. van de Ven *et al.*, “The potential land requirements and related land use change emissions of solar energy,” *Sci. Rep.*, vol. 11, no. 1, p. 2907, Feb. 2021, doi: 10.1038/s41598-021-82042-5.
- [3] S. Wilke, “Indikator: Anteil Erneuerbare am Bruttostromverbrauch,” Umweltbundesamt. Accessed: Sep. 13, 2025. [Online]. Available: <https://www.umweltbundesamt.de/indikator-anteil-erneuerbare-am>
- [4] BMWK-Bundesministerium für Wirtschaft und, “Erneuerbare Energien.” Accessed: Sep. 13, 2025. [Online]. Available: <https://www.bundeswirtschaftsministerium.de/Redaktion/DE/Dossier/erneuerbare-energien.html>
- [5] D. P. Graichen *et al.*, “Klimaneutrales Deutschland - Wie Deutschland seine Klimaziele schon vor 2050 erreichen kann,” Berlin, Jun. 2021. [Online]. Available: https://www.agora-energiewende.de/fileadmin/Projekte/2021/2021_04_KNDE45/A-EW_231_KNDE2045_Langfassung_DE_WEB.pdf
- [6] M. Koelman, T. Hartmann, and T. J. M. Spit, “Squeezing in – Land-use conflicts of urban energy transitions in densification,” *DisP - Plan. Rev.*, vol. 60, no. 3, pp. 40–53, Jul. 2024, doi: 10.1080/02513625.2024.2471168.
- [7] Statistisches Bundesamt, “Erneuerbare Energien decken ein Fünftel des globalen Verbrauchs - Solarenergie boomt.” Accessed: Jun. 28, 2025. [Online]. Available: <https://www.destatis.de/DE/Themen/Laender-Regionen/Internationales/Thema/umwelt-energie/energie/ErneuerbareEnergienGlobal.html>
- [8] Dr. M. Trommsdorff *et al.*, “Agrivoltaics: Opportunities for Agriculture and the Energy Transition - Fraunhofer ISE,” Fraunhofer Institute for Solar Energy Systems ISE. Accessed: Jun. 28, 2025. [Online]. Available: <https://www.ise.fraunhofer.de/en/publications/studies/agrivoltaics-opportunities-for-agriculture-and-the-energy-transition.html>
- [9] R. C and F. E, “The spatial socio-technical potential of agrivoltaics in Germany,” *Renew. Sustain. Energy Rev.*, vol. 202, p. 114706, Sep. 2024, doi: 10.1016/j.rser.2024.114706.
- [10] “C1.1: Flächenpotenziale für BIPV – BIPV Initiative.” Accessed: Sep. 13, 2025. [Online]. Available: <https://bipv-bw.de/c-bipv-im-planungsprozess/c1-1-flaechenpotenziale/>
- [11] ICARES (Becquerel Institute), “Update on BIPV market and stakeholder analysis.” BIPVBOOST, Jul. 2019.
- [12] “FVHF Leitlinie: bauwerksintegrierte Photovoltaik BIPV.” Mar. 2024. [Online]. Available: https://www.fvhf.de/Fassade-bilder/docs/Prospekte/FVHF_Leitlinie_bauwerksintegrierte-Photovoltaik-BIPV.pdf
- [13] Bundesverband Solarwirtschaft e.V., “Solarpflichten in deutschen Bundesländern.” Accessed: Sep. 13, 2025. [Online]. Available: https://www.solarwirtschaft.de/wp-content/uploads/2024/05/Uebersicht_Solarpflichten_Bundeslaender_Langfassungen.pdf
- [14] *LOI n° 2023-175 du 10 mars 2023 relative à l'accélération de la production d'énergies renouvelables (1)*. 2023.
- [15] D. Auvergne-Rhône-Alpes, “Foire Aux Questions: Obligations de solarisation,” DREAL Auvergne-Rhône-Alpes. Accessed: Sep. 13, 2025. [Online]. Available: <https://www.auvergne-rhone-alpes.developpement-durable.gouv.fr/foire-aux-questions-obligations-de-solarisation-a27265.html?lang=fr>
- [16] “Leitfaden zur Anzeige und Genehmigungspflicht von Photovoltaikanalagen und Energiespeichern.” Accessed: Sep. 13, 2025. [Online]. Available: <https://pvaustria.at/wp-content/uploads/Kurzversion-Leitfaden-zur-Anzeige-und-Genehmigungspflicht-von-PV-Anlagen.pdf>

- [17]D. für W. Umwelt Soziales und, “Schwerpunkt Solaroffensive,” Kanton Basel-Stadt. Accessed: Sep. 13, 2025. [Online]. Available: <https://www.bs.ch/wsu/schwerpunkt-solaroffensive>
- [18]Kanton Aargau, “Merkblatt: Pflicht zur Nutzung der Sonnenenergie.” Accessed: Sep. 13, 2025. [Online]. Available: <https://www.ag.ch/media/kanton-aargau/bvu/energie/bauen-energie/vollzugshilfen-und-formulare/merkblatt-solarpflicht-26a.pdf>
- [19]G. Newsom (CA Governor), *Building Energy Efficiency Standards for Residential and Nonresidential Buildings*, Aug. 2022. [Online]. Available: https://www.energy.ca.gov/sites/default/files/2025-07/CEC-400-2025-010-F_0.pdf
- [20]“Die obligatorische Installation von Solarmodulen beginnt im April 2025|Tokio.” Accessed: Sep. 13, 2025. [Online]. Available: <https://www.koho.metro.tokyo.lg.jp/2025/03/02.html#p1>
- [21]A. Mellit, G. M. Tina, and S. A. Kalogirou, “Fault detection and diagnosis methods for photovoltaic systems: A review,” *Renew. Sustain. Energy Rev.*, vol. 91, pp. 1–17, Aug. 2018, doi: 10.1016/j.rser.2018.03.062.
- [22]L. Hernández-Callejo, S. Gallardo-Saavedra, and V. Alonso-Gómez, “A review of photovoltaic systems: Design, operation and maintenance,” *Sol. Energy*, vol. 188, pp. 426–440, Aug. 2019, doi: 10.1016/j.solener.2019.06.017.
- [23]I. Høiaas, K. Grujic, A. G. Imenes, I. Burud, E. Olsen, and N. Belbachir, “Inspection and condition monitoring of large-scale photovoltaic power plants: A review of imaging technologies,” *Renew. Sustain. Energy Rev.*, vol. 161, p. 112353, Jun. 2022, doi: 10.1016/j.rser.2022.112353.
- [24]A. K. V. de Oliveira, M. Aghaei, and R. Rütther, “Automatic Inspection of Photovoltaic Power Plants Using Aerial Infrared Thermography: A Review,” *Energies*, vol. 15, no. 6, Art. no. 6, Jan. 2022, doi: 10.3390/en15062055.
- [25]N. Martín-Chivelet, J. Polo, C. Sanz-Saiz, L. T. Núñez Benítez, M. Alonso-Abella, and J. Cuenca, “Assessment of PV Module Temperature Models for Building-Integrated Photovoltaics (BIPV),” *Sustainability*, vol. 14, no. 3, p. 1500, Jan. 2022, doi: 10.3390/su14031500.
- [26]Ulrike Jahn and Magnus Herz, “Review on Infrared and Electroluminescence Imaging for PV Field Applications,” ResearchGate. Accessed: Aug. 22, 2025. [Online]. Available: https://www.researchgate.net/publication/364939388_Review_on_Infrared_and_Electroluminescence_Imaging_for_PV_Field_Applications
- [27]M. Martínez, S. Suarez, D. Jason, D. Villoslada, J. Rivas, and S. Rodríguez-Conde, “Defect Quantification System Through Aerial Inspections,” *41st Eur. Photovolt. Sol. Energy Conf. Exhib.*, pp. 020361-001-020361-004, 2024, doi: 10.4229/EUPVSEC2024/4BV.3.52.
- [28]A. Khatri, S. Khadka, N. Lamichhane, and R. Shrestha, “A comprehensive review of infrared thermography and deep learning applications for solar photovoltaic systems,” *Infrared Phys. Technol.*, vol. 148, p. 105878, Aug. 2025, doi: 10.1016/j.infrared.2025.105878.
- [29]D. Amstad, A. K. Vidal De Oliveira, A. Häberle, and R. Rütther, “Fault Inspection of CIGS PV Plant Using Aerial Infrared Thermography,” *36th Eur. Photovolt. Sol. Energy Conf. Exhib. 1569-1574*, p. 6 pages, 5419 kb, 2019, doi: 10.4229/EUPVSEC20192019-5CV.4.6.
- [30]A. Memari and T. Debich, “Drone-Assisted Infrared Thermography and Machine Learning for Enhanced Photovoltaic Defect Detection: A Comparative Study of Vision Transformers and YOLOv8,” in *Artificial Intelligence XLI*, M. Bramer and F. Stahl, Eds., Cham: Springer Nature Switzerland, 2025, pp. 59–72. doi: 10.1007/978-3-031-77918-3_5.
- [31]“Fundamentals of Infrared Thermal Imaging,” in *Infrared Thermal Imaging*, John Wiley & Sons, Ltd, 2017, pp. 1–106. doi: 10.1002/9783527693306.ch1.
- [32]“What is infrared radiation?,” Federal Office for Radiation Protection. Accessed: Aug. 20, 2025. [Online]. Available: <https://www.bfs.de/EN/topics/opt/ir/introduction/introduction.html>
- [33]“6.2: Blackbody Radiation,” Physics LibreTexts. Accessed: Aug. 20, 2025. [Online]. Available: [https://phys.libretexts.org/Bookshelves/University_Physics/University_Physics_\(OpenStax\)/University_Physics_III_-](https://phys.libretexts.org/Bookshelves/University_Physics/University_Physics_(OpenStax)/University_Physics_III_-)

- [34]M. Planck, “On the law of the energy distribution in the normal spectrum,” *Ann Phys*, vol. 4, no. 553, pp. 1–11, 1901.
- [35]M. Vollmer, “Infrared Thermal Imaging,” in *Computer Vision*, Springer, Cham, 2020, pp. 1–4. doi: 10.1007/978-3-030-03243-2_844-1.
- [36]I. Subedi, T. J. Silverman, M. G. Deceglie, and N. J. Podraza, “Emissivity of solar cell cover glass calculated from infrared reflectance measurements,” *Sol. Energy Mater. Sol. Cells*, vol. 190, pp. 98–102, Feb. 2019, doi: 10.1016/j.solmat.2018.09.027.
- [37]B. Jaeckel, B. Weinreich, C. Buerhop-Lutz, and U. Jahn, “Outdoor Non-Destructive Infrared Thermography of Photovoltaic Modules and Plants for Inspection: IEC 62446-3,” *32nd Eur. Photovolt. Sol. Energy Conf. Exhib. 1741-1745*, p. 5 pages, 4881 kb, 2016, doi: 10.4229/EUPVSEC20162016-5DO.12.3.
- [38]*DIN IEC/TS 62446-3 VDE V 0126-23-3:2018-04 Photovoltaik(PV)-Systeme – Anforderungen an Prüfung, Dokumentation und Instandhaltung Teil 3: Photovoltaische Module und Betriebsanlagen – Infrarot-Thermografie im Freien*, DIN IEC/TS 62446-3:2018-04, Berlin., 2018. Accessed: Jun. 28, 2025. [Online]. Available: <https://www.vde-verlag.de/normen/0100451/din-iec-ts-62446-3-vde-v-0126-23-3-2018-04.html>
- [39]V. Quaschnig, *Regenerative Energiesysteme: Technologie – Berechnung – Klimaschutz*. Carl Hanser Verlag GmbH Co KG, 2023.
- [40]M. P. Brennan, A. L. Abramase, R. W. Andrews, and J. M. Pearce, “Effects of spectral albedo on solar photovoltaic devices,” *Sol. Energy Mater. Sol. Cells*, vol. 124, pp. 111–116, May 2014, doi: 10.1016/j.solmat.2014.01.046.
- [41]“Water absorption spectrum.” Accessed: Aug. 21, 2025. [Online]. Available: https://water.lsbu.ac.uk/water/water_vibrational_spectrum.html#glob
- [42]“THz antennas design, developments, challenges, and applications: A review,” *ResearchGate*, May 2025, doi: 10.1002/dac.5474.
- [43]FLIR Sytems, Inc., “Reference documentation Thermography.” Aug. 13, 2019. [Online]. Available: https://support.flir.com/DSDownload/Assets/T810442-en-US_A4.pdf
- [44]Heliguy, “In-depth Guide To Thermal Imaging,” Heliguy™. Accessed: Aug. 21, 2025. [Online]. Available: <https://www.heliguy.com/blogs/posts/guide-to-thermal-imaging/>
- [45]volterradrone, “Radiometric Vs RGB Thermal Imagery,” Volterra Drone. Accessed: Aug. 21, 2025. [Online]. Available: <https://www.volterradrone.com/post/radiometric-vs-rgb-thermal-imagery>
- [46]R. Liu *et al.*, “Eddy current pulsed thermography with an inductive heating layer (ECPT-IHL) for subsurface defect detection in GFRP materials,” *Compos. Part B Eng.*, vol. 290, p. 111982, Feb. 2025, doi: 10.1016/j.compositesb.2024.111982.
- [47]C. Buerhop-Lutz *et al.*, “aIR-PV-Check of Thin-Film PV-Plants – Detection of PID and Other Defects in CIGS Modules,” *32nd Eur. Photovolt. Sol. Energy Conf. Exhib. 2021-2026*, p. 6 pages, 8063 kb, 2016, doi: 10.4229/EUPVSEC20162016-5BV.2.51.
- [48]International Electrotechnical Commission, *IEC TS 62446-3:2017. Photovoltaic (PV) systems – Requirements for testing, documentation and maintenance – Part 3: Photovoltaic modules and plants – Outdoor infrared thermography*, IEC TS 62446-3, Geneva., 2017. Accessed: Jun. 28, 2025. [Online]. Available: <https://webstore.iec.ch/en/publication/28628>
- [49]E. Kaplani and S. Kaplanis, “PV Module Temperature Prediction at Any Environmental Conditions and Mounting Configurations,” in *Renewable Energy and Sustainable Buildings: Selected Papers from the World Renewable Energy Congress WREC 2018*, A. Sayigh, Ed., Cham: Springer International Publishing, 2020, pp. 921–933. doi: 10.1007/978-3-030-18488-9_77.

- [50]I. Berardone, J. Lopez Garcia, and M. Paggi, “Analysis of electroluminescence and infrared thermal images of monocrystalline silicon photovoltaic modules after 20 years of outdoor use in a solar vehicle,” *Sol. Energy*, vol. 173, pp. 478–486, Oct. 2018, doi: 10.1016/j.solener.2018.07.055.
- [51]M. Waqar Akram *et al.*, “Improved outdoor thermography and processing of infrared images for defect detection in PV modules,” *Sol. Energy*, vol. 190, pp. 549–560, Sep. 2019, doi: 10.1016/j.solener.2019.08.061.
- [52]N. Martín-Chivelet *et al.*, “Building-Integrated Photovoltaic (BIPV) products and systems: A review of energy-related behavior,” *Energy Build.*, vol. 262, p. 111998, May 2022, doi: 10.1016/j.enbuild.2022.111998.
- [53]T. E. Kuhn, C. Erban, M. Heinrich, J. Eisenlohr, F. Ensslen, and D. H. Neuhaus, “Review of technological design options for building integrated photovoltaics (BIPV),” *Energy Build.*, vol. 231, p. 110381, Jan. 2021, doi: 10.1016/j.enbuild.2020.110381.
- [54]P. Stadel, “Colored BIPV - Market, Research and Development,” Task Report Report IEA-PVPS T15-07: 2019, 2019. [Online]. Available: https://iea-pvps.org/wp-content/uploads/2020/01/IEA-PVPS_15_R07_Coloured_BIPV_report.pdf
- [55]M. Babin, I. H. Jóhannsson, M. L. Jakobsen, and S. Thorsteinsson, “Experimental evaluation of the impact of pigment-based colored interlayers on the temperature of BIPV modules,” *EPJ Photovolt.*, vol. 14, p. 34, 2023, doi: 10.1051/epjpv/2023028.
- [56]W. Li, Y. Shi, Z. Chen, and S. Fan, “Photonic thermal management of coloured objects,” *Nat. Commun.*, vol. 9, p. 4240, Oct. 2018, doi: 10.1038/s41467-018-06535-0.
- [57]N. Albinus, “Master Thesis: Building-integrated photovoltaics - An investigation of solar modules as ventilated curtain wall facade depending on the specific rear-ventilation and insulation.” htw Berlin, Apr. 14, 2022. [Online]. Available: <https://www.helmholtz-berlin.de/media/media/projekte/pvcomb/PDF/abschlussarbeiten/niklas-albinus-masterarbeit-2022.pdf>
- [58]“EN 50583-1:2016 - Photovoltaics in buildings - Part 1: BIPV modules,” iTeh Standards. Accessed: Jul. 08, 2025. [Online]. Available: <https://standards.iteh.ai/catalog/standards/clc/a749f8c8-938e-48a4-9a7d-0891a4c57f8f/en-50583-1-2016>
- [59]“CIGS Elemente,” Home. Accessed: Jul. 08, 2025. [Online]. Available: <https://www.avancis.de/magazin/cigs-elemente>
- [60]H. Zhang, F. Qu, and H. Li, “Front Transparent Passivation of CIGS-Based Solar Cells via AZO,” *Molecules*, vol. 27, no. 19, Art. no. 19, Jan. 2022, doi: 10.3390/molecules27196285.
- [61]T. Zhou and C. Shang, “Parameter Identification of Photovoltaic Models by an Enhanced RIME Algorithm,” *Int. J. Energy Res.*, vol. 2024, no. 1, p. 9777345, 2024, doi: 10.1155/2024/9777345.
- [62]Marc Köntges, Sarah Kurtz, Corinne Packard, and Ulrike Jahn, “Review of Failures of Photovoltaic Modules Final 2014-05-06 BMWi logo,” Report IEA-PVPS T13-01:2014. Accessed: Sep. 16, 2025. [Online]. Available: https://www.researchgate.net/publication/279955703_141212_IEA-PVPS_T13-01_2014_Review_of_Failures_of_Photovoltaic_Modules_Final_2014-05-06_BMWi_logo
- [63]M. Aghaei, “Autonomous Monitoring and Analysis of Photovoltaic Systems,” *Energies*, vol. 15, no. 14, Art. no. 14, Jan. 2022, doi: 10.3390/en15145011.
- [64]M. Aghaei *et al.*, “Review of degradation and failure phenomena in photovoltaic modules,” *Renew. Sustain. Energy Rev.*, vol. 159, p. 112160, May 2022, doi: 10.1016/j.rser.2022.112160.
- [65]J. Kettle *et al.*, “Review of technology specific degradation in crystalline silicon, cadmium telluride, copper indium gallium selenide, dye sensitised, organic and perovskite solar cells in photovoltaic modules: Understanding how reliability improvements in mature technologies can enhance emerging technologies,” *Prog. Photovolt. Res. Appl.*, vol. 30, no. 12, pp. 1365–1392, 2022, doi: 10.1002/pip.3577.

- [66]M. Faifer, S. Ierace, and M. Lazzaroni, “Maintenance Scheduling by Means of Electrical Signature Analysis Technology”, [Online]. Available: <https://www.imeko.info/publications/tc4-2014/IMEKO-TC4-2014-404.pdf>
- [67]“IEC 61724-1:2021.” Accessed: Aug. 24, 2025. [Online]. Available: <https://webstore.iec.ch/en/publication/65561>
- [68]Paolo Corti, Pierlugi Bonomo, and Francesco Frontini, “Building Integrated Photovoltaics: A practical handbook for solar buildings’ stakeholders,” *SUPSI - ISAAC - BIPV Res. Team*, p. 72, Oct. 2024.
- [69]A. J. Aristizábal Cardona, C. A. Páez Chica, and D. H. Ospina Barragán, “Implementation of the BIPVS Monitoring System,” in *Building-Integrated Photovoltaic Systems (BIPVS): Performance and Modeling Under Outdoor Conditions*, A. J. Aristizábal Cardona, C. A. Páez Chica, and D. H. Ospina Barragán, Eds., Cham: Springer International Publishing, 2018, pp. 79–89. doi: 10.1007/978-3-319-71931-3_8.
- [70]A. J. Aristizábal Cardona, C. A. Páez Chica, and D. H. Ospina Barragán, “BIPVS Basics for Design, Sizing, Monitoring, and Power Quality Measurement and Assessment,” in *Building-Integrated Photovoltaic Systems (BIPVS): Performance and Modeling Under Outdoor Conditions*, A. J. Aristizábal Cardona, C. A. Páez Chica, and D. H. Ospina Barragán, Eds., Cham: Springer International Publishing, 2018, pp. 17–33. doi: 10.1007/978-3-319-71931-3_3.
- [71]H. L. Tsai and C. J. Yang, “PV Model with Energy Balance Equation for Commercial PV Modules,” *Appl. Mech. Mater.*, vol. 284–287, pp. 1163–1167, Jan. 2013, doi: 10.4028/www.scientific.net/AMM.284-287.1163.
- [72]R. Arena, S. Aneli, G.M. Tina, and A. Gagliano, “Experimental analysis of the performances of ventilated photovoltaic facades,” *RE&PQJ*, vol. 20, no. 2, Jan. 2024, doi: 10.24084/repqj20.257.
- [73]“PV Module Temperature | PVEducation.” Accessed: Jul. 09, 2025. [Online]. Available: <https://www.pveducation.org/pvcdrom/modules-and-arrays/pv-module-temperature>
- [74]L. M. Shaker, A. A. Al-Amiery, M. M. Hanoon, W. K. Al-Azzawi, and A. A. H. Kadhum, “Examining the influence of thermal effects on solar cells: a comprehensive review,” *Sustain. Energy Res.*, vol. 11, no. 1, p. 6, Feb. 2024, doi: 10.1186/s40807-024-00100-8.
- [75]“Thermal Modelling of Photovoltaic Modules in Operation and Production,” in *ResearchGate*, May 2025. doi: 10.4229/EUPVSEC20192019-4CO.2.4.
- [76]“Quantum Efficiency | PVEducation.” Accessed: Sep. 09, 2025. [Online]. Available: <https://www.pveducation.org/pvcdrom/solar-cell-operation/quantum-efficiency>
- [77]“Three-Dimensional Cu(InGa)Se Photovoltaic Cells Simulations: Optimization for Limited-Range Wavelength Applications,” *ResearchGate*, Aug. 2025, doi: 10.1109/jphotov.2013.2258191.
- [78]“Development of ultrathin Cu(In,Ga)Se₂-based solar cells with reflective back contacts,” *ResearchGate*. Accessed: Sep. 09, 2025. [Online]. Available: https://www.researchgate.net/publication/343139839_Development_of_ultrathin_CuInGaSe_-based_solar_cells_with_reflective_back_contacts
- [79]“Heat Generation in PV Modules | PVEducation.” Accessed: Jul. 10, 2025. [Online]. Available: <https://www.pveducation.org/pvcdrom/modules-and-arrays/heat-generation-in-pv-modules>
- [80]H. Xie, Z. Song, Y. Tang, and J. Ji, “Performance analysis of a novel CPV/T system with curved CIGS modules: Comparison with traditional flat modules,” *Appl. Energy*, vol. 389, p. 125738, Jul. 2025, doi: 10.1016/j.apenergy.2025.125738.
- [81]F. Zhou, J. Ji, J. Cai, and B. Yu, “Experimental and numerical study of the freezing process of flat-plate solar collector,” *Appl. Therm. Eng.*, vol. 118, pp. 773–784, May 2017, doi: 10.1016/j.applthermaleng.2017.02.111.

- [82]S. Kumar and S. C. Mullick, “Wind heat transfer coefficient in solar collectors in outdoor conditions,” *Sol. Energy*, vol. 84, no. 6, pp. 956–963, Jun. 2010, doi: 10.1016/j.solener.2010.03.003.
- [83]“Heat Loss in PV Modules | PVEducation.” Accessed: Jul. 10, 2025. [Online]. Available: <https://www.pveducation.org/pvcdrom/modules-and-arrays/heat-loss-in-pv-modules>
- [84]P. Stephan, S. Kabelac, M. Kind, D. Mewes, K. Schaber, and T. Wetzel, Eds., *VDI-Wärmeatlas: Fachlicher Träger VDI-Gesellschaft Verfahrenstechnik und Chemieingenieurwesen*, 12. Aufl. 2019. in Springer Reference Technik. Berlin, Heidelberg: Springer Berlin Heidelberg, 2019. doi: 10.1007/978-3-662-52989-8.
- [85]B. Tuncel, T. Ozden, R. S. Balog, and B. G. Akinoglu, “Dynamic thermal modelling of PV performance and effect of heat capacity on the module temperature,” *Case Stud. Therm. Eng.*, vol. 22, p. 100754, Dec. 2020, doi: 10.1016/j.csite.2020.100754.
- [86]S. Ramesh *et al.*, “Energy yield framework to simulate thin film CIGS solar cells and analyze limitations of the technology,” *Sci. Rep.*, vol. 15, no. 1, p. 988, Jan. 2025, doi: 10.1038/s41598-024-78862-w.
- [87]A. Pavgi, J. Kuitche, J. Oh, and G. TamizhMani, “Climate-Specific Thermal Model Coefficients for c-Si and Thin-Film PV Modules,” in *2017 IEEE 44th Photovoltaic Specialist Conference (PVSC)*, Jun. 2017, pp. 1883–1887. doi: 10.1109/PVSC.2017.8366643.
- [88]P. Singh and N. M. Ravindra, “Temperature dependence of solar cell performance—an analysis,” *Sol. Energy Mater. Sol. Cells*, vol. 101, pp. 36–45, Jun. 2012, doi: 10.1016/j.solmat.2012.02.019.
- [89]N. Alhammedi, E. Rodriguez-Ubinas, S. Alzarouni, and M. Alantali, “Building-integrated photovoltaics in hot climates: Experimental study of CIGS and c-Si modules in BIPV ventilated facades,” *Energy Convers. Manag.*, vol. 274, p. 116408, Dec. 2022, doi: 10.1016/j.enconman.2022.116408.
- [90]“Avancis SKALA Datasheets.”
- [91]C. Yu *et al.*, “Temperature dependence of the band gap of perovskite semiconductor compound CsSnI₃,” *J. Appl. Phys.*, vol. 110, no. 6, Sep. 2011, doi: 10.1063/1.3638699.
- [92]F. Frontini, G. Friesen, C. Polo López, and T. Friesen, “Experience on the Behavior of Different BIPV Solution: Electrical and Thermal Performance of Roof and Façade Mounted Micromorph Modules,” *28th Eur. Photovolt. Sol. Energy Conf. Exhib. 4357-4360*, p. 4 pages, 6066 kb, 2013, doi: 10.4229/28THEUPVSEC2013-5CV.7.6.
- [93]B. N. S. Sampah, F. K. A. Nyarko, B. A. Asaaga, and J. Aggor, “Generating temperature cycle profiles of different solar photovoltaic module technologies from in-situ conditions for accurate prediction of thermomechanical degradation,” *Int. J. Energ.*, vol. 7, no. 2, pp. 41–51, Dec. 2022, doi: 10.47238/ijeca.v7i2.205.
- [94]Andreas Beinert, Pascal Romer, Martin Heinrich, and Jarir Aktaa, “Thermomechanical Design Rules for PV Modules,” in *ResearchGate*, Sep. 2022. doi: 10.4229/WCPEC-82022-3CO.5.1.
- [95]D. Lee *et al.*, “Damp heat and thermal cycling-induced degradation mechanism of AZO and CIGS films in Cu(In,Ga)Se₂ photovoltaic modules,” *Curr. Appl. Phys.*, vol. 15, no. 3, pp. 285–291, Mar. 2015, doi: 10.1016/j.cap.2014.12.023.
- [96]Björn Rau, “Aufbau einer fassaden-integrierten Photovoltaikanlage am HZB für Forschungszwecke am Beispiel „Testinghalle“ auf dem WCRC, Adlershof,” HZB, Berlin, Aug. 2018.
- [97]H.-Z. B. für M. und Energie, “Reallabor für BIPV,” HZB Website. Accessed: Aug. 29, 2025. [Online]. Available: https://www-intern.helmholtz-berlin.de/projects/pvcomb/forschen/living-lab-bipv/index_de.html
- [98]“Google Earth.” Accessed: Aug. 14, 2025. [Online]. Available: <https://earth.google.com/web/@52.42651349,13.53266545,38.84062185a,179.24674596d,35y,6>

2.97538868h,42.49993192t,360r/data=CgRCAggBOgMKATBCAggASg0I_____ARA
A

- [99] “AVANCIS GmbH - AVANCIS SKALA im Kontext realisierter Projekte | BAUKOBOX.” Accessed: Jun. 28, 2025. [Online]. Available: <https://baukobox.de/produkte/4600-avancis-gmbh-avancis-skala>
- [100] “Montage Allgemein - AVANCIS SKALA Sicherheits-, Installations- Und Betriebshandbuch [Seite 7],” ManualsLib. Accessed: Aug. 23, 2025. [Online]. Available: <https://www.manualslib.de/manual/917613/Avancis-Skala.html>
- [101] “FLIR A6700 MWIR | Teledyne FLIR.” Accessed: Aug. 17, 2025. [Online]. Available: <https://www.flir.de/products/a6700-mwir?vertical=science&segment=solutions>
- [102] Maximilian Riedel, “Sensorkonzept Tesinghalle.”
- [103] “Digitales Thermo-Hygrometer 30.5048,” TFA Dostmann. Accessed: Aug. 19, 2025. [Online]. Available: <https://www.tfa-dostmann.de/produkt/digitales-thermo-hygrometer-30-5048/>
- [104] thermometrics, “Type K Thermocouple,” Thermometricscorp.com. Accessed: Aug. 19, 2025. [Online]. Available: <http://www.thermometricscorp.com/thertypk.html>
- [105] “Flash Test: technical background and importance.” Accessed: Aug. 09, 2025. [Online]. Available: <https://sinovoltaics.com/learning-center/testing/flash-test-technical-background-and-importance/>
- [106] D. Bertani, C. Liciotti, S. Guastella, and C. Camilloni, “Investigation and Diagnostic Tool Comparison: Infrared Thermography vs Electroluminescence,” *32nd Eur. Photovolt. Sol. Energy Conf. Exhib. 2098-2104*, p. 7 pages, 7850 kb, 2016, doi: 10.4229/EUPVSEC20162016-5BV.2.81.
- [107] “thermal paste packaging.”
- [108] Janina Moereke and Stefan Grünsteidl, “Thermographie SKALA Fassade,” May 26, 2025.
- [109] “Sonnenaufgang und Sonnenuntergang im Juli 2025,” Vollmond-info.de. Accessed: Jul. 12, 2025. [Online]. Available: <https://vollmond-info.de/sonnenkalender/sonnenaufgang-und-sonnenuntergang-im-juli/>
- [110] S.-H. Lin, Y.-C. Lu, C.-C. Tai, and C. Tzu-Huan, “Identification of Edge Recombination from CIGS Solar Cells,” in *2019 26th International Workshop on Active-Matrix Flatpanel Displays and Devices (AM-FPD)*, Jul. 2019, pp. 1–4. doi: 10.23919/AM-FPD.2019.8830632.
- [111] P. Yilmaz *et al.*, “In-depth analysis of potential-induced degradation in a commercial CIGS PV module,” *Prog. Photovolt. Res. Appl.*, vol. 31, no. 6, pp. 627–636, 2023, doi: 10.1002/pip.3670.
- [112] T. S. Vaas *et al.*, “Light induced degradation of CIGS solar cells,” *Sol. Energy Mater. Sol. Cells*, vol. 275, p. 113036, Sep. 2024, doi: 10.1016/j.solmat.2024.113036.
- [113] J. Lee, “Metastability of copper indium gallium diselenide polycrystalline thin film solar cell devices,” University of Oregon, 2008. Accessed: Aug. 08, 2025. [Online]. Available: <https://hdl.handle.net/1794/8588>
- [114] Guillermo Antonio Farias Basulto, “CIGSSe Thin Film Photovoltaic Yield Improvement for Operating Conditions,” Dissertation, Technische Universität Berlin, Berlin, 2021.
- [115] “Thermal Stimulation of Reverse Breakdown in CIGS Solar Cells,” *ResearchGate*, doi: 10.1109/JPHOTOV.2023.3240680.
- [116] M. E. Stuckelberger *et al.*, “How Does CIGS Performance Depend on Temperature at the Microscale?,” *IEEE J. Photovolt.*, vol. 8, no. 1, pp. 278–287, Jan. 2018, doi: 10.1109/JPHOTOV.2017.2762584.
- [117] L. Lin and N. M. Ravindra, “Temperature dependence of CIGS and perovskite solar cell performance: an overview,” *SN Appl. Sci.*, vol. 2, no. 8, p. 1361, Jul. 2020, doi: 10.1007/s42452-020-3169-2.
- [118] U. C. Matur and N. Baydoğan, “Annealing time effect on CIGS thin films,” *Emerg. Mater. Res.*, vol. 9, no. 3, pp. 725–729, Sep. 2020, doi: 10.1680/jemmr.18.00061.

- [119] S. Karthikeyan, S. Hwang, M. Sibakoti, T. Bontrager, R. W. Liptak, and S. A. Campbell, "Effect of rapid thermal annealing of copper indium aluminium gallium diselenide solar cell devices and its deposition challenges," *Appl. Surf. Sci.*, vol. 493, pp. 105–111, Nov. 2019, doi: 10.1016/j.apsusc.2019.06.279.
- [120] S. V. Desarada, K. B. Chavan, and N. B. Chaure, "Effect of Different Annealing Techniques on CIGS Deposited Using One-Step Single-Target Sputtering," *J. Electron. Mater.*, vol. 52, no. 5, pp. 3413–3419, May 2023, doi: 10.1007/s11664-023-10308-x.
- [121] M. Marudachalam, R. W. Birkmire, H. Hichri, J. M. Schultz, A. Swartzlander, and M. M. Al-Jassim, "Phases, Morphology, and Diffusion in $\text{CuIn}_x\text{Ga}_{1-x}\text{Se}_2$ Thin Films," *J. Appl. Phys.*, vol. 82, no. 6, pp. 2896–2905, Sep. 1997, doi: 10.1063/1.366122.
- [122] M. Jahandardoost, C. Walkons, and S. Bansal, "Degradation behavior of CIGS solar Cells: A parametric analysis," *Sol. Energy*, vol. 260, pp. 61–70, Aug. 2023, doi: 10.1016/j.solener.2023.05.052.
- [123] W. L. Schram and E. Shirazi, "PV on façades: A financial, technical and environmental assessment," *Energy Build.*, vol. 328, p. 115010, Feb. 2025, doi: 10.1016/j.enbuild.2024.115010.
- [124] "Sunny Portal powered by ennexOS." Accessed: Aug. 11, 2025. [Online]. Available: <https://ennexos.sunnyportal.com/6531195,6554701/monitoring/view-energy-and-power>
- [125] "B2: Ausrichtung und Verschattung von PV-Modulen – BIPV Initiative." Accessed: Aug. 06, 2025. [Online]. Available: <https://bipv-bw.de/b-architektur-mit-photovoltaik/b2-ausrichtung-und-verschattung/>
- [126] D.J. Coyle *et al.*, "Life Prediction for CIGS Solar Modules," presented at the DOE PV Module Reliability Workshop, Denver, CO, Feb. 2011. [Online]. Available: https://www1.eere.energy.gov/solar/pdfs/pvmrw2011_32_tf_coyle.pdf
- [127] Mirjam Theelen, N. Barreau, felix daume, and Henk Steijvers, "Accelerated performance degradation of CIGS solar cell determined by in-situ monitoring," *ResearchGate*, Oct. 2014, doi: 10.1117/12.2059951.
- [128] A. Qamar, "Outdoor performance of CIGS modules at multiple temperatures over three years," Jan. 2018, doi: 10.1117/12.2326702.
- [129] P. Berdahl and M. Martin, "Emissivity of clear skies," *Sol. Energy*, vol. 32, no. 5, pp. 663–664, 1984, doi: 10.1016/0038-092X(84)90144-0.
- [130] A. Thakfan and Y. Bin Salamah, "Development and Performance Evaluation of a Hybrid AI-Based Method for Defects Detection in Photovoltaic Systems," *Energies*, vol. 18, no. 4, p. 812, Jan. 2025, doi: 10.3390/en18040812.
- [131] S. Aksoy, "Benchmarking Vision Transformers and CNNs for Thermal Photovoltaic Fault Detection with Explainable AI Validation," Sep. 08, 2025, *arXiv*: arXiv:2509.07039. doi: 10.48550/arXiv.2509.07039.

11 Academic Integrity Declaration

I hereby declare that I have written all parts of this thesis independently and that I have not used any sources or aids other than those stated in the thesis, and that the thesis has not been presented in the same or a similar form in any other examination. All verbatim or in-sentence copies and quotations have been identified and verified. I have not used any AI-generated text passages or content in the thesis. Furthermore, I assure that I have not used any other AI-based tools whose use has been explicitly excluded in writing by the examiner.

Berlin, 22.09.2025, Luca Raschke
(Place, Date, Signature)

12 Appendix

A1 Additional Data

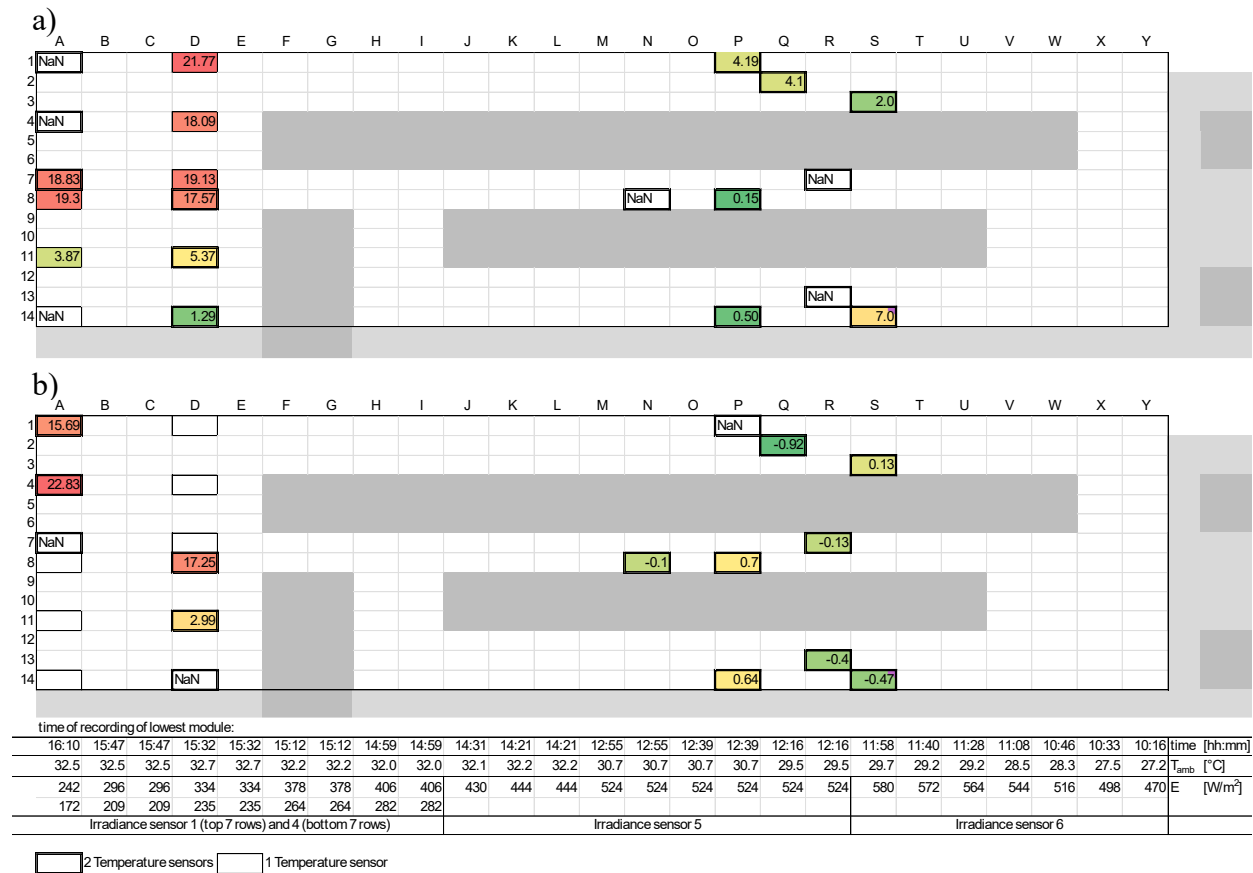


Figure 12-1: Temperature difference (ΔT) of mean temperature measured by IR camera, as in Figure 7-6, and measured by temperature sensor on module backsides of selected modules at the same time, a) with the sensor placed in the center of the module, and b) with the sensor placed at the edge of the module

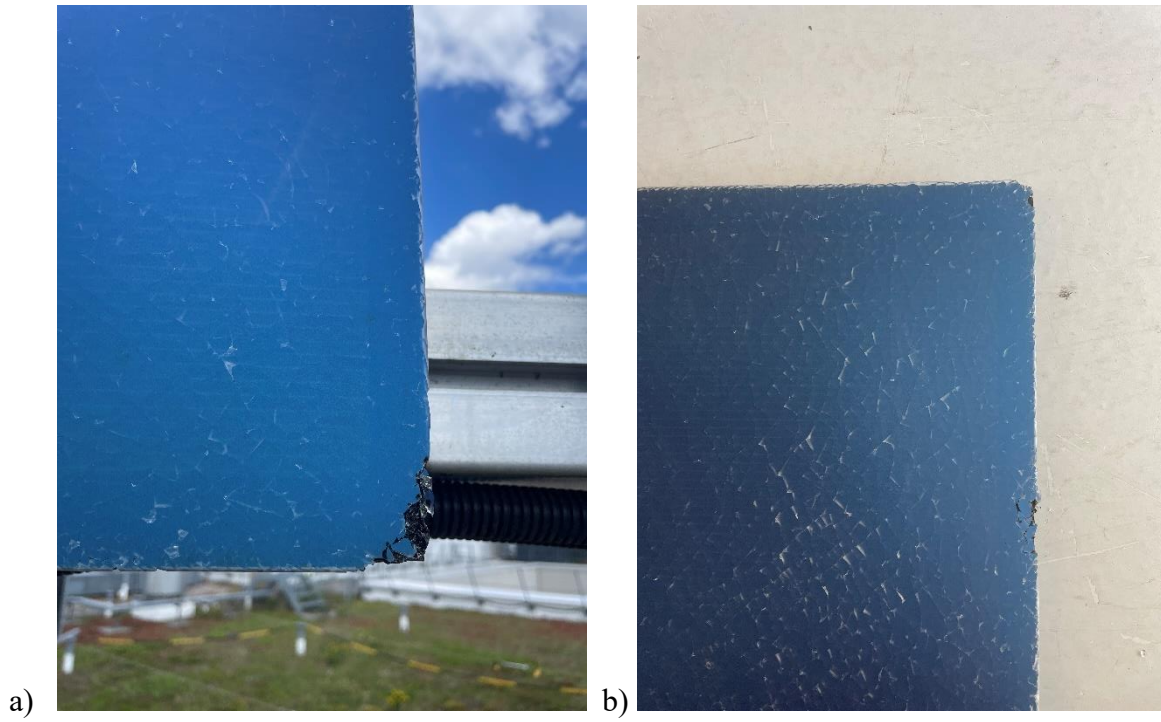


Figure 12-2: Close-up of damaged front glass in module 0688

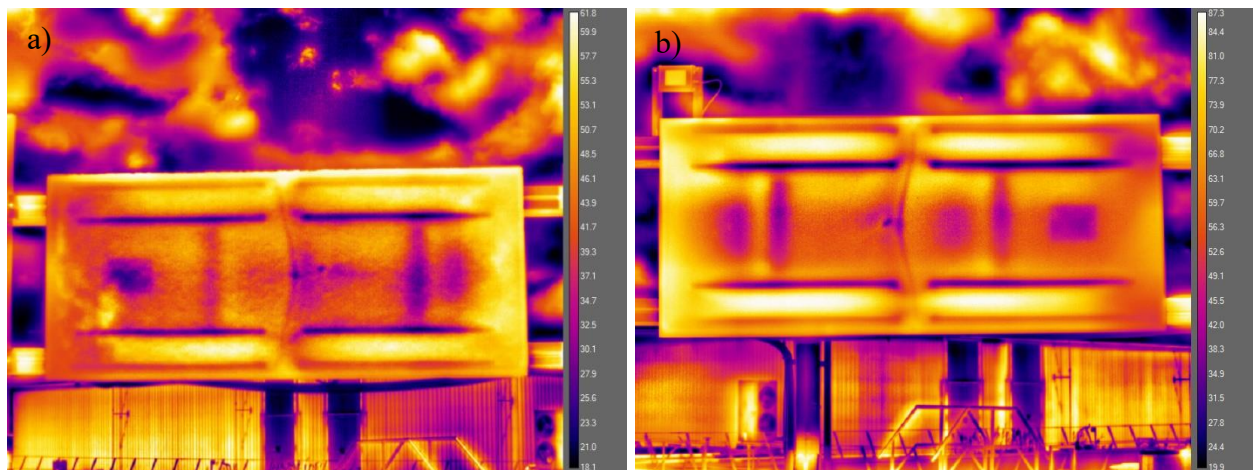


Figure 12-3: Entire IR recordings including temperature scale, a) IR recording of module 0688, b) mirrored IR recoding of module 0069

A2 Technical Data

Acancis SKALA CIGS Modules



Figure 12-4: Module label stickers of the modules used on the HZB Living Lab facade, a) module type as for module 0069, and b) module type as for 0688

IR Camera: FLIR A6700sc

Resolution:	640 × 512
Spectral Range:	1.0 – 5.0 μm
Pixel Size [Square]:	15 μm
Detector Type:	FLIR indium antimonide (InSb)
Camera f-number:	f/2.5
Frame Rate [Full Window]:	Programmable: 0.0015 Hz to 60 Hz
Integration Time:	480 ns to ~full frame
Standard Temperature Range [with band matched optics]:	-20°C to 300°C (-4°F to 572°F)
Optional Temperature Range [with band matched optics]:	45°C to 600°C/113°F to 1112°F (ND1); 250°C to 2000°C/482°F to 3632°F (ND2); 500°C to 3000°C/932°F to 5432°F (ND3)
Sensitivity:	± 2 °C or 2% of measured value
Filter Holder [Warm]:	Behind lens mount for standard 1 inch diameter filters
Focus:	Manual [101]